EPRI-EL-1757

Magnetic Refrigerator Development

EL-1757
Research Project 7867-1

Final Report, April 1981

Prepared by

LOS ALAMOS SCIENTIFIC LABORATORY
University of California
Los Alamos, New Mexico 87545

Principal Investigators
J. A. Barclay
W. A. Steyert

Prepared for

Electric Power Research Institute
3412 Hillview Avenue
Palo Alto, California 94304

EPRI Project Manager
M. Rabinowitz

Underground Transmission Program
Electrical Systems Division

DISTRIBUTION OF THIS DOCUMENT IS UNLIMITED

DISCLAIMER

Portions of this document may be illegible in electronic image products. Images are produced from the best available original document.

ORDERING INFORMATION

Requests for copies of this report should be directed to Research Reports Center (RRC), Box 50490, Palo Alto, CA 94303, (415) 965-4081. There is no charge for reports requested by EPRI member utilities and affiliates, contributing nonmembers, U.S. utility associations, U.S. government agencies (federal, state, and local), media, and foreign organizations with which EPRI has an information exchange agreement. On request, RRC will send a catalog of EPRI reports.

EPRI authorizes the reproduction and distribution of all or any portion of this report and the preparation of any derivative work based on this report, in each case on the condition that any such reproduction, distribution, and preparation shall acknowledge this report and EPRI as the source.

NOTICE

This report was prepared by the organization(s) named below as an account of work sponsored by the Electric Power Research Institute, Inc. (EPRI). Neither EPRI, members of EPRI, the organization(s) named below, nor any person acting on their behalf: (a) makes any warranty or representation, express or implied, with respect to the accuracy, completeness, or usefulness of the information contained in this report, or that the use of any information, apparatus, method, or process disclosed in this report may not infringe privately owned rights; or (b) assumes any liabilities with respect to the use of, or for damages resulting from the use of, any information, apparatus, method, or process disclosed in this report.

Prepared by
Los Alamos Scientific Laboratory
Los Alamos, New Mexico

ABSTRACT

The research described here is the first step in a program to develop magnetic refrigeration in the 4 to 10K temperature region. The original purpose of the program was to provide more efficient refrigeration for superconducting technological applications in power generation and transmission. However, the work reported forms part of the basis for a whole new refrigeration technology with a myriad of applications extending beyond the original objective.

To initiate development of the low-temperature refrigerator technology, a gadolinium-metal, magnetic-wheel prototype was designed, built, and tested at room temperature with the objective of understanding the device in an experimentally convenient temperature region. When operating through a 6-T magnetic-field difference, the wheel was designed to provide 1 kW of continuous refrigeration across a 40K span near room temperature and to operate at 70% of Carnot efficiency. The prototype operated through a 1.2-T field difference and provided 1/2 kW of continuous refrigeration over a 7K span at 26% of Carnot efficiency.

One problem that was found with this first device was the difficulty of producing simultaneously a high, homogeneous field across the top of the wheel with almost zero field across the bottom of the wheel. Problems with fluid-flow control of both transient and entrained fluid were also encountered. Nevertheless, the performance results at 1.2-T field difference are those predicted by the theory used to determine the design objectives at 6-T field difference. A second magnetic refrigerator, a simple reciprocating device, was also designed, built, and tested with the objective of understanding the problems associated with this class of design for low-temperature application.

The results of several experiments show that the principle of operation is understood and offers exciting prospects. Experiments with water as the heat exchange fluid and gadolinium as the magnetic material provided up to 1/2-kJ/cycle of refrigeration. The key problem uncovered is that of compensating large magnetic forces while keeping parasitic heat leaks to a minimum.

EPRI PERSPECTIVE

PROJECT DESCRIPTION

This report presents the results of RP7867-1 undertaken by the Los Alamos Scientific Laboratory to develop a magnetic refrigerator. Low-cost, high-efficiency refrigeration would be an important adjunct to any forced-cooled underground transmission line. It is an indispensable component of a cryogenic system, such as a superconducting transmission line. Ordinary gas expansion-compression refrigerators are expensive and limited to a relatively low efficiency (10 to 30% of Carnot). Theoretically, a magnetic refrigerator has the potential for much higher efficiency and lower cost and can be much more compact.

PROJECT OBJECTIVES

The objectives of this project were: (1) to develop and test a magnetic rotating-wheel refrigerator with design goals of 1000 W of refrigeration from +20°C to -20°C at 70% of Carnot efficiency and (2) to develop and test a high-efficiency reciprocating magnetic refrigerator.

PROJECT RESULTS

Both refrigerators were built and tested. Although it was quite an achievement to make such operational devices, the tests showed that the prototypes' power output and efficiency fell short both of the design goals and of what would be needed for a practical refrigerator.

Mario Rabinowitz, Project Manager
Electrical Systems Division

ACKNOWLEDGMENTS

We acknowledge the active participation of Professors William P. Pratt, Jr. (Michigan State University) and Donald R. Zrudsky (University of Toledo) in the building and testing of various components of the wheel refrigerator. Haskel Shienberg oversaw the gadolinium fabrication while Barney Geelan provided technical assistance. Jack Dyson machined and helped in the assembly of the intricate wheel refrigerator.

CONTENTS

Part A: ROTATING MAGNETIC REFRIGERATOR

Section	Page
1 INTRODUCTION	1-1
Principles of Magnetic Refrigeration	1-3
2 THEORY OF GADOLINIUM WHEEL	2-1
Thermodynamic Properties of the Ferromagnet, Gadolinium Metal	2-1
Theory of the Wheel Refrigeration	2-5
3 MAGNET AND DEWAR	3-1
Dewar	3-1
Magnet Design and Construction	3-4
4 WHEEL AND WHEEL HOUSING	4-1
Fluid Flow in an Actual Wheel	4-1
Entrained Action in an Actual Wheel	4-1
Construction of the Wheel	4-3
Construction of Wheel Housing	4-4
Wheel and Wheel Housing Tests	4-6
5 POROUS GADOLINIUM FABRICATION AND TESTING	5-1
Heat Transfer and Flow Friction in Fine Porous Media	5-1
Heat Transfer and Flow Friction in Gadolinium Chips	5-2
Design of Gd Sections	5-4
Actual Fabrication of Gadolinium Sections	5-10
Tests of Gd Sections in Assembled Wheel and Housing	5-12
6 FLUID HANDLING AND INSTRUMENTATION	6-1
External Heat Exchangers	6-1
Pumping System	6-1
Flow Measurements	6-3
Temperature Measurement	6-3
Wheel Drive	6-4
Torque Measurements	6-4
7 TESTS OF REFRIGERATOR	7-1
Initial Tests	7-1

7 TESTS OF REFRIGERATOR (continued)
Analysis of Initial Refrigerator Tests 7-2
Additional Refrigerator Tests 7-6
Final Analysis 7-15
Summary of Test Results 7-17
8 CONCLUSIONS 8-1
Refrigeration Power vs Magnetic Field 8-1
Efficiency vs Magnetic Field 8-2
Temperature Span ΔT vs Magnetic Field 8-4
Discussion of Experimental Magnetic Field 8-4
Discussion of Experimental Heat Exchanger 8-5
9 REFERENCES 9-1
APPENDIX A WATER REQUIRED FOR BALANCED FLOW A-1
APPENDIX B PUBLICATIONS AND TALKS B-1
EPRI PROGRESS REPORTS B-1
OTHER PUBLICATIONS AND TALKS RESULTING FROM THIS WORK B-1

Part B: RECIPROCATING REFRIGERATORS

1 INTRODUCTION 1-1
2 THEORY OF ACTIVE MAGNETIC REGENERATION 2-1
3 RESULTS ON ACTIVE MAGNETIC REGENERATION 3-1
Porous-Bed Heat Transfer Experiments 3-1
Gadolinium-Air Experiments 3-4
Gadolinium Water Experiments 3-10
4 CONCLUSIONS 4-1
5 REFERENCES 5-1
APPENDIX A SIMPLIFIED MODEL OF ACTIVE MAGNETIC REFRIGERATOR A-1

ILLUSTRATIONS

PART A

Figure		Page
1-1	Schematic diagram of magnetic Carnot refrigeration principles.	1-4
2-1	Magnetization of gadolinium metal.	2-1
2-2	Experimental and calculated entropy for Gadolinium metal.	2-2
2-3	Calculated entropy for GdN.	2-4
2-4	Calculated entropy for material like $GdAg_{0.8}\ In_{0.2}$.	2-5
2-5	Stirling-cycle wheel concept in refrigerator mode.	2-6
2-6	Thermodynamic cycle executed by Gd metal in the wheel.	2-7
2-7	Stirling-cycle wheel concept in the heat-engine mode.	2-8
2-8	Stirling-cycle refrigerator with nonideal heat exchange.	2-9
2-9	Solution of the heat-pump equations.	2-10
2-10	Fraction of Carnot efficiency of the heat pump.	2-13
3-1	Overall design of magnetic refrigerator.	3-1
3-2	Dewar before final assembly.	3-2
3-3	Perspective view of the magnet.	3-4
3-4	Magnetic field vs angular displacement.	3-9
3-5	Types of iron shields tested.	3-10
3-6	Measured force on iron shielding.	3-10
3-7	Magnetic field profile.	3-11
4-1	Details of the housing and wheel.	4-2
4-2	Cutaway of wheel and housing.	4-3
4-3	Cutaway of wheel and housing, along with the drive components.	4-4
4-4	Seal designs.	4-5
5-1	Microstructure of porous Gd.	5-3
5-2	Low flow velocity pressure drops per unit length and unit velocity for water through porous gadolinium pressings.	5-4
5-3	Porous gadolinium section.	5-8
5-4	The pressure drop of flow into wheel entrance port 8.	5-12

6-1	Exit heat exchanger construction.	6-2
6-2	Schematic of closed-cycle pumping system.	6-2
6-3	Torque table.	6-4
7-1	A black-box refrigerator used for energy and entropy balance calculations.	7-5
7-2	Measured entropy-temperature curves for gadolinium metal.	7-7
7-3	Heating load of the Gearchem pump as a function of the pressure drop.	7-10
7-4	A recording illustrating the flow patterns and pressure patterns at very slow rotation rate.	7-14
7-5	Temperature profile of the gadolinium.	7-14
7-6	Thermal load added by a heater in the cold, external heat exchanger.	7-16
8-1	Calculated refrigeration capacity as a function of filled change across wheel.	8-3
8-2	Calculated refrigerator efficiency as a function of field change across the wheel.	8-3
8-3	Calculated refrigerator span as a function of field change across wheel.	8-4

ILLUSTRATIONS

PART B

Figure		Page
3-1	Experimental Result for heat transfer of air in a Pb-ball porous bed.	3-3
3-2	Theoretical result for heat transfer of air in a Pb-ball porous bed giving a $N_{tu} = 25 \pm 15$.	3-4
3-3	Experimental Setup for gadolinium reciprocating heat pulse air refrigerator.	3-5
3-4	Experimental and theoretical force measurements for Gd-Air design No. 1.	3-8
3-5	Calculated forces for various components of Gd-Air design No. 1.	3-8
3-6	Temperature excursions of gadolinium and gas for Gd-air design No. 1.	3-9
3-7	Net force on gadolinium-air refrigerator.	3-11
3-8	Experimental Design No. 2. Temperatures of water entering and leaving the refrigerator.	3-13
3-9	Experimental refrigeration capacity versus temperature span.	3-13
3-10	Calculated temperature of water entering and leaving the refrigerator.	3-14
3-11	Calculated refrigerator capacity versus temperature span.	3-14

APPENDIX A

A-1	Simplified S - T curves for Gd metal	A-2
A-2	Thermal wave propagation through an active magnetic regenerator type of refrigerator.	A-2

TABLES

PART A

Table		Page
7-1	Energy and Entropy Sources in Refrigeration	7-5

SUMMARY

Since the early 1930s adiabatic demagnetization has been used to provide refrigeration at temperatures below 1 K. In the 1970s the potential of adiabatic demagnetization to provide efficient, reliable refrigeration from 1 K upwards was discovered. The research described here is the result of over two years (September 1, 1977 to June 30, 1980) of work on two types of magnetic refrigerators. The original aim of the research and development program was to provide more efficient refrigeration for superconducting technological applications in power generation and transmission. However, the work reported forms part of the basis for a whole new refrigeration technology with a myriad of applications.

As a first step toward development of the low-temperature refrigerator technology, a gadolinium-metal magnetic-wheel prototype was designed, built, and tested at room temperature with the objective of understanding the device in an experimentally convenient temperature region. When operating through a 6-Tesla magnetic-field difference, the wheel was designed to provide 1 kW of continuous refrigeration across a 40 K span near room temperature and to operate at 70% of Carnot efficiency. The device was designed to operate near 1 Hz for low-speed, high reliability performance. The prototype, when operating through a 1.2-T field differnce, provided 1/2 kW of continuous refrigeration over a 7-K span at 26% of Carnot efficiency. A thorough set of experiments and a complete analysis of the results were performed. The main limitation of the wheel prototype was the magnetic field profile, i.e. it was difficult to obtain a high, uniform field across the top of the wheel while simultaneously maintaining zero field across the bottom of the wheel. The profile problem along with magnet-quench problems limited the maximum field difference between the top and bottom of the wheel to $\sim$ 1.2 T. A second problem that occurred was fluid-flow control. The combination of seals, ports, and porous-bed impedance variation produced a transient flow that appeared to degrade the heat transfer significantly, although an exact analysis was difficult. The experimental value of the porous-bed heat exchange character was given by an

N_{tu} = 6, far below the design value of 160. The entrained fluid was a problem because transient flow reduced the effectiveness of a counterflow, compensating mechanism. The results on the wheel can be readily scaled by use of simple theory. If all the experimental parameters, except the magnetic field, are fixed, and if the field difference is increased from 1.2 T to 6.0 T, the wheel would pump 1.45 kW across 40 K with 65% of Carnot efficiency. Considering that comparable gas-based refrigerators have an efficiency of 10-30% of Carnot, the magnetic refrigerator looks very attractive.

A second magnetic refrigerator model, a simple reciprocating device was also designed, built, and tested with the objective of understanding the problems associated with this class of design for low-temperature applications. Two sets of experiments were performed, one using water as the heat-exchange fluid and the other using air. Both of these sets of experiments verified that the principle of this new type of device was understood and that the design has promise. The small apparatus using water provided up to 1/2 kJ/cycle of refrigeration, which was expected performance. The key problem uncovered in the reciprocating design is the compensation of large magnetic forces simultaneously with the reduction of parasitic heat leaks.

The key results of both sets of experiments show that the principles of magnetic refrigeration are clearly demonstrated and that no fundamental problems exist in the two designs that were tested. Prospects are good for a highly efficient, highly reliable device; but more study and careful engineering are required before commercially viable devices can be considered.

PART A

ROTATING MAGNETIC REFRIGERATOR

Section 1

INTRODUCTION

At the present time there are two general designs for magnetic refrigerators, the wheel-type and the reciprocating-type. Part A of this report described the results of an investigation of a particular wheel-type design. The study showed that the magnetic-field profile, the complex flow pattern requiring orifices, and the entrained fluid were the key problems in the wheel design. We decided that it was necessary to study the reciprocating-type design in order to learn about its problems before deciding which general design should be developed at liquid-helium temperatures. There were several different magnetic cycles that could be chosen for study such as the Carnot, Stirling or Brayton cycles but we also wanted to develop a refrigerator cycle that could span large temperature ranges if required. Therefore, we chose to develop a new idea, called active magnetic regeneration, which is the basis for a refrigerator that potentially executes a Brayton cycle over a wide temperature span.

limits for the operating requirements of a SPTL refrigerator. Thus if we seek to optimize SPTL refrigerator performance, we may choose some typical specifications and easily scale requirements for other situations from these. Accordingly we consider here the characteristics of machines providing between 1,000 and 5,000 W of refrigeration at operating temperatures, which might range from 4 to 14 K. At these temperatures the only fluid available for a working material and heat transfer medium is helium, having a normal boiling point of 4.2 K and a critical point of 5.2 K at 2.26 atm. Under most conditions considered for cooldown and steady state SPTL operation, the refrigerant helium will be in the supercritical state; but for cooling pothead leads liquid at 4.2 K is often preferred, so the machine should also be capable of performing as a liquefier.

Current cryogenic refrigeration technology has provided machines of about 1000 W capacity at 4 K, though there appears no technical reason why capacity cannot be extended to 5000 W. But the 1000-W machines are not off-the-shelf items, not only because the call for these is presently limited but also because each order has special specifications. All currently-used machines for 4 to 14 K service are of the gas-expansion type and have in common four principal elements: a feed-gas purification system; ambient temperature gas compression; low-temperature gas expansion; and gas-gas heat exchange. Modes of accomplishing these functions vary among the cryogenic refrigerator manufacturers, and some effort is now being expended to determine which modes and combinations thereof are best suited to such missions as SPTL. Criteria of importance in this comparison are:

Reliability. Very little long-term experience has accured for large helium refrigerators operating in the 4 to 14 K range; however, large machines using hydrogen near 20 K have run for 5,000 h or more without shut-down. Gas purity and wear of moving parts are of prime concern for long-term continuous operation.

Efficiency. The ideal thermodynamic, or Carnot, efficiency of a refrigerator is given by $[T_C/(T_H-T_C)]$, where T_C is the cold operating temperature and T_H is the ambient temperature. Thus for a machine operating between 300 and 4 K, the Carnot efficiency is 4/296 = 0.0135. But usually a refrigerator of 1000-W capacity will operate at only about 15% of Carnot efficiency, so to extract 1 W at 4 K requires an input energy of $(0.15 \times 0.0135)^{-1} = 494$ W to the ambient-temperature compressors. Greater efficiency can be obtained but only at a greater cost.

Cost. At present a 1000-W-at-4 K refrigerator costs somewhat more than $1,000,000. Costs for larger machines should scale somewhat less than linearly. Total installation costs for refrigeration station facilities to serve SPTL systems are considerably greater and depend strongly on the physical size of the refrigeration equipment. Estimates suggest that the costs of such facilities account for something like 10% of the SPTL transmission system costs.

Thus while current refrigeration technology could be successfully applied in SPTL systems, there is considerable room for improvement. And whereas progress in this direction for conventional machines can and undoubtedly will be made, such progress must consist of small steps. On the other hand, the potential of magnetic refrigeration indicates that a large step can be taken in a rather straightforward manner.

PRINCIPLES OF MAGNETIC REFRIGERATION

In 1925 Giauque(1) and Debye(2) independently suggested the use of magnetic refrigeration to produce temperatures below those previously attainable. The Nobel Prize winning work of Giauque and MacDougall(3) in 1933 used the method of adiabatic demagnetization of paramagnetic salts to cool from 3.5 K to 0.5 K. Until recently magnetic refrigeration has been used to produce temperatures to below 0.001 K and has been applied almost exclusively in situations requiring low power and very low temperatures; furthermore, the refrigeration has been accomplished using single-cycle ("one-shot") devices. Our purpose in the present work is to generalize and expand on these earlier ideas, to devise, construct, and operate continuous, high capacity magnetic refrigerators that ultimately span the range from very low temperatures to ambient temperatures.

Application of a magnetic field to paramagnetic materials at low temperatures and ferromagnetic materials near their Curie temperatures causes them to warm up; alternatively, heat is expelled from such materials if the temperature is held constant during the field application. Conversely, removal of the field will cool the material or, at constant temperature, allow absorption of heat by the material. The temperature changes can be of the order of 10 to 20 K if fields of about 7T are applied to an appropriately chosen material. The measured energy changes are large, being the order of hundreds of joules per liter of magnetic material in the liquid helium temperature range and tens of kilojoules per liter near room temperature.

The principle of a magnetic refrigerator can be illustrated with the conventional Carnot cycle device shown schematically in Figure 1-1. With Thermal Switch TS1 closed, Thermal Switch TS2 is opened and a magnetic field is applied to the paramagnetic or ferromagnetic working material (WM). The field aligns the magnetic spins in the working material, decreasing the randomness (i.e., entropy, S) of the spin system. The spin system is now in good thermal contact with the fixed temperature of the Heat Reservoir (HR), and heat will flow out of WM into HR. Next, TS1 is opened while TS2 remains open and the magnetic field is partially removed; the spin system becomes partially randomized, requiring energy and thus cooling WM to the temperature of the Heat Source (HS). TS2 is then closed while the magnetic field is decreased to zero, completing the spin-randomization process and allowing heat to be absorbed from HS. TS2 is then opened and a small magnetic field applied, so that WM warms to the temperature of HR. The cycle can be repeated if TS1 is closed as the full field is again applied to WM.

In order to apply magnetic refrigeration in large-scale practical situations, simple inexpensive refrigerator designs must be developed which permit a large quantity of heat to be removed rapidly from the low temperature heat source. The fundamental physics of magnetic refrigeration is well proven and does not require any further work. A magnetic refrigerator could embody several distinct advantages over conventional cryogenic refrigerators.

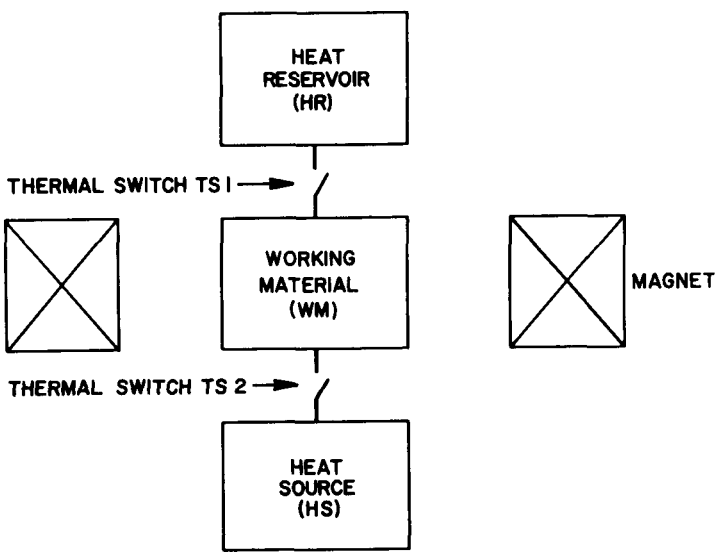

Figure 1-1. Schematic diagram of magnetic Carnot refrigeration principles.

The refrigeration power per unit volume is large. We are dealing with a solid, rather than a gaseous, working substance, and the density of the solid is about 50 times greater than that of the compressed gas at 20 atm and room temperature. The magnetic cycle can operate at nearly 100% of Carnot efficiency. For magnetic refrigeration, losses which lead to a drop from Carnot efficiency are readily anticipated an can be minimized. They are: heat flows across temperature gradients, frictional losses in moving parts or moving fluids, eddy current and hysteresis losses in magnet and refrigerator components, and heat leaks. Losses associated with finite spin-lattice relaxation times can be neglected, since spin-lattice relaxation times above 1 K are in the microsecond range. The aggregate of these losses will allow the overall magnetic refrigerator system to operate at about 70% of Carnot efficiency.

The working materials are inexpensive, about $30 per pound for rare earth ceramics, $200 per pound for rare earth metallic alloys in research quantities. Rare earths are more plentiful than Ge, Be, and many other elements.

As a result of the above three factors - small size, high efficiency, and inexpensive working materials - the entire system could be produced and operated for low temperature applications at substantial cost reductions when compared with conventional machines.

As there should be few moving parts in a magnetic refrigerator, it should be extremely reliable.

Section 2

THEORY OF GADOLINIUM WHEEL

THERMODYNAMIC PROPERTIES OF THE FERROMAGNET, GADOLINIUM METAL

Gadolinium metal is a ferromagnet with a Curie point at 294 K (21°C) at temperatures near this Curie point the application of a magnetic field will cause a partial electronic spin alignment and a corresponding entropy reduction. This is shown in Figures 2-1 and 2-2. The curves are calculated using the simplest model of a ferromagnet.

Thus because we are not interested in the physics of critical points and phase transitions, we have used the Weiss molecular field approach(4) and compared

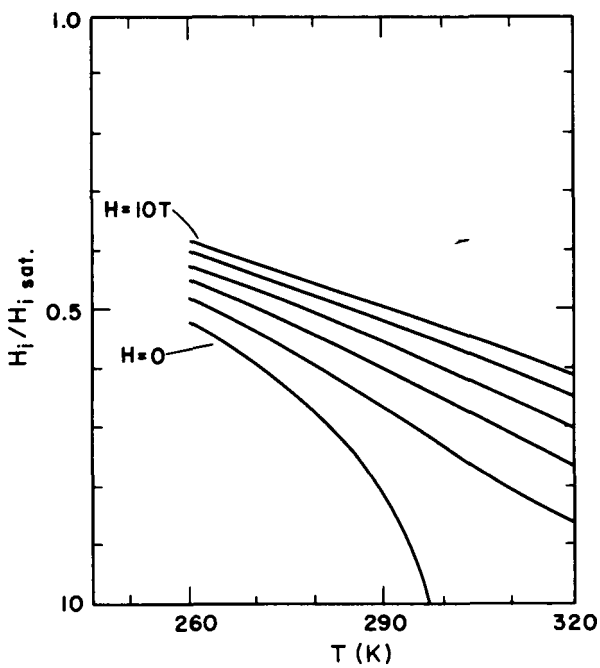

Figure 2-1. Magnetization(or internal field H_i) divided by corresponding saturation value for Gd metal for H=0,2,4,6,8, and 10T.

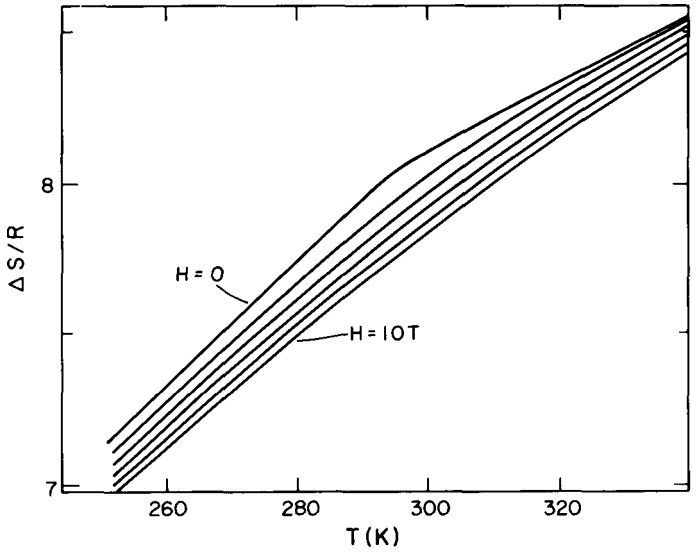

Figure 2-2. Experimental and calculated entropy for Gd metal. The experimental data at zero and 7T is within 0.01 of the calculated results at all temperatures and field, and thus not shown in this drawing.

the results with the two where experimental results are available. This model is quite simple, and lends itself to straightforward calculation on an HP 9830 programmable desk calculator. The model simply says that the effective field tendency to align a spin is given by the applied field, H, plus an internal field, H_i. H_i itself is proportional to the degree of alignment. The equation for H_i is

$$H_i = CB_J\left(\frac{\beta g(H+H_i)}{kT}\right) \tag{2-1}$$

where β is the Bohr magneton, g is the Lande g-factor, and k is Boltzmann's constant, and B_J is the Brillouin function for spin J. The intersection of the B_J curve and the H_i line for a given H represent a solution to Eq. 2-1.

The proportionality constant, C, is determined by the measured Curie temperature T_C. If $T=T_C$ and H=0 the initial slopes of the two curves

CB_J and H_i are equal (because, for $T \leq T_C$ there is by definition and by Eq. 2-1 spontaneous magnetization). The initial slope of the Brilloiun function is:

$$B_J\left(\frac{g\beta J}{kT} H_i\right) = \frac{J+1}{3J} \cdot \frac{g\beta J H_i}{kT} \tag{2-2}$$

by matching the initial slopes of the two curves

$$C \frac{g\beta(J+1)H_i}{3\ kT_C} = H_i \tag{2-3}$$

$$C = \frac{3kT_C}{g\beta(J+1)} \tag{2-3}$$

Thus, the equation that the calculator satisfies by trial and error is:

$$H_i = \frac{3\ kT_C}{g\beta(J+1)} B_J\left(\frac{g\beta J\ (H + H_i)}{kT}\right) \tag{2-4}$$

We have attempted unsuccessfully to take into account short range spin-spin correlations by introducing a small random field, H_r, such that (H_i+H) in Eq. 2-4 becomes $(H_i+H)^2 + H_r^2$ or that $B_J[\ldots(H + H_i)]$ becomes $1/2[(B_J(\ldots(H+H_i+H_r)) + B_J(\ldots(H+H_i-H_r))]$. Neither approach gave rise to the hoped for sharpening of the zero field specific heat peak just below T_C, and the zero field specific tail above T_C, With a little more thought, this could surely be corrected in a simple way. However, it is not necessary because as we shall see, the Weiss model is sufficiently accurate for our engineering application. It should produce error in the specific heat C_V and entropy S only in very small fields, very near the Curie point. As one way of finding a numerical solution of Eq. (2-4) in zero field near and above T_C, we have maintained a very small random field so that H_i+H becomes $(H_i+H)^2 + H_2^2$. This gives rise to small C_V and smaller than measured unphysical, but negligible spontaneous magnetization above T_C.

The magnetization and entropy calculated for Gd metal are shown in Figures 2-1-2. The lattice and electronic contribution to C_V/R has been taken(5) as $2T^{0.1}$; this small temperature dependence of C_V is due to the electronic

contribution and the fact that the relevant temperatures are slightly below that where the lattice C_V/R saturates at 3. Note that these calculations have no free parameters other than the nonmagnetic C_V and and additive constant to $S/R(H_2$ is taken as negligibly small, g and T_C are established properties of Gd metal). The gas constant is R.

Figure 2-2 shows $\Delta S/R$ versus field and temperature for Gd. For comparison with experimental data in both Gd and Fe (not shown), we examine experimental zero field entropy curves based on zero field C_V measurements, and non-zero field entropy curves based on measurements of the magnetocaloric effect. It is the temperature change with the application of a field which is most difficult to find data on and most important for our work. Based on similar materials, we can guess the lattice C_V for other materials and calculates $\Delta S/R$ vs T for various other ferromagnets(6) as shown in Figures 2-3 and 2-4.

To draw some qualitative conclusions we see that

1. The entropy removal near T_C for a given H goes more or less like $1/T_C$ of the material.

2. Between room temperature and liquid nitrogen temperature the lattice contribution to entropy changes is largest. This is because lattice C_V is rather large in that region, and because $\Delta S = (C_V/T)\Delta T$; C_V/T drops off at higher or lower temperatures for most materials.

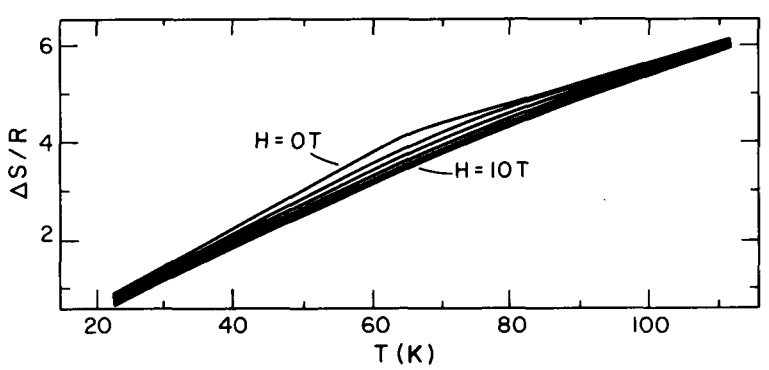

Figure 2-3. Calculated entropy for GdN. Parameters used were $C_{non-mag}/R = 0.042T$, J = 3.5, g = 2, T_C = 65 K, and H1 = 0.3 T.

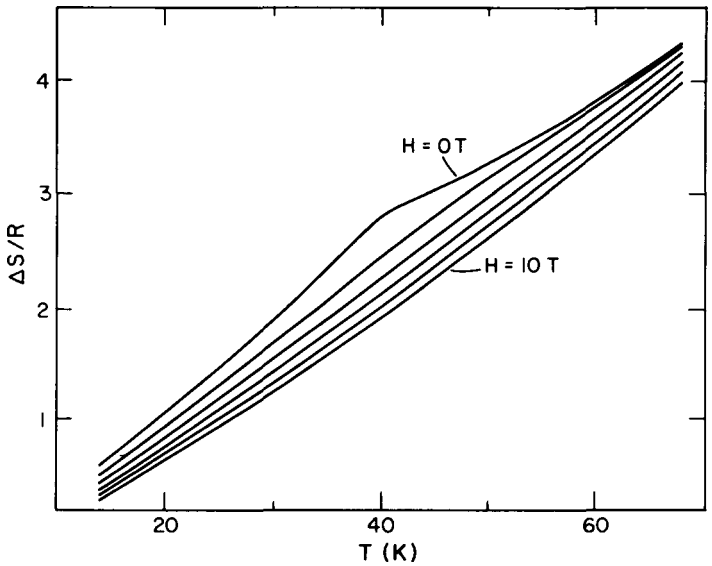

Figure 2-4. Calculated entropy for material like Gd $Ag_{0.8}In_{0.2}$. Parameters used were $C_{non\text{-}mag.}/R = 10^{-3}\,T^2$, J = 3.5, g = 2, T_C = 40K. These results show roughly the expected behavior of Gd based materials with T_C near 40K.

THEORY OF WHEEL REFRIGERATION

Concept

Figure 2-5 illustrates the operation of the magnetic Stirling-cycle wheel as a refrigerator(7). At the lower right-hand side, the fluid at T^H enters the porous wheel; in the perfect, conceptual device, the wheel is also at T^H at this point. The fluid flows through the porous wheel, in contact with the wheel which was at temperature T^C after leaving the high-field region. It heat exchanges with the wheel, exiting the wheel at temperature T^C, the same temperature as the wheel (again in the case of perfect heat exchange and flow balance). The fluid warms by an amount Δ, picking up heat Q_C from the low-temprature heat source and reenters the wheel at temperature $T = T^C + \Delta$. In exchange with the wheel which was at temperature $T^H + \Delta$ after entering the high-field regin, the fluid warms to $T^H + \Delta$. It deposits the heat Q^H in the high-temperature heat sink, completing the cycle as it reenters the wheel at temperature T^H. Note that in this idealized system no heat flows across any large temperature gradient as would be the case if the fluid entered or left the wheel at a temperature appreciably different from the wheel temperature at that point.

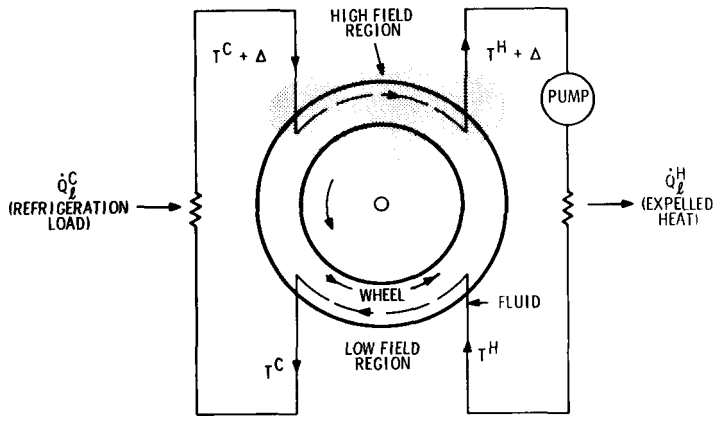

Figure 2-5. Stirling-cycle wheel concept in refrigerator mode. Ideal heat transfer with T_H, etc. being the temperature of the wheel and fluid at that point; Δ is the inherent temperature change of the working material upon entering and leaving the field.

Figure 2-6 shows the thermodynamic cycle described above but viewed in terms of the Gd-metal working material. It warms from T^H to $T^H + \Delta$ upon entering the field, is cooled by the fluid in the field, etc. The area of the parallelogram like figure represents the amount of work W put into the Gd each cycle, which for 1 ℓ (50 moles) of Gd is

$$\Delta \sim 50 \times \Delta S \times (\Delta) = (50)(1.35)(8.3)(8) = 4.5 \text{ kJ}. \qquad (2\text{-}5)$$

In the idealized system, all this work goes into pumping heat (many times 4.5 kJ with 100% of Carnot efficiency). If the arrows in Figure 2-6 were reversed, we would have the heat engine in Figure 2-7 producing 4.5 kJ of energy per cycle. This amount of work may seem large, but it should be noted that Gd is a very magnetic metal, about as magnetic as Fe. Thus, when a large amount of Gd at a lower temperature is pulled into the high field of a superconducting magnet, a large amount of work is done. A much smaller amount of work is required to remove the warmer less magnetic Gd from the field.

Simplifying Approximations

Reference 7 calculates the properties of the two fluid-wheel heat exchangers of Figure 2-5. To make the equations linear, we have assumed a constant

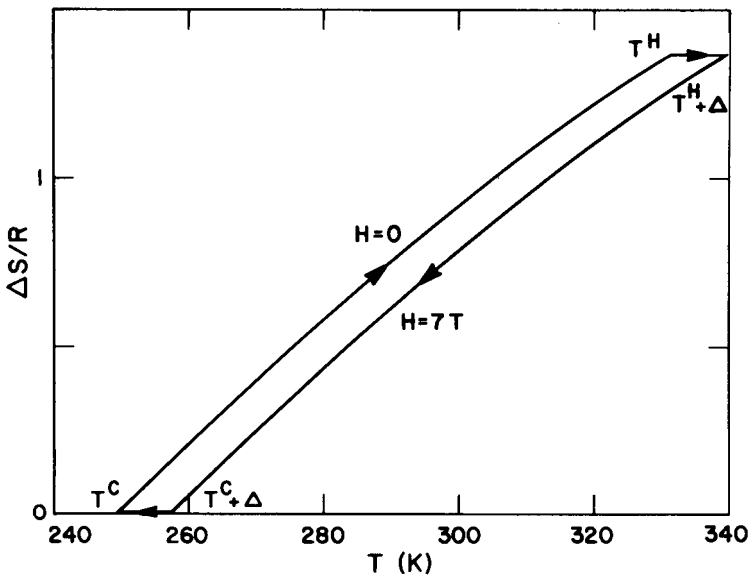

Figure 2-6. Thermodynamic cycle executed by Gd metal in the wheel. The parallelogramlike shape is an approximation to the actual entropy curves of Gd and to the specific-heat approximation used in our calculation [Eq. 2-6]. In this figure, R is the gas constant.

(temperature-independent) specific heat for the fluid (a very good approximation, particularly if the fluid is water) and for the working material.

Another approximation that was made in our conceptual device and in Figure 2-5 was that the Δ's at the high- and low-temperature ends of the cycle are the same, namely, 8 K (smaller than the 14 K value at the Curie point). This is thermodynamically inconsistent with the approximation of the same constant specific-heat value at high and zero magnetic fields. If the specific heat is C, and referring to Figure 2-6 and allowing for two values of Δ, Δ^C, and Δ^H, we obtain

$$S(T^H) = S(T^C) + \int_{T^C}^{T^H} \frac{C\,dT}{T} = S(T^C) + C \ln \frac{T^H}{T^C} \qquad (2\text{-}6)$$

and

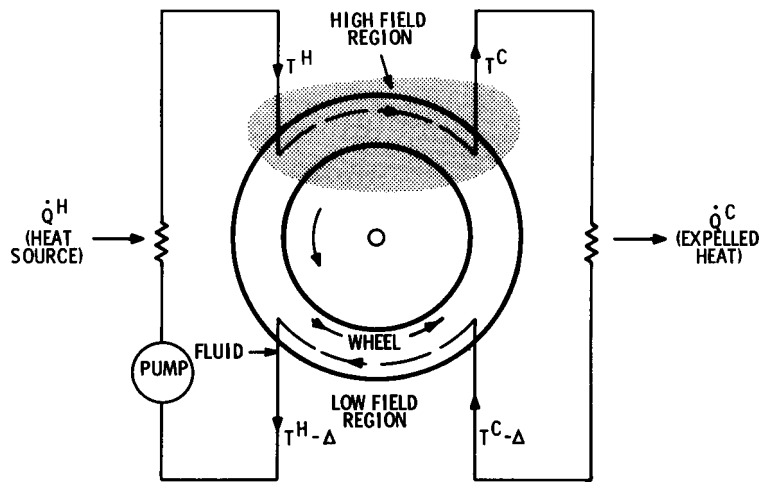

Figure 2-7. Stirling-cycle wheel concept in the heat-engine mode.

$$S(T^H + \Delta^H) = S(T^C + \Delta^C) + \int_{T^C+\Delta^C}^{T^H+\Delta^H} \frac{C\,dT}{T}$$

$$= S(T^C + \Delta^C) + C \ln \left(\frac{T^H + \Delta}{T^C + \Delta} \right); \qquad (2\text{-}7)$$

because $S(T^H) = S(T^H + \Delta^H)$, and $S(T^C) = S(T^C + \Delta^C)$, we have

$$\frac{T^H}{T^C} = \frac{T^H + \Delta H}{T^C + \Delta^C} \qquad (2\text{-}8)$$

or

$$\frac{\Delta^H}{\Delta^C} = \frac{T^H}{T^C} \quad . \qquad (2\text{-}9)$$

Thus, for Gd, if $\Delta^C = 7$ K, then $\Delta^H = 9.3$ K to be consistent with thermodynamic requirements. Our calculations will take Eq. 2-9 into account. However, this will limit the validity of these calculations to materials like Gd which have $C_v(H=0) \approx C_v(H \neq 0)$, as deduced from Figure 2-2.

Expected refrigerator performance

Figure 2-8 shows the refrigeration system; Figure 2-5 is the case of a nonideal heat transfer in the exchangers of the wheel. The fluid may be at a different temperature from the wheel where it enters and leaves; thus, heat flows irreversibly across a temperature difference. We must now calculate the refrigerator performance when this irreversibility is taken into account.

Appendix A of ref. 7 shows that in two counter flowing materials (wheel working material, subscript w and fluid subscript f) in heat exchange and with advanced flow ($\dot{m}_w C_w = \dot{m}_f C_w$)
that

$$T_w^r = T_w^\ell - [T_r^\ell - T_w^\ell] N_{tu} \qquad (2\text{-}10)$$

and

$$T_f^r = T_f^\ell - [T_f^\ell - T_w^\ell] N_{tu} \qquad (2\text{-}11)$$

In the above discussion $\dot{m}$'s are the mass flow rates and C's are the specific heats per unit volume. The superscript ℓ and r apply to the left and right and sides of the exchangers of Figure 2-8.

We can apply Eqs. 2-10 and 2-11 to the two heat exchangers of Fig. 2-9, to obtain a relation between the temperatures of the two materials on one side of exchanger in terms of the temperatures of the materials on the other side.

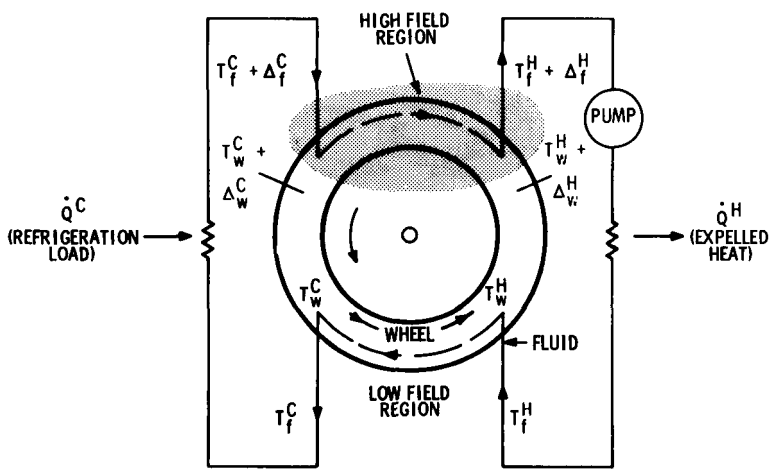

Figure 2-8. Stirling-cycle refrigerator with nonideal heat exchange.

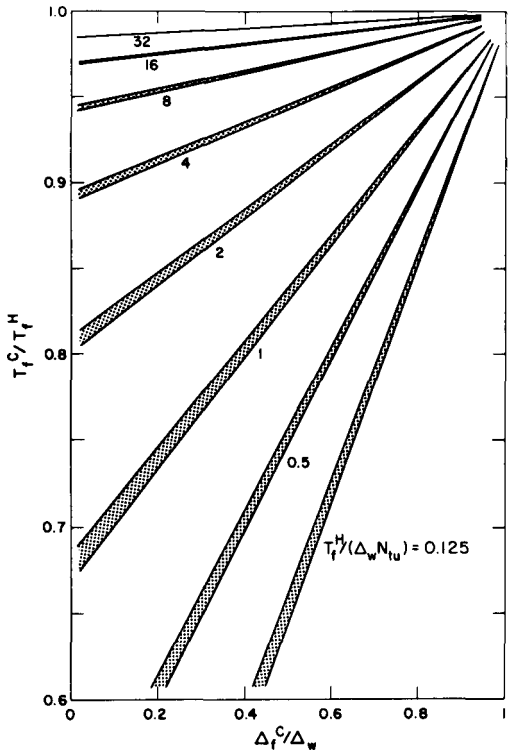

Figure 2-9. Solution of the heat-pump Equation (2-13) in terms of dimensionless parameters. T_f^C/T_f^H versus Δ_f^C/Δ_w for various values of $T_f^H/\Delta_w N_{tu}$. The results are slightly dependent on the value of Δ_w/T_f^H. If $\Delta_w/T_f^H = 0.1$, the upper part of the appropriate shaded area should be used; for $\Delta_w/T_f^H = 0.001$, the lower part shoud be used. The nomenclature is explained in the text.

If we take $\Delta_w^H = \Delta_w$ and $\Delta_w^C = T_w^C \Delta w / T_w{}^H$ as in Eq. 2-9. we have

$$T_w^C = T_w^H - (T_f^H - T_w^H)\, N_{tu}\,, \tag{2-12a}$$

$$T_f^C = T_f^H - (T_f^H - T_w^H) N_{tu} \tag{2-12b}$$

$$T_w^H + \Delta_w = T_w^C + T_w^C \Delta_w/T^H - (T_f^C + \Delta_f^C - T_w^C - T_w^C\Delta_w/T^H)\, N_{tu}, \tag{2-12c}$$

$$T_f^H + \Delta_f^H = T_f^C + \Delta_f^C - (T_f^C + \Delta_f^C - T_w^C - T_w^C\, \Delta_w/T_w^H)\, N_{tu}\ . \tag{2-12d}$$

In these four refrigerator equations, we will specify N_{tu} (the exchanger quality), T_f^H (the temprature of the high-temperature heat reservoir), Δ_w (the temperature change of the working material of the wheel upon entering the high field), and Δ_f^C (the temperature change of the fluid when it picks up energy, $\dot{Q}^C = \dot{m}C\Delta_f^C$). We will solve for T_f^C (the temperature of the heat source for the refrigerator), Δ_f^H (the temperature change of the fluid as it gives up energy $\dot{Q}_H = \dot{m}C\Delta_f^H$) and T_w^H and T_w^C (the wheel temperatures which are not of direct interest to the refrigerator performance). These quantities are illustrated in Figure 2-8.

We now have four equations to solve for the four unknowns, T_f^C, Δ_f^H, T_w^H, and T_w^C. Except for deviations from unity of T_w^C/T_w^H on the right-hand side of Eqs. (2-12c) and 2-12d), these are straightforward linear equations whose solutions are

$$T_f^C = T_f^H + \Delta_f^C N_{tu}/2 - [(1+N_{tu}^{-1})T_w^C/T_w^H - N_{tu}^{-1}]\Delta_w N_{tu}/2 \tag{2-13a}$$

$$T_w^C = T_f^H + (1 + N_{tu}^{-1})\Delta_f^C N_{tu}^{-1}/2 - (1 + N_{tu}^{-1}) \times [(1 + N_{tu}^{-1})T_w^C/T_w^H - N_{tu}^{-1}]\Delta_w(N_{tu}^{-1}/2) \tag{2-13b}$$

$$T_w^H = T_f^H + 1/2\ \Delta_f^C - 1/2\ [(1 + N_{tu}^{-1})T_w^C/T_w^H - N_{tu}^{-1}]\Delta_w, \tag{2-13c}$$

and

$$\Delta_f^H = \Delta_f^C + (1 - T_w^C/T_w^H)\Delta_w. \tag{2-13d}$$

As $T_w^C = T_w^H$ (which is near unity in cases of interest) appears on the right-hand side of Eqs. 2-13a-d, we solve these by iteration. We can also calculate the thermodynamic efficiency of the device, compared to Carnot efficiency. The work put into the system is, by conservation of energy

$$\Delta = \dot{m}C(\Delta_f^H - \Delta_f^C), \tag{2-14}$$

and the refrigeration power is

$$\dot{Q}^C = \dot{m}C\Delta_f^C \ . \tag{2-15}$$

Thus, using Eq. (2-13d) we obtain

$$\left(\frac{\Delta}{\dot{Q}^C}\right)_{\text{actual}} = \left(1 - \frac{T_w^C}{T_w^H}\right)\left(\frac{\Delta_w}{\Delta_f^C}\right) \tag{2-16}$$

while for a Carnot efficiency

$$\left(\frac{W}{Q^C}\right)_{\text{Carnot}} = \frac{T_f^H + \frac{1}{2}\,\Delta T_f^H}{T_f^C + \frac{1}{2}\,\Delta_f^C} - 1. \tag{2-17}$$

This approximate equation takes into account that heat is absorbed (or deposited) evenly between temperatures T_f and $T_f + \Delta_f$. If Δ_f becomes comparable with T_f, Eq. (2-17) would need modification. Now, η equals Eq. (2-17) divided by Eq. (2-16) (the ratio of the Carnot to the actual work required to pump heat $\dot{Q}^C$).

It is convenient to plot the numerical solution to Eq. (2-13), as in Figure 2-9, i.e., T_f^C/T_f^H as a function of Δ_f^C/Δ_w.

The fraction of Carnot efficiency η is nearly equal to Δ_f^C/Δ_w. Figure 2-10 shows a plot of η as a function of Δ_f^C/Δ_w.

In Figure 2-9, the curves end in the upper right-hand corner, $T_f^C/T_f^H = \Delta_f^C/\Delta_w = 1$, and have a slope nearly equal to$[2\ T_f^H/(\Delta_w N_{tu})]^{-1}$ for larger values of $T_f^H/(\Delta_w N_{tu})$, i.e.,

$$T_f^C/T_f^H \sim 1 - [1 - (\Delta_f^C/\Delta_w)]\Delta_w N_{tu}/2T_f^H. \qquad (2\text{-}18)$$

From Figures 2-9 and 2-10, we see that for high efficiency we require Δ_f^C/Δ_w as large as possible; but, in order to get a large temperature difference, $T_f^H - T_f^C$, with large Δ_f^C/Δ_w, we need a small $T_f^H/\Delta_w N_{tu}$.

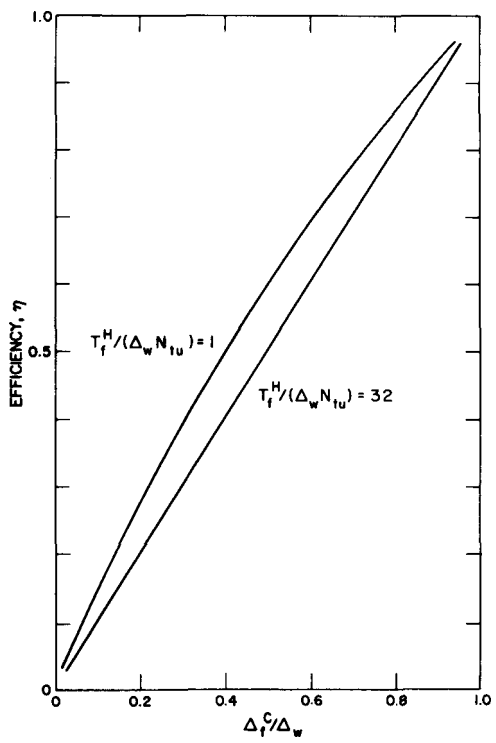

Figure 2-10. Fraction of Carnot efficiency of the heat pump in terms of the dimensionless parameter Δ_f^C/Δ_w and $(\Delta_w N_{tu})$. The dependence on Δ_w/T_f^H is too small to be seen in this figure.

Reference 8 discusses a concrete example of the use of these equations and also solves the problem of the heat engine with non-ideal heat exchange.

Section 3

MAGNET AND DEWAR

DEWAR

Dewar Design

The main dewar requirements are simplicity and reliability. In addition, the helium boil off should be low enough that the dewar will not warm to liquid nitrogen temperature over night, this will make the next days helium transfer quick and inexpensive. Also, the dewar bottom must be specially shaped to allow access for the Gd wheel as shown in Figure 3-1. The inner dewar bottom must be strong enough to withstand the combined vacuum and magnetic forces. Atmospheric pressure will push the bottom down and the reaction force on the magnet (from the magnetic wheel and magnetic shielding) will attempt to pull the magnet through the dewar bottom. At the same time the inner and outer dewar bottom must be thin enough to allow the wheel to be fully inserted into the bore of the magnet.

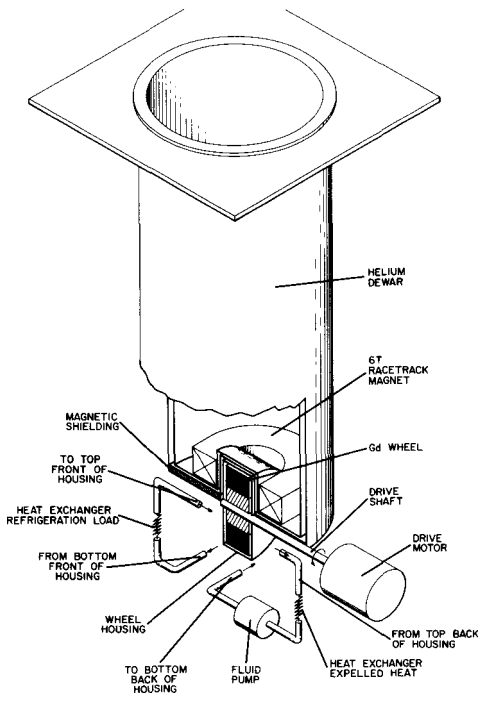

Figure 3-1. Overall design of magnetic refrigerator.

Figure 3-2 shows the dewar before assembly.

Dewar Construction and Testing

After the dewar was carefully leak-checked, it was insulated using polyester paper and double-sided aluminized Mylar. The total thickness of one sheet of paper and one sheet of Mylar was 0.005 cm. To improve the removal of residual gas from the insulation, slices 2 to 3 cm long about 6 to 10 apart were made in the Mylar and paper. Then 30 layers of paper and Mylar were loosely wrapped around the sides of the inner wall of the dewar to a total thickness of 3 cm. The bottom of the dewar had only 20 layers of paper and Mylar because of the restricted space. To maintain a good vacuum in the

Figure 3-2. Dewar before final assembly. The Dewar, shown schematically in Figure 1, relies on superinsulation and does not have a liquid nitrogen jacket.

dewar, $\sim 90 cm^3$ of activated carbon granules (16 to 20 mesh) were distributed between the layer. The charcoal pumped residual gas produced by outgassing from the Mylar and paper.
In the dewar neck, two baffles were placed 10 and 25 cm from the top of the dewar. They were made from 2.5-cm-thick styrofoam coated on top and bottom with 0.058-cm aluminum foils. Appropriate fill and lead holes were cut in the baffles, but otherwise they were within $\sim$3 mm of the wall. This caused the helium gas to cool the walls as it came out of the dewar.

The temperature measurements on the dewar were taken with copper-Constantan thermocouples made from 0.0079-cm-diam wires. The thermocouples were calibrated and then mounted. Four thermocouples were soldered to the inside dewar wall at 10, 25, 40, and 55 cm from the bottom of the dewar. One thermocouple was glued in contact with the center of the bottom baffle, and two more thermocouples were placed in the gas stream between the baffles and the wall of the dewar. The output of the thermocouples was recorded continuously on two 4-pen recorders.

The helium boil-off rate was measured with a flow meter and with a dip stick. Helium was transferred to a height of $\sim$30 cm (equivalent to $\sim$18ℓ). The boil-off was rapid immediately after transfer, but within 1 to 2 h it dropped significantly to a steady 1.0 to 1.2 ℓ/h. The wall and gas temperatures were essentially equal all the way up the dewar walls, which indicates excellent heat transfer and very efficient use of the enthalpy of the helium gas. The bottom-baffle temperature was between 4 and 20 K, which indicates that the "thermosiphon" effect(8) was present. To reduce the heat leak from thermal siphoning, we tried two different batting in separate tests. The first was 15 cm of a type of fiber glass batting normally used for house insulation. The batting was cut to fit tightly against the inside wall of the dewar between 25 and 40 cm from the bottom of the dewar; that is, just below the bottom baffle. The second batting was loosely wrapped glass wool that had $\sim$3 cm clearance between it and the dewar wall. As with the fiber glass, a 15-cm section was placed just below the bottom baffle. Neither of these battings produced a significant reduction in boil-off rate, although both gave a marginal improvement. The conclusion of these dewar experiments is that the radiation heat leak into the dewar through the insulation on the walls and bottom is the dominant heat leak. An analysis of this heat leak gave a mean

thermal conductivity of the insulation of 0.75 μW/cm K, which is very respectable and below the "rule of thumb" value of 1 μW/cm K. Thus the dewar performed as designed and it turned out to be 100% reliable during the magnetic refrigerator operation.

MAGNET DESIGN AND CONSTRUCTION

The magnetic field for the Gd wheel must have a special profile because of the wheel shape and the field requirements during the cycle. The top third of the wheel must be in a field of ≥ 6 T while the bottom third must be in a field of ~ 0. The most effective shape for production of the required magnetic field is a tiered racetrack because it puts the windings as close as possible to the wheel over an extended distance. The magnet windings also must be very compact. To obtain such a high field with a very compact magnet our calculations and meaurements show that near short-sample performance is required of the superconducting wire used in the magnet. The magnet finally decided upon is shown in Figure 3-3.

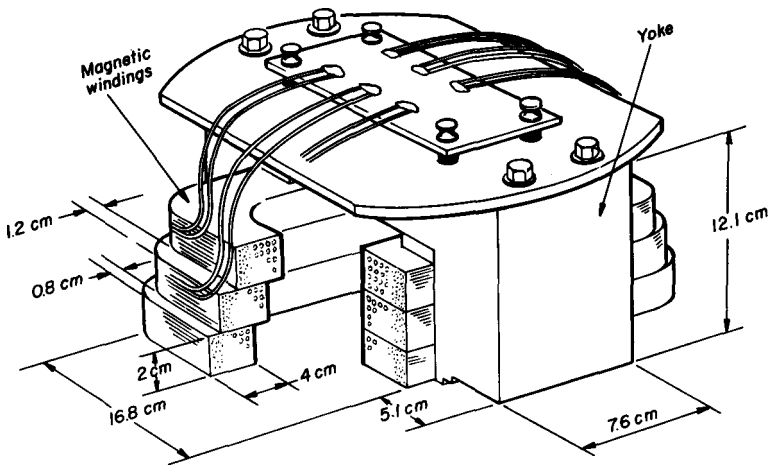

Figure 3-3. A perspective view of the magnet illustrating all typical dimensions. The inner half of each of the three coils is made of 0.75-mm-diam 1-to-1 copper to NbTi ratio wire, whereas the outer half is 0.50-mm-diam 2-to-1 ratio wire. There are 422, 442, and 436 turns on the upper, middle, and lower inner halves respectively, and 882, 963, and 1022 turns in the outer halves.

Magnet stability in this geometry is a problem. The outward force on each of the two long legs of the racetrack is 267 kN (30 tons); a heavy yoke made from 18% Ni Maraging 300 steel [yield stress 1.72 GPa (250 000 psi)] is used to confine this force. The magnet itself is wet-wrapped with epoxy to prevent the motion of individual wires.

The choice of the epoxy to give optimum performance is critical. A variety of epoxies were tested here. The thermal expansion coefficients and the integrity of epoxy bonds to copper and molybdenum have been tested between room temperature and liquid nitrogen temperatures. Shell Epon 828 with diethanolamine elevated-temperature cure hardener and Stycast 2850 FT with elevated-temperature cure Catalyst 11 were teted. Various proportions of aluminum oxide were added as filler to the unfilled Epon and the already filled Stycast. Stycast with 23 vol% 240-mesh fused alumina was best. Note that fine, nonfused alumina is not suitable. It has a tap density of 0.5 g/cm^3 compared to 3.2 g/cm^3 for solid alumina and 1.3 g/cm^3 for our fused alumina. (Tap density is the weight per unit volume of powder when poured into a container and tapped several times.) Later tests with unfilled and alumina-filled Crest 7380 A and 7380 B with elevated-temperature cure proved that Crest was superior in tenacity to the other epoxies. The Crest is a polyurethane reported to maintain some degree of flexibility at 77 K. Because not much thermal contraction occurs between 77 and 4 K, thermal stresses and cracks are minimized.

Thus, for our magnet we use Crest 7380 A and 7380 B along with fused Gd_2O_3 (gadolinia) as a cermic filler. This material has a large specific heat at $\sim$4 K (about 700 times that of copper) so we were able to increase the magnet's overall specific heat by about an order of magnitude, providing additional stability against thermal fluctuations.

To accommodate the high fields at the corners of the windings, the inner 2 cm was wound with 0.75-mm-diam multifilamentary NbTi wire with a copper-to-superconductor ratio of 1 to 1. The outer 3 cm of winding was 0.5-mm-diam Supercon multifilamentary NbTi wire with a copper-to-superconductor ratio of 2 to 1. We have used the latter type of wire successfully in a smaller magnet of this same shape. This particular wire is left over from a previous magnetic energy storage project.

Calculations

The dimensions of the windings were obtained by calculating the field produced by rectangular coils of varying dimensions. The method for these calculations is described below (9).

The magnetic field B is given by

$$\underset{\sim}{B} = \underset{\sim}{\nabla} \times \underset{\sim}{A} , \qquad (3\text{-}1)$$

where $\underset{\sim}{A}$ is the magnetic vector potential. $\underset{\sim}{A}$ is related to the current density $\underset{\sim}{J}$ according to

$$\underset{\sim}{A}(x_0, y_0\ z_0) = \frac{\mu_0}{4\pi}\int \frac{\underset{\sim}{J}(x, y, z)}{r}\ dV , \qquad (3\text{-}2)$$

where (x_0, y_0, z_0) is the point at which the field is calculated, (x, y, z) is the location of the current element, r is the magnitude of the length vector that connects (x_0, y_0, z_0) and (x, y, z), and dV indicates a volume integral. In the rectangular coil, the volume integral reduces to a line integral; that is $\underset{\sim}{J}\ dV = \underset{\sim}{I}\ dx$. Because $\underset{\sim}{A}$ and $\underset{\sim}{J}$ are collinear vectors, A_x is the only nonzero component from two parallel sides of the rectangle, and A_y is the only nonzero component from the remaining two sides. Because $A_z = 0$, the components A_x and A_y at (x_0, y_0, z_0) were calculated for a grid of points that describe the location of current density. This calculation was repeated at each point in a second grid where the field was required. The magnetic field components and total magnitude were then calculated.

The magnetic field calculation was performed on a Hewlett-Packard 9830 computer. The program was checked by letting the long dimension of the coil be ∿100 times greater than the short dimension. The field then approximates the easily calculated field for two parallel wires.

The calculation was repeated for several different current densities and coil dimensions, from which we selected the final dimensions of the coil to achieve a homogeneous field of 6 T. The predicted homogeneity was ∿10% over the upper third of the gadolinium wheel, and the field decreased rapidly below the windings. The results verified that the field is highest in the corners of

the rectangle, with the ratio of the maximum field at the corner to the field at the center of the magnet ranging from 1.3 to 1.4. From these calculations and mockup coil measurements, we decided that the inner half of each layer should be wound with 0.75-mm-diam multifilamentary NbTi wire and the outer half should be wound with 0.5-mm-diam multifilamentary NbTi wire. The dimensions of the coil we constructed are shown in Figure 3-3.

Yoke Design

The direction of the magnetic forces in the rectangular coil can be found using

$$\underset{\sim}{dF} = i\, \underset{\sim}{d\ell} \times \underset{\sim}{B} \,, \qquad (3\text{-}3)$$

where $\underset{\sim}{dF}$ is the force increment and i is the current flowing in a coil segment $\underset{\sim}{d\ell}$. The magnetic forces tend to compress the coils vertically and expand them radially; that is these forces tend to make the coils circular. Therefore the largest stress will occur in the corners of the magnet. An estimate of the forces between the long segments of the rectangular coil can be obtained from Eq. 3-3 by approximating the segments as parallel wires. The resultant force is 2.7×10^5 N ($\sim$30 tons) Maraging steel, has sufficient strength to contain the magnetic forces. The dimensions of the constructed yoke are shown in Figure 3-3.

Details of Construction

The magnet was wound on a coil winder using aluminum forms coated with Teflon sheet. Three separate coils were wound and then epoxied together using Stycast 2850 GT. After preliminary field measurements, these coils were epoxied into the yoke with Stycast. Junctions were made between all the inner, larger wire coils and also with all the outer coils. The junctions consisted of PbSn solder over $\sim$5 cm of adjacent wires laid on a printed circuit board. Leads were attached in a similar way but also had a 1- by 0.094-cm high-purity copper backing strip. The leads(10) to the inner and outer coils were separated to maintain the option of operating the coils at different currents.

Magnet Tests

The dewar and superconducting magnet were installed in the refrigerator stand and tested. As a part of this test, we developed a method for mounting and

locating a Hall probe in three dimensions. A 1-cm grid with (0,0,0) located in the center of the gadolinium wheel was used to locate the x-, y-, and z-component field measurements, which were taken with a Bell Model 640 gaussmeter.*

The extensive data, consisting of three component values at each grid point, were interpolated and converted into magnitudes only in the vicinity of the intended location of the gadolinium wheel. The data then were reduced to the field plots shown in Figure 3-4, which shows the field vs angular displacement from the top of the wheel, only at the radius of the center of the gadolinium. There are three separate field plots shown in Figure 3-4; one has no shield and the other two use ARMCO iron donut-type shields. The three types of shields, each with a total volume of about 1700 cm^3, were tested (Figure 3-5). A significant reduction from 0.6 to 0.2 T in the lowest part of the wheel was achieved with almost no loss of peak field over a total 90^0 sector at the top. Because the three types of shields were similar in their field shaping ability, the wing-type shield data were not pursued as extensively.

The most important information gained from the field plot (Figure 3-4) is that the amount of shield material used is the strongest factor in achieving the desired field shaping. Additional benefits from geometrical variations in the shield shapes are secondary.

The force (Figure 3-6) exerted on the three types of shields discussed in Figure 3-6 was measured using a three-point ball bearing suspension system, where the load cell was used in one of the three points. Two force measurements were made for each shield, with the load cell placed alternately in each of two positions. The force from the third position was calculated by symmetry. The three-point forces were summed to give the total force on the shield as a function of maximum magnetic field (Figure 3-6). The greater than linear growing rate of force per increment of applied field at low fields most likely is due to saturation in the shield material at low fields.

---

* Manufactured by F. W. Bell, Inc., 1356 Norton Avenue, Columbus, OH 43229.

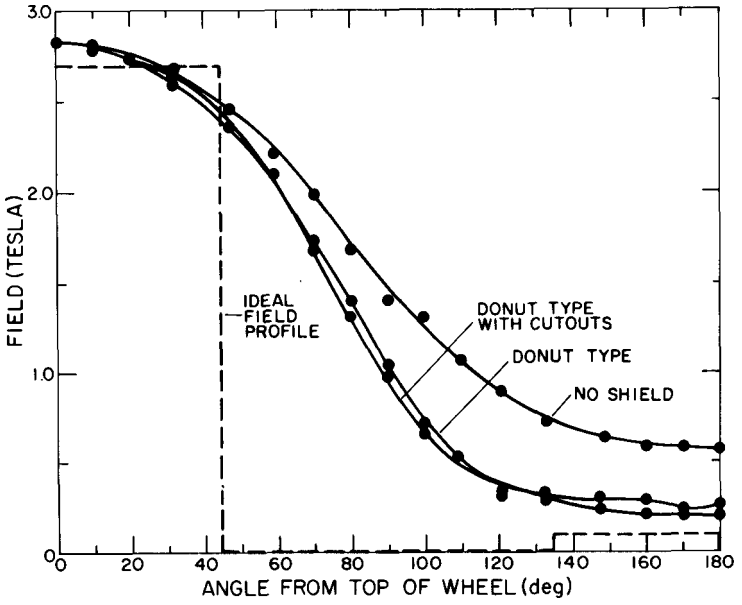

Figure 3-4. Field vs angular displacement from top wheel, as measured at the center of a section through the gadolinium at that angle.

The large reaction forces produced on the magnet by the shielding preclude the use of shielding to shape the magnetic field (the magnet could be pulled through the bottom of the dewar--even at small fields the dewar bottom makes large noises as the field increases if a shield is present). The nonuse of shields is a major and unforeseen problem in the program.

The magnetic field profile shown in Figure 3-4 was inferred from these measurements and indicates a major limitation of the present wheel design. The important field change is across the adiabatic section, from the 8-to-10-o'clock and 2-to-4o'clock positions in Figure 3-7, and is only ∿37% of the maximum field produced by the magnet. The gadolinium homogenizes the field within itself.

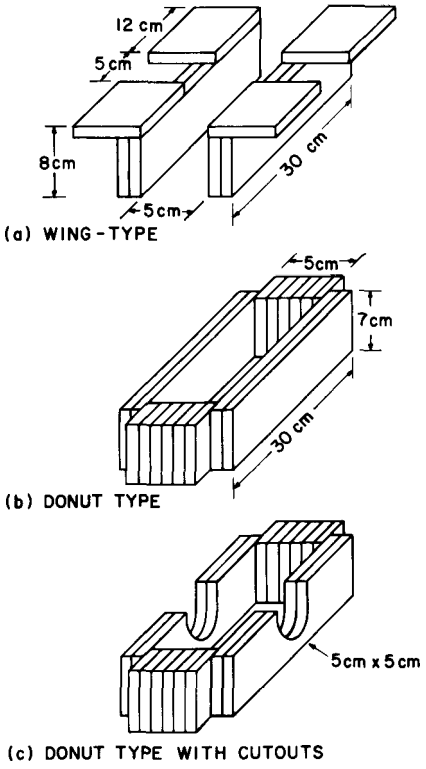

Figure 3-5. Types of iron shields tested.

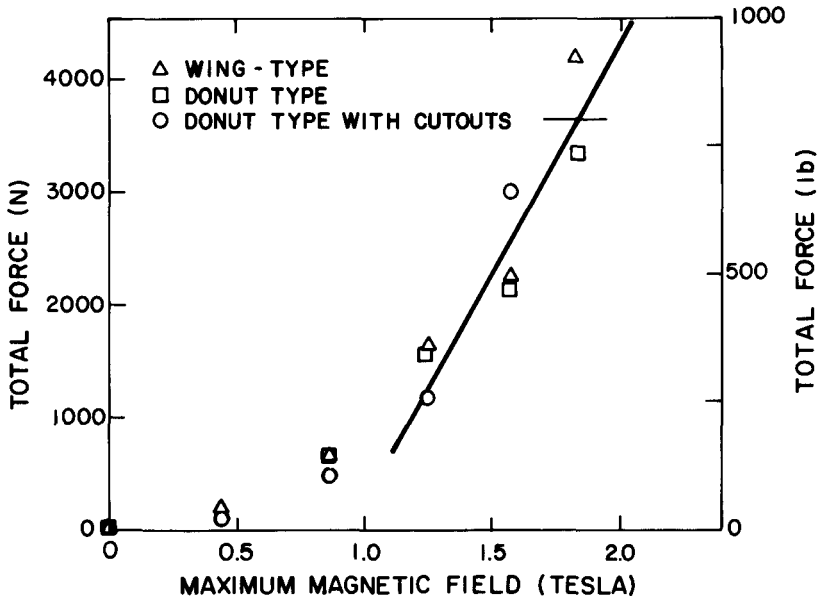

Figure 3-6. Measured force between 1700 cm^3 of soft iron shielding and magnet vs maximum magnetic field.

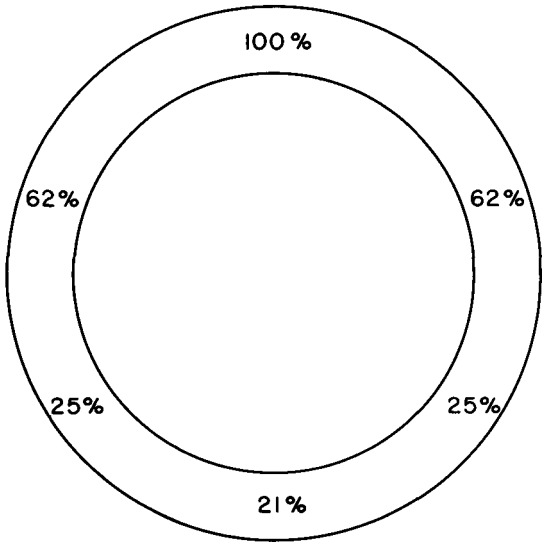

Figure 3-7. Magnetic field profile as a percentage of the maximum field. The profile was inferred from adiabatic temperature change measurements of the gadolinium.

Section 4

WHEEL AND WHEEL HOUSING

FLUID FLOW IN AN ACTUAL WHEEL

Some special design problems were encountered trying to force the fluid (water in our system) to flow (referring to Figure 2-5) from upper left to upper right, clockwise against the counterclockwise wheel rotation. It took a special arrangement to prevent fluid flow in the counterclockwise direction of wheel rotation, for instance in the "adiabatic section" from upper left to lower left.

Figures 4-1, 4-2, and 4-3 show the details of the wheel design. The rotating wheel has 18 fluid-tight compartments, each containing a porous gadolinium pressing. The wheel is surrounded by a housing containing many small, annular fluid chambers. The fluid enters a compartment in the wheel from a chamber in the housing through a wheel entrance slot. In each compartment, the fluid flows clockwise, through the porous gadolinium, exiting the compartment and entering the next clockwise compartment. The seals prevent the flow of fluid back to the adjacent counterclockwise compartment. Thus, if the velocity of fluid flow through each compartment is sufficiently rapid, the net fluid flow is clockwise as shown in the upper and lower thirds of the schematic wheel of Figure 2-5. Some of the mathematical differences between the continuous heat exchange shown in Figure 2-5 and the actual exchange are given in Appendix A of ref. 16.

ENTRAINED FLUID IN AN ACTUAL WHEEL

Although the compartmented wheel design provides flow in the clockwise direction, it does not, at first glance, entirely prevent flow in the counterclockwise direction. Some of the fluid introduced at the housing entrance ports (upper left and lower right in Figure 4-1) is entrained in the wheel and moves counterclockwise with it, through the adiabatic sections on the left and right of the wheel. The gadolinium in the wheel has about 40%

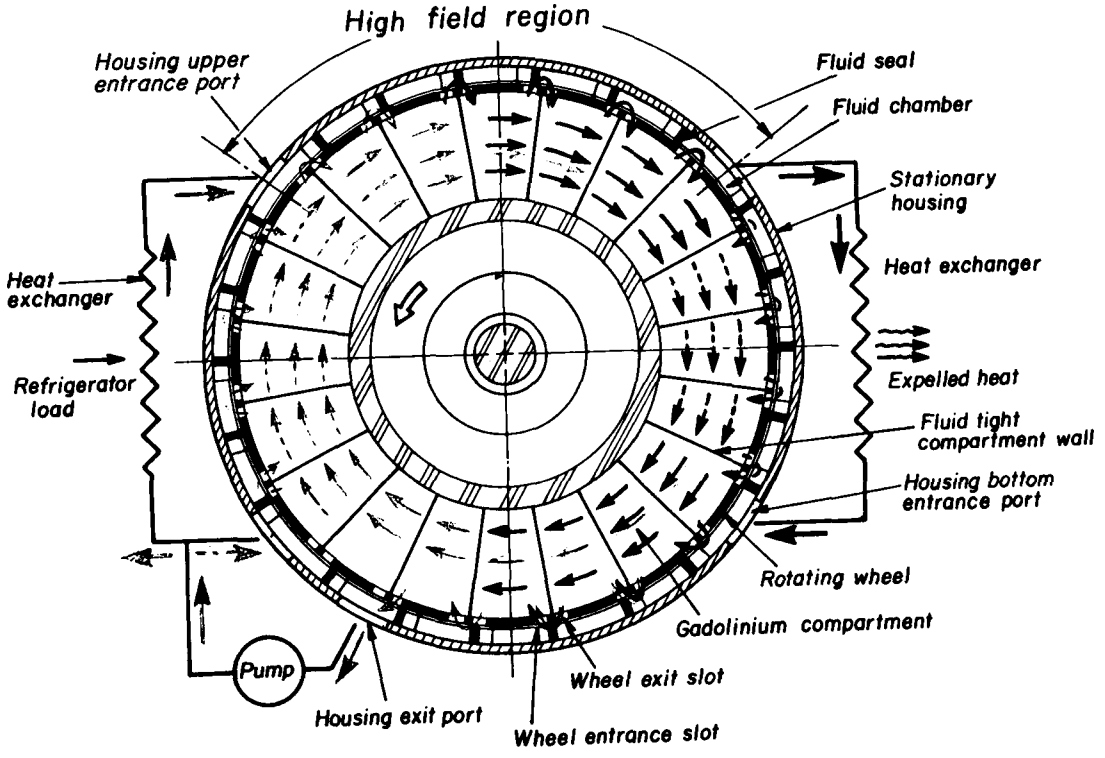

Figure 4-1. Details of the housing and wheel. Note that the actual wheel has 18 compartments not 20 as shown here. Figures 4-2 and 4-5 show the assembly from a different angles. The pump takes fluid from the lower left housing exit port and forces most of it through the left heat exchanger. Some of the fluid is forced to flow through the wheel to neutralize the flow of entrained fluid, as discussed in the text. The main flow, heated by the refrigeration load, enters the wheel housing at the upper left housing entrance port. It then flows through the wheel as shown in Figure 2-5. Flow continues to the housing upper exit port. Flow channels in each compartment (detail not shown) distribute the flow evenly through the porous gadolinium. Seals between each fluid chamber in the housing prevent backflow of fluid. The lower left housing exit and entrance near the pump are simplified in this figure.

void fraction and can entrain this amount of water. This thermal load on the magnetocaloric effect in the gadolinium reduces Δ, the temperature change in the adiabatic sections, by a factor of 2 (the water heat capacity equals the gadolinium heat capacity at a 32/68 volume ratio of H_2O/Gd). The entrained fluid problem is solved by allowing a small controlled volume of

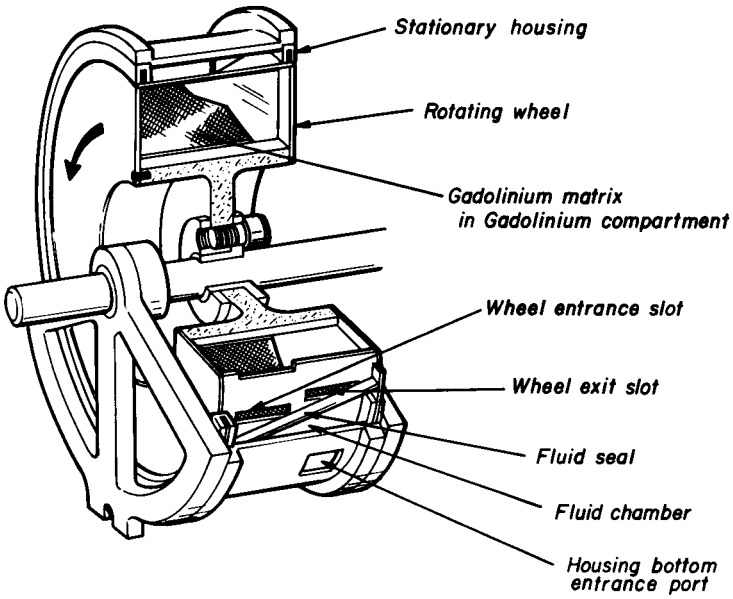

Figure 4-2. Cutaway of wheel and housing that we are constructing.

fluid to flow clockwise through the adiabatic sections of the wheel (where no flow is shown in Figure 2-5). This small flow equals the entrained fluid flow, so that there is no net flow (the water molecules in the left and right sections are not moving in the laboratory frame of reference, even though they are entrained in the porous gadolinium). Further details of this process are discussed in Appendix B. Appendix C of ref. 16 discusses the effect of leakage past the seals on refrigerator performance.

CONSTRUCTION OF THE WHEEL

The 18 compartments of the gadolinium shown in Figures 4-1, 4-2, and 4-3 are formed by 0.051- by 5.79- by 3.35-cm stainless steel compartment walls that are inserted into notches in the fiber glass hub and in the stainless steel rim (0.152 cm thick). The stainless-to-stainless joints are sealed with lead-tin solder and the stainless-to-fiberglass joints are sealed with epoxy. The two stainless steel side plates (0.152 cm thick) fasten to the fiber glass hub with silicone sealant (Silastic) and screws so that each compartment is sealed except for the oval wheel exit and entrance slots in the rim. These slots (2.22 by 0.32 cm) allow the heat exchange (water or alcohol) to flow into and out of each compartment. The gadolinium pieces, which are discussed in a later section, are inserted into each compartment before the side plates are attached.

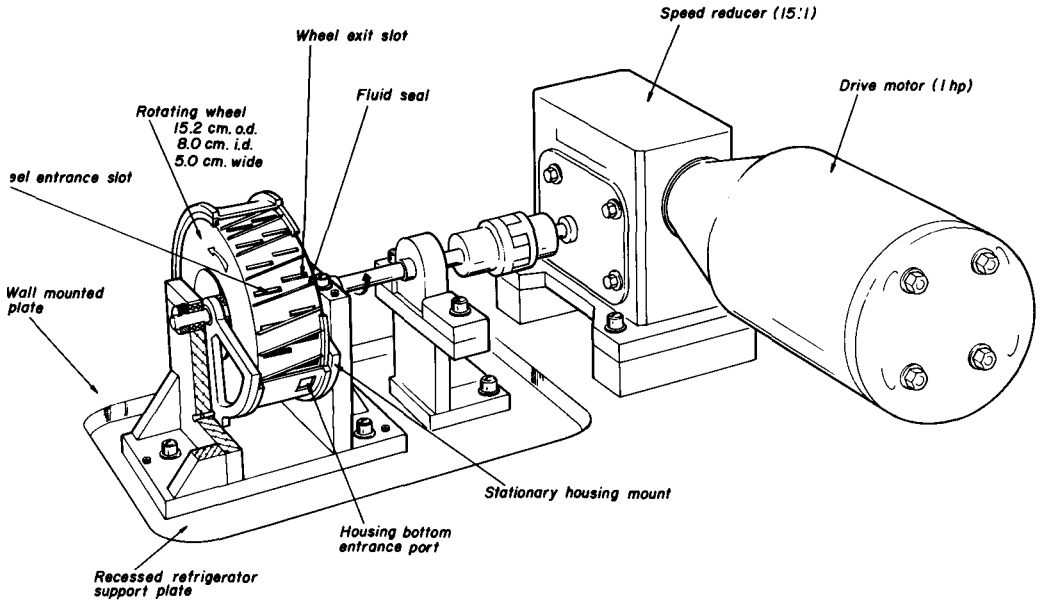

Figure 4-3. Cutaway of wheel and housing, along with the drive components. Note how seals prevent backflow of fluid.

CONSTRUCTION OF WHEEL HOUSING

The wheel housing is shown in Figures 4-1, 4-2, and 4-3. The primary problem faced here is the design of the seals, which direct the water flow into and out of the 18 gadolinium compartments. After numerous tests of different seal designs, we settled on the design of Figure 4-4.

The holders for the circumferential seals, which are on the edges of the rotating wheel, are stainless steel rings as shown in Figure 4-4a. The slots on the sides of the rings are openings for the axial-fluid seals, which connect the two circumferential seals. The holders for the axial-fluid seals, shown in Figure 4-4b, are made from beryllium-copper and bent to grip the seal material. The springiness of the holder's notched side opposes the pressure gradient existing across the seals.

The initial seal designs that were chosen are shown in Figure 4-4c. Initially, the circumferential seals were made from four materials selected to provide a range of hardness. The materials were Silastic 6508 (25-30 durometer), Neoprene $55A_2$ (55 durometer), Viton E70C

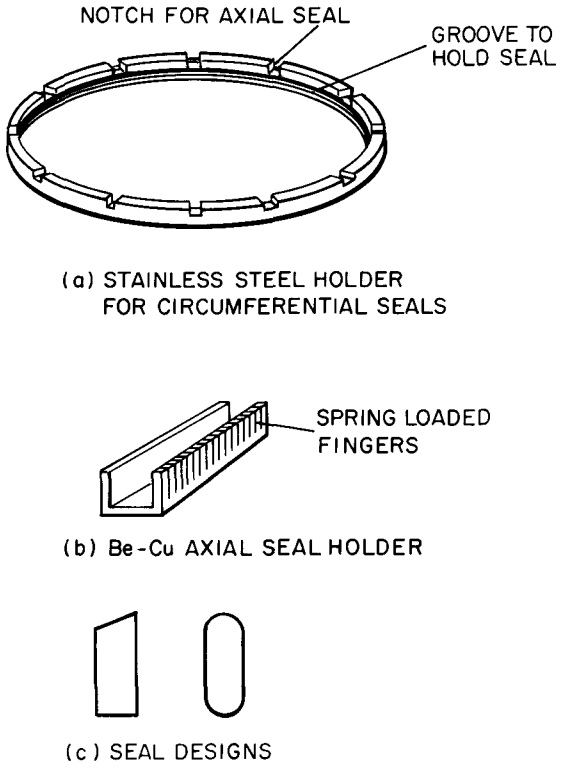

Figure 4-4. a. Stainless steel ring, which fits into the housing to hold the circumferential seals. b. The axial-fluid seal holder, which fits into the housing between the two rings as in 4a. The springs are to load the seal against the pressure differential. c. The cross sections of two seals chosen for being simple and reliable.

without carbon black (60-65 durometer), and Silastic 80 (80 durometer). Durometer is a relative measure of hardness for elastomers, with durometer 100 corresponding to infinite hardness.

To test the sealing ability and frictional torque of the various seals, an aluminum test wheel was made to be used inside the housing, which could be pressurized with water. The diameter of the aluminum wheel was reduced in small increments and tested at each diameter to determine frictional torque using a torque wrench, and sealing ability.

All of the rectangular seals had little or no leakage over the whole diameter range up to 2.76×10^5 Pa (40 psi) water pressure. Although some seals needed to be pressurized before they sealed, they retained their sealing ability. The oval design sealed very well with the larger wheel diameters but poorly with the smaller diameters. The torque was greater than desired but tolerable; 16.9 Nm (150 in. lbs) of torque corresponds to a loss of 106 W at 1 Hz. The diameter of the actual wheel was chosen to give $\sim$ 10 Nm of torque but an excellent seal because frictional losses are more easily corrected for than leakage losses.

WHEEL AND WHEEL HOUSING TESTS

The wheel, along with the drive shaft, bearings, etc. was assembled and tested. Because we found that the large internal water pressure tends to deform the outside radius of the wheel side plates enough to cause significant leakage, we added 2-mm-diam axial reinforcement rods on the inside of the outer diameter of the alternate gadolinium compartments. The unit was then essentially leakproof and was final tested in preparation for insertion of the porous gadolinium sections.

The stainless steel wheel housing, with its neoprene seals installed, was tested. The torque required to turn the wheel against the friction of the seals of the stationary wheel housing was about 3.5 N-m (30 in.-lb) with no water pressure in the housing. This amount was about 1.5 times larger or smaller depending on mechanical adjustments. The torque increased to about 5.8 N-m (50 in.-lb) with 275 kPa (40 psi) of water pressure in the housing. At a rotation rate of 0.5 rps, 5.8 N-m of frictional torque will result in $5.8 \times 2 \times 0.5 = 18$ W of frictional loss, which is an acceptable amount.

The fluid pressure drop around the entire wheel was measured with no gadolinium sections in the 18 compartments. Figure 4 of ref. 17 shows the orifice pressure drop ΔP_0 associated with flow into 18 orifices and out of 18 orifices. The predicted orifice pressure drop was only a few per cent higher than experimentally measured. This close agreement indicates that we have a good understanding of the external fluid dynamics of the wheel. This ΔP_0 is acceptable for flow rates under 200×10^{-6} m^3s (corresponding to a 0.5-Hz rotation rate). The 0.5-Hz rotation rate provides >1 kW of refrigeration capacity.

Section 5

POROUS GADOLINIUM FABRICATION AND TESTING

HEAT TRANSFER AND FLOW FRICTION IN FINE POROUS MEDIA

Pressure drop (ΔP) and heat transfer coefficients (h) for fluids flowing through porous media must be thoroughly understood for proper refrigerator design. Experimental correlations of ΔP and h in screens and pressings of spherical particles reported in Refs. 10 and 11 are based on the measurements of ΔP and h made in preparation for magnetic refrigerator development. The emphasis was to study through smaller particles and smaller Reynolds numbers than previously studied. The data of Ref. 11 confirms that the scaling laws deduced at high Reynolds numbers are approximately correct. Reference 11 averaged its previous results with its own data to obtain the following relation for flow through beds of spherical particles.

The pressure drop ΔP is given by

$$f = \frac{\Delta P \; d_p \alpha^3}{L G^2 (1-\alpha)} = 1.75 + (150/Re_p) \; , \qquad (5\text{-}1)$$

where d_p is the sphere diameter, α is the porosity (volume fraction of voids in the particle bed), L is the length of bed in the direction of fluid flow, ρ is the fluid density, G is the mass flow rate per unit frontal area, d_p is the particle diameter and μ is the fluid viscosity. Here the Reynolds number for calculation pressure drops is given by

$$Re_p = d_p G/[\mu(1 - \alpha)] \; . \qquad (5\text{-}2)$$

and the heat transfer coefficient is given by

$$\frac{h \; \alpha}{G \; C_p} = 0.21 \; Re_h^{-0.31} \; Pr^{-1} \qquad (5\text{-}3)$$

Pr is the Prandtl Number, $C_p \mu/\kappa$ where C_p is the fluid specific heat per unit mass, and κ is the fluid thermal conductivity. Re_h is the Reynolds

number for heat transfer and is equal to 2/3 Re_p. These equations, presented in dimensionless form, are valid in all consistent units.

Equation 5-1 is valid to within $\pm$ 30% over the wide range $0.1 < Re_p < 10^4$, however, it has not been tested over a wide range in α. Equation 5-3 may be in error by a factor of 3 for $Re_h \sim 1$ for $Re_h \sim 40$ Eq. 5-3 agrees with all the available data to within less than a factor of 2.

HEAT TRANSFER AND FLOW FUNCTION IN GADOLINIUM CHIPS

For the wheel refrigerator the porous gadolinium particles were prepared as fine chips by turning a gadolinium ingot on a lathe. For the pressure drop measurement they were pressed into 1.2 cm diam by 1.2 cm long cylinders and sintered together by annealing at 1000°C for 4 h. The gadolinium particles, when viewed microscopically, were in the form of jagged chips as shown in Figures 5-1a and 1-b. An equivalent particle diameter can be deduce from

$$d_p = \frac{6V_p}{A_p} \quad , \qquad (5\text{-}4)$$

where V_p and A_p are the average particle volume and surface area. In the calculation d_p the actual surface area is increased by a factor of 2for the microscopic surface roughnes. At the low flow velocities, which are of interest in magnetic refrigerator design, Eq. 5-1 becomes

$$\frac{\Delta P}{Lv} = \frac{150 \quad (1-\alpha)^2}{d_p^2 \alpha^3} \quad . \qquad (5\text{-}5)$$

Figure 5-2 is a composite of $\Delta P/Lv$ for all the waterflow measurements.

Pressure-drop measurements, using gases, gave values for $\Delta P/Lv$ about a factor of 50 lower than those for water flow through the same gadolinium pressing. This relationship is consistent because the gases used, helium and nitrogen at room temperature, have a factor 50 lower viscosity.

Uniform flow through all of the 1.2-cm-diam, 1.2-cm-long cylinders was confirmed visually first by forcing air through the cylinders under water and then by forcing water through the cylinders in air.

Figures 5-1a and -1b show the microstructure of samples with d_p = 236 μm and d_p = 68 μm shown in Fig. 5-2. The anomalously large impedance of the d_p = 236 μm sample may be associated with the more jagged microstructure. It was not possible to measure gadolinium heat transfer coefficients for several reasong. First, the heat transfer is so good that the Gd-water temperature is calculated to be too small to measure. Second, attempts to make electrical connections to the Gd for ohmic heating proved unsuccessful. Connecting temperature sensors to the Gd would have been equally difficult, however, a sensitive magnetic susceptometer was built which accurately measured the Gd temperature by the Gd susceptibility change.

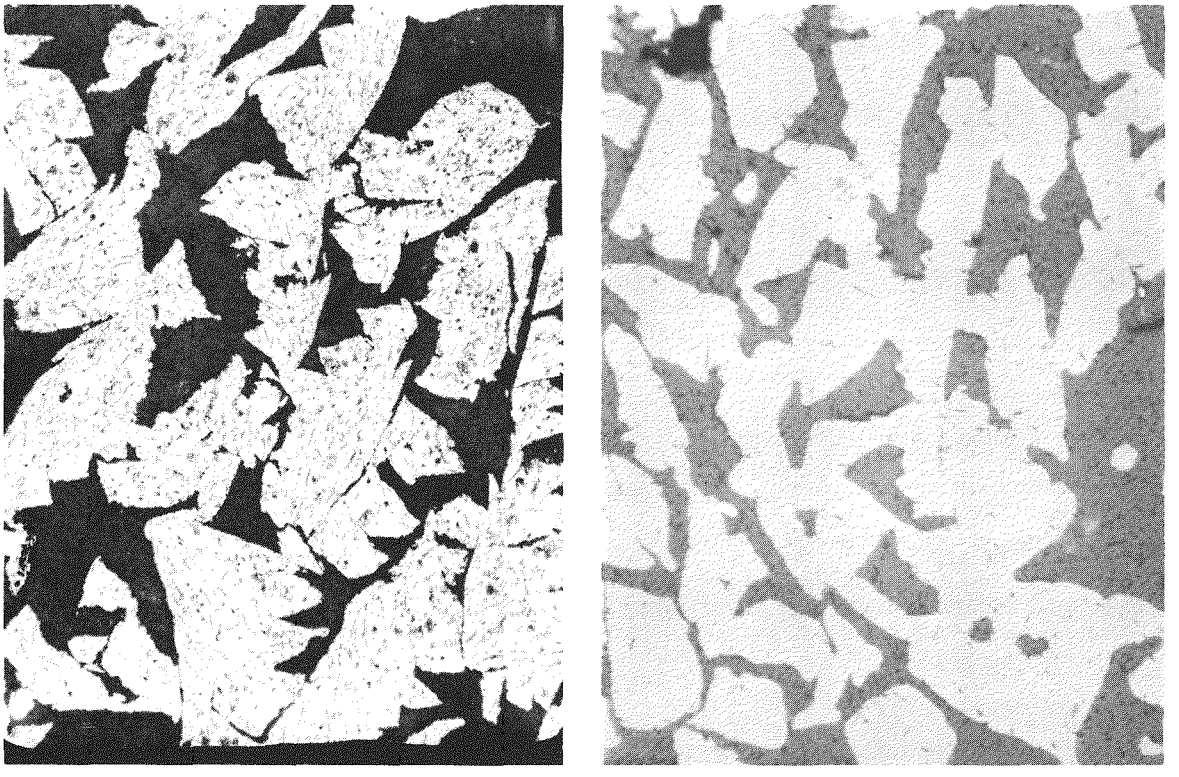

Figure 5-1. a. Microstructure of a d_p = 236 μm, porosity α = 0.41, pressing, 45 X magnification. b. Microstructure of the d_p = 68 μm, α = 0.40, 90 X magnification.

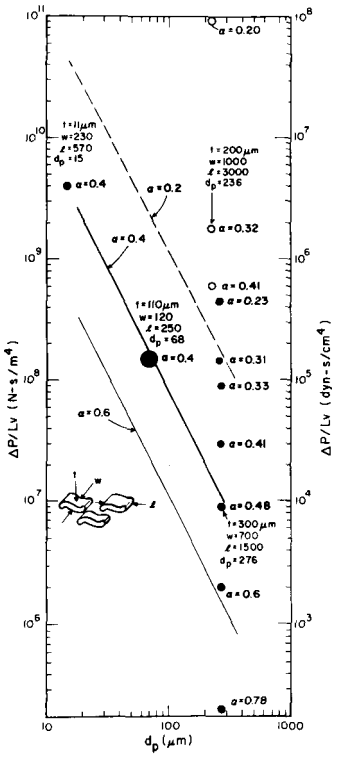

Figure 5-2. Low flow velocity pressure drops per unit length and unit velocity for water through porous gadolinium pressings as a function of equivalent particle diameter. Here α is the void fraction as determined from density meausrements. These values are for ν near 10^{-3} m/s; flow is viscous flow. The large deviation of the calculated lines from the data for small α is expected because the calculation is for equivalent uniformly sized spheres, which cannot be packed with $\alpha \leq 0.3$

DESIGN OF Gd SECTIONS

Five requirements must be met for the pressed gadolinium sections that fit into the gadolinium compartments shown in Fig. 4-1, 4-2, and 4-3. First, the pressure drop of water flowing through the porous gadolinium sections must not be too large or too small. Second, heat transfer must be very good, third, eddy-current heating must be minimal. Fourth, the thermal conduction across a section must not be too large. Fifth, fabrication must not be too difficult

or time consuming. Many different designs using many types of gadolinium powder were evaluated before a final design was obtained.

Pressure Drops in a Gadolinium Section. The flow of fluid through the porous gadolinium must be uniform to insure that the fluid (water) will have a homogeneous temperature. If not, when the water is mixed at the exit section there will be a net entropy production. The need for uniform flow requires that the pressure drop ΔP_G, associated with the viscous flow of water through the gadolinium, must dominate the orifice pressure drops of each section. The orifice pressure drop through each wheel exit of entrance slot is 1.9×10^4 Pa (1.9×10^5 dyn/cm^2) at a flow of 375×10^{-6} m^3/s. About the fastest rotation expected is 1 Hz, and at lower rotation rates ΔP_G will dominate because it drops off only linearly as v decreases, whereas the orifice pressure drop will decrease as v^2.

Figure 5-2 is the final summary of pressure drop measurements made with water flowing through gadolinium samples. From the data for the gadolinium pressing with equivalent sphere diameters d_p equal to 15 μm, 236 μm, and 276 μm, we decided that $d_p \sim 100$ μm would be a good particle size. Accordingly, new chips were prepared, which turned out to have $d_p = 68$ μm. A 60% dense pressing was tested, and the results appear in Fig. 5-2. However, we designed to use 65% dense gadolinium. Based on the results shown in Fig. 5-2, the essential shape of a gadolinium compartment is as shown in Fig. 5-3a. The area available for flow is 14 x 2.07 x 3.0 cm = 87 cm^2 (87×10^{-2} m^3). The flow must be through a distance L of 0.35 cm of porous gadolinium. We have

$$\Delta P_G = \left(\frac{\Delta P}{Lv}\right) = 3.8 \times 10^4 \text{ Pa } (3.8 \times 10^5 \text{ dyn/cm}) . \qquad (5\text{-}6)$$

which is consistent with our requirement that $\Delta P_G = 3.8 \times 10^4$ Pa. We have taken $\Delta P/Lv$ as 3×10^8 N-s/m^4 for 65% dense pressings of d_p = 68 μm particles, where v is the water velocity.

The pressure drop in the tapered slits must be small compared to this. If the maximum thickness of the tapered slits is 0.040 cm, then for the combined ΔP of the entrance and exit slits,

$$\Delta P = 2 \times 10^4 \text{ Pa } (2 \times 10^5 \text{ dyn/cm}^2) , \tag{5-7}$$

which is acceptable. (Viscous effects are calculated to be small compared to the kinetic effect used in the calculation of Eq. 5-7).

Heat Transfer. Using Ref. 10 we can calculate the heat transfer in the two counterflow heat exchanges of the gadolinium wheel.

$$Re_h = \frac{2(0.0068)(375/87)}{3(0.65)(0.01)} = 3 \tag{5-8}$$

and the heat-transfer coefficient

$$h = 1.1 \text{ W/cm}^2\text{-K}. \tag{5-9}$$

Each heat exchanger will have a volume equal to $\sim$ 1/3 of the wheel volume. If we neglect the comparatively small volume of the channels in the gadolinium pieces of Fig. 5-3, volume $V = 1/3 \times \pi/4 \times (14.86^2 - 8.83^2 \text{ cm}^2) \times 5.4$ cm = 202 cm^3. The heat exchange area A' is

$$A' = \frac{6V(1 - \alpha)}{d_p}$$

$$= \frac{6 \times 202 \ (0.65)}{0.0068}$$

$$= 1.2 \times 10^5 \text{ cm}^2. \tag{5-10}$$

The dimensionless heat exchange quantity where V is the exchanger volume, $N_{tu} = hA'/\dot{m}C_p = 1.1 \times 1.2 \times 10^5/(200 \times 4.18) = 160$. N_{tu} is the number of heat transfer units, and m is the mass flow rate. Reference 6 defines $E' = N_{tu} - 1$ and shows that a maximum value of 0.021 is required for good performance. Whereas the other design estimates appearing in this section are based on measured numbers, heat transfer measurements could not be made on the gadolinium, hence, this factor of 3 safety margin could be important.

Eddy-Current Losses. During $\sim$ 1/6 revolution, a compartment of the wheel moves from a region of vertical field B, basically parallel to the slit, into

a zero-field region. If this field decrease is assumed to occur uniformly in the vertical direction over a time 1/6 with $a = 1.7 \times 10^{-3}$ m (the half-width between slits of Fig. 5-3) the eddy-current power generation per unit volume is, from Eq. (C-10) of Ref. 12, $Q/V = 0.7 \times 10^3\ \nu^2\ W/m^3$. (We have used a 6-T field with a measured resistivity of $2.8 \times 10^{-4}\ \Omega$-cm).*

In addition, some component of the field will be perpendicular to the thin-plate laminates. Suppose we take the perpendicular component as 20% of 6 T. Now the quantity a in Eq. (C-10) of Ref. 12 is $\sim 1.04 \times 10^{-2}$ m (see Figure 5-3). The eddy-current heating from this field component is

$$\dot{Q}/V = 1000\ \nu^2\ W/m^3. \qquad (5\text{-}11)$$

We have a gadolinium volume of $606 \times 10^{-6}\ m^3$. This heating occurs during 1/6 of a revolution, both entering and leaving the high-field region; thus,

$$\dot{Q} = 0.3\ \nu^2\ W\ . \qquad (5\text{-}12)$$

Of course, this heating is negligible if $\nu = 2$ Hz even though we have taken the smallest of the measured ρ_e values.

Thermal Conduction Through a Section. A temperature gradient must be developed across the thin gadolinium plates (the subsections of gadolinium between slits) through which the water flows. The thermal conductivity of

---

*There is some uncertainty here. The electrical resistivity ρ_e of pure gadolinium is 127 Ω-cm (Ref. 13) or 140 $\mu\Omega$-cm (Ref. 14). We measured $\rho_e = 280\ \mu\Omega$-cm for a 2.1-cm-thick pressing of $d_p = 15\ \mu m$ filings after sintering at 1110°C for 1-1/2 h. For this material, $\alpha = 0.35$. For a 2.4-mm-thick pressing ($\alpha = 0.43$) of $d_p = 236\ \mu m$ turnings, $\rho_e = 710\ \mu\Omega$-cm. A section from a 1.2 by 1.2 cm pressing of $d_p = 68\ \mu m$ turnings, $\alpha = 0.4$, and $\rho_e = 1700\ \mu\Omega$-cm. (Turnings of this latter size, but from a new batch of gadolinium from the same supplier will be used in the actual wheel. Of course, ρ_e measurements on the actual wheel material will be made.)

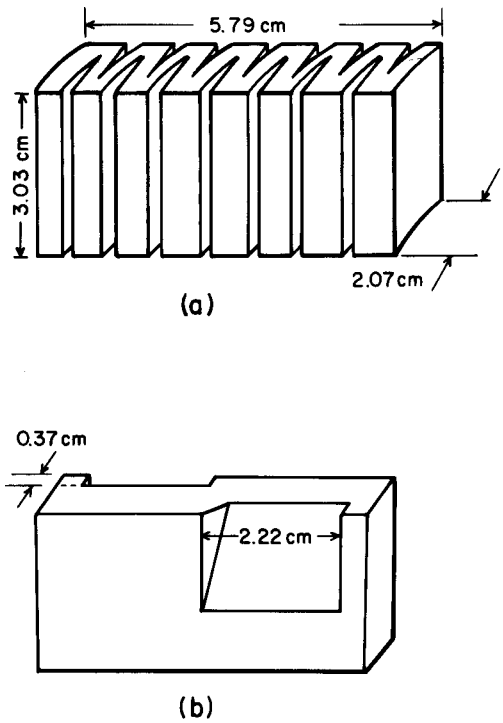

Figure 5-3. Porous gadolinium section to be placed inside a gadolinium compartment. a. Slits are shown. There are seven tapered slits on one side and six on the other. There is a tapered gap between the left and right outsides of the section and the compartment wall to allow flow at the edges. b. Openings run into the gadolinium sections under the entrance and exit ports to allow diffusion of the flow to and from all the slits (not shown). These openings are small tapered gaps between the part of the section and the compartment wall. They are 0.16 cm at the top and 0.0 cm at the bottom.

pure gadolinium metal* is κ = 0.096 W/cm-K. Our gadolinium has a smaller conductivity by the ratios of the measured electrical conductivity; thus, $\kappa = 0.096 \times 1.34 \times 10^{-4}/2.8 \times 10^{-4} = 0.046$ W/cm K. The area-to-length ratio in each compartment is 87 cm^2/0.35 cm = 250 cm. The thermal conductance from end to end through six compartments is $\dot{Q}/\Delta T = 0.043 \times 250/6 = 1.9$ W/K.

---

*The thermal conductivity of pure gadolinium is 0.104 W/cm-K (Ref. 14) and 0.083 W/cm-K. (Ref. 14) (The Lorenz number is a little high, 4.3×10^{-8} W-Ω/K^2 compared with the theoretical value of 2.5×10^{-8} W-Ω/K^2.)

One way of estimating the effect of this thermal short circuit from end to end of an exchanger is the method from Figures 2-36 of Ref. 15. The dimensionless conduction parameter(15) $\lambda = (\dot{Q}/\Delta T)\dot{m}C_p = 1.9/(200 \times 4.18) = 2.3 \times 10^{-3}$. For $N_{tu} = \sim 50$, this thermal conduction decreases N_{tu} by about 10%.

Another way of estimating the effect of the thermal short circuit is by the entropy production method of Ref. 16, Appendix C.

$$\frac{W}{W_C} = 1 + \frac{\dot{S}_p T_H}{\dot{S}_C (T_H - T_C)} , \qquad (5\text{-}13)$$

where W/W_c is the ratio of the required Carnot work, $\dot{S}_p$ is the net entropy production in the refrigerator, $\dot{S}_c$ = 22.8 J/K-s is the entropy removed from the cold load at temperature T_c, and T_H is the temperature at which the heat will be deposited. When an amount of heat Q leaks from a high temperature to a lower temperature across a temperature gradient ΔT,

$$\dot{S}_p = \frac{\dot{Q}\ \Delta T^2}{T} . \qquad (5\text{-}14)$$

In 12 sections (6 in each exchanger) with T = 40/6 K and Q = 1.9 x 40 = 76 W,

$$\dot{S}_p = 12 \times 76 \times (40/6)^2/294 = 0.15 \text{ W/K} \qquad (5\text{-}15)$$

and

$$\frac{W}{W_c} = 1.05 \qquad (5\text{-}16)$$

or a 5% effect on efficiency.

Fabrication Plans. Plans were for the gadolinium wheel to be prepared in an annular shape with an i.d. of 8.76 cm (3.4488 in.), an o.d. of 15.23 cm (5.996 in.), and thickness of 5.40 cm (2.127 in.). The wheel would be sintered at 1000°C for 4 h. It would be machined to the i.d. and o.d. of Fig. 5-3a sectioned into 18 pieces and shaped as shown in Fig. 5-3b. Slits would be stepped rather than smoothing tapered as in Fig. 5-3a.

ACTUAL FABRICATION OF GADOLINIUM SECTIONS

Here we describe the fabrication method for preparing the required 18 gadolinium sections from gadolinium ingots.* The chips were prepared by turning the 5-cm-diam ingots on a lathe using a 45^{0} tool. The feed was set at 0.019 cm/rev. (0.0075 in./rev.) and the cut was 0.013 cm (0.005 in.) deep. The surface speed was about 75 cm/s (30 in./s). A steady stream of helium gas was sprayed on the tool during the cutting to minimize heating and oxidation. The turnings were crushed and screened in an argon atmosphere to -35 +100 U.S.S. mesh. About 15% of the chips were not used because they were too fine. After crushing, the chips were pressed into a toroidal shape in a hardened steel die with unhardened steel punches. A steel cylinder in the center was used as a filler to provide a toroidal rather than a disk shape. Only modest pressure was needed to produce 61.4% of metal density in the pressing. In the die, the gadolinium pressing was 8.76 cm i.d., 15.23 cm o.d., and 5.78 cm thick. After removing the pressure and heat-treating the toroid, the dimensions expanded to 8.77, 15.26, and 5.82 cm, respectively. The wheel was placed in a graphite crucible, which served as a susceptor for rf heating coils. After surrounding the wheel with thin tantalum sheets, the too-fine gadolinium chips were strategically placed on the wheel to getter the vacuum. The chips also were placed on the tantalum surrounding the wheel and inside the covered graphite crucible-susceptor. The wheel then was heat treated in a vacuum induction furnace. During the heat treatment, the wheel changed from a dull gray to a shiny silver color, presumably as the oxide surface layer diffused throughout the interior of each chip or was reduced by the carbon. Annealing time was 4 h at 1000 C (measured with a thermocouple and optical pyrometer). It took 4 h to bring the wheel up to temperature (to avoid thermal shocks and temperature inhomogeneities) and 12 h for cooldown. The vacuum varied between 0.008 and 0.13 Pa (0.6×10^{-4} torr and 10^{-3} torr) as the gadolinium and prefired crucible outgassed.

We believe that any type of vacuum furnace would be suitable, although an induction furnace was most convenient in our case. However, we feel it is important to surround the gadolinium with some type of getter to prevent

---

*Obtained from Research Chemical Division, Nucor Corporation, P. O. Box 14588, Phoenix, AZ 85063.

the gadolinium itself from gettering the gases in the furnace. We found that the tantalum foil, which surrounded the gadolinium, was very badly discolored after the annealing, as were the gadolinium chips that were placed outside the tantalum foil. Note that the opening between the inside and outside tantalum getter was about 0.25 cm^2; this opening was required to allow evacuation of the space inside the tantalum where the wheel was located.

After heat treatment, the outside diameter, inside diameter, and thickness of the wheel were machined to fit inside the stainless steel wheel; a 0.004-cm clearance was allowed. Next, we planned to cut the wheel into 18 sections with a sltting saw to the shape as shown in the Figure 5-3. Unfortunately, machining of the soft porous gadolinium metal partially sealed the surface, thus preventing the necessary fluid flow. This problem was not encountered with earlier samples prepared from poorer quality metal with different heat treatments. We attempted to cut the metal after filling its pores with vinyl acetate and ice, but again the surface was partially sealed. Spark cutting the slots in the metal was slow and also tended to smear the surface of the metal. Because all these machining methods failed to give clear pores, we had to reduce the wheel to chips again.

The gadolinium chips were screened to obtain particles between 30 and 100 U.S.S. mesh. Then the chips were pressed into 15 disks, each 0.32 cm thick. Because radiographs indicated density variations, each disk was cut into trapezoidal-shaped pieces and sorted according to a correlation of measured density against measured pressure drop. This sorting enabled us to obtain the best possible homogeneity of gadolinium in each wheel segment.

After sorting the pieces into 18 piles, we epoxied the pieces together, using Eccobond 26, according to Fig. 5-3. The top and bottom of each segment (15 pieces) were sealed with the same epoxy. The epoxy was cured at $60^{o}C$ for $\sim$ 1 h before any excess epoxy was filed or sanded off. Each segment was shaped for a snug fit into a compartment. The final seals around each segment were made using Silastic on the side plates of the wheel. The wheel was inserted into the housing and the final assembly was completed.

TESTS OF Gd SECTIONS IN ASSEMBLED WHEEL AND HOUSING

The pressure drops in the wheel rotating at 0.1 Hz were measured as a function of water flow rate. With the valves to the external heat exchangers closed, flow was around the entire wheel.

Figure 5-4 shows the pressure-flow measurements. The solid line is the predicted pressure drop ΔP, which is the sum of the gadolinium and orifice

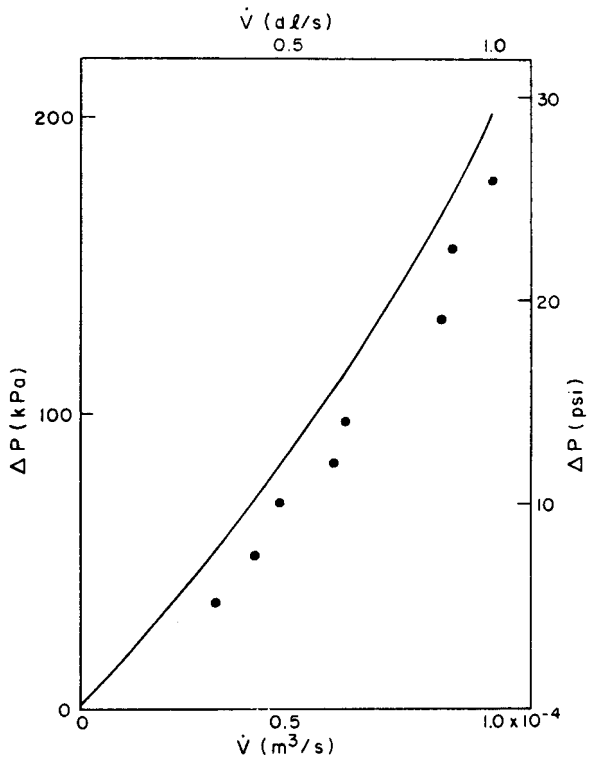

Figure 5-4. The pressure drop of flow into wheel entrance port 8 going all the way around the wheel, and out of exit port 7. (See Fig. 6-2).

pressure drops. In kilopascals, $\Delta P = 130\ \dot{V} + 69\ \dot{V}^2$, in pounds per square inch, $\Delta P = 19\ \dot{V} + 10\ \dot{V}^2$, where $\dot{V}$ is in decaliters per second. The experimental points that show this $\dot{V}$ dependence are slightly below the predicted curve. The deviation from the calculated curve does not seem serious as these results show that the gadolinium segments are close to design specifications.

Section 6

FLUID HANDLING AND INSTRUMENTATION

EXTERNAL HEAT EXCHANGERS

The use of a closed-cycle system to test the magnetic refrigerator requires the introduction of external heat into the low-temprature side of the refrigerator (refrigeration-load heat exchanger) and the removal of heat to the outside on the high-temperature side of the refrigerator (exit heat exchanger). (See Figure 2-5). Both heat exchangers were designed, constructed, and tested to satisfactory performance specifications, as separate components. The refrigertion-load heat exchanger consists of a LASL stock item; a 1-kW, 7-mm-diam, 1-m-long, magnesium-alloy-encased immersion heater, hermetically sealed with O-rings into a 20-mm-diam, 1-m-long, copper pipe. Standard soldered copper tee connections near each end permit continuous liquid flow through the assembly to exchange heat directly with the heater walls. Flow and temperature-increase measurements, at a flow rate of 2000 cm^3, verified electrical power-loss measurements.

The exit heat exchanger was made by pulling three copper tubes, each 7 mm in diam and wrapped spirally as an assembly with 2-mm-diam copper bus wires, through a 20-mm-diam stainless steel tube, 1 m in length. As seen in Figure 6-1, soldered copper tee transition pieces near the end force external liquid flow into thermal contact with the three copper tubes, which in turn exchange heat with internal liquid flowing in parallel through the inside of three copper tubes.

PUMPING SYSTEM

The Gearchem Model G6-ACT-KKT pump* was found to pulsate. By adding a particle filter and ballast tank to the output of the pumping system (Figure 6-2) we reduced the pressure pulsations delivered to the wheel to an

---

*Manufactured by Celesco Industries, Inc., Environmental and Industrial Products, 7800 Deering Ave., Canoga Park, CA 91304

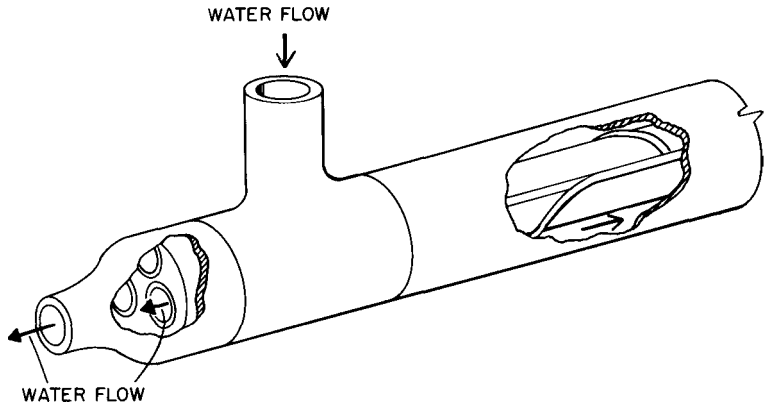

Figure 6-1. Exit heat exchanger construction.

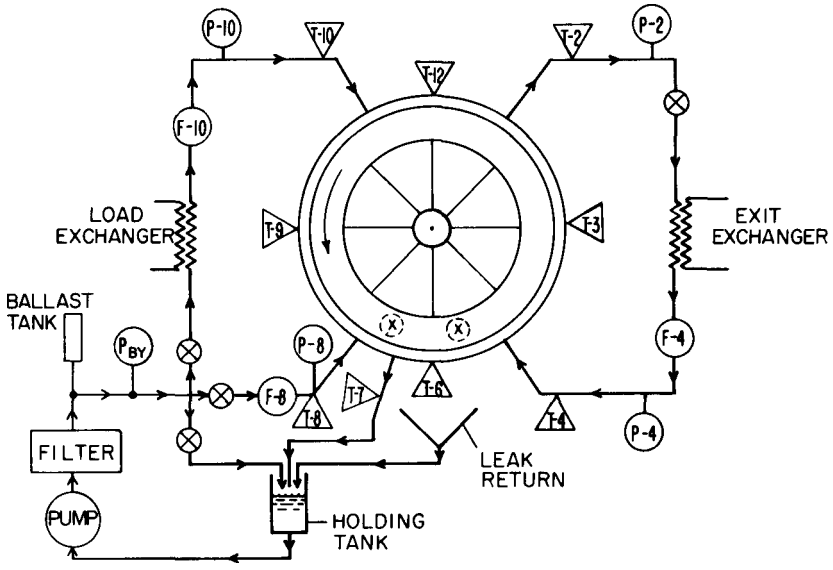

Figure 6-2. Schematic of closed-cycle pumping system used to evaluate refrigerator performance. F = flowmeter, P = pressure transducer, T = thermocouple, and x = susceptibility coils.

acceptable level. We also substituted a variable speed drive motor for the pump to eliminate the need to recirculate fluid in a bypass circuit, therby reducing pumping losses to a minimum.

To permit operator control and data taking standardizations, each element in the system was code numbered by point of entry in terms of an equivalent clockface time, as shown in Figure 6-2. Except for the temporary use of dial pressure gauges, the system was completed, tested with a rotating wheel, empty of gadolinium, and found to be acceptable.

FLOW MEASUREMENTS

Three sharp-edged orifice flowmeters were completed and assembled with a 140 cm^3/s at 10^5-Pa (15-psi) full-scale orifice plate in place. We attached rugged and reliable Celesco variable reluctance Model P7D differential pressure transducers to the flowmeter with small-diameter extension tubes. These units have a 2 ms response time. The three flowmeters were calibrated with timed volumetric measurements to yield a useful measurement range of 14 to 140 $\pm$ 0.5 cm^3/s.

TEMPERATURE MEASUREMENT

The most critical measurements needed to evaluate the magnetic refrigerator are those of temperature. A method was developed to place thermocouples in direct contact with the liquid-flow path using Swagelock gland fittings for hermetic seals. A copper-constantan thermocouple junction was soldered together on the inside tip of a 0.01-mm-thick, 1-mm-o.d., 5-cm-long, stainless steel tube. The 5-cm length of the tube was filled with low thermal-conductivity epoxy to stiffen the assembly against stress cracking. Fourteen thermocouple assemblies were made and tested in a stirred ice bath and stirred boiling-water bath to verify that they indicated the same temperature to within $\pm$ 0.2^{o}C while maintaining average readings systematically within 2% of published calibration tables. Their thermal time constant of response to changed water temperature was measured to be <1s. Two 4-channel OMNI-chart recorders with microvolt sensitivity were calibrated for simultaneously recording thermocouple voltages, as well as all other analog signals associated with magnetic refrigerator evaluation.

WHEEL DRIVE

The dc 1-hp variable speed motor was connected to its control box and the mechanical output was attached to the reducer gear box as shown in Figure 4-3. Tests of the complete assembly under load showed it performed adequately.

TORQUE MEASUREMENTS

The drive motor and gearbox were mounted on a carefully calibrated torque table (Figure 6-3). The load cell was used to measure the force, which was then translated to torque by a calibration using known weights on known lever arms. The output of the load-cell bridge was recorded on a chart recorder to provide a constant measure of the torque supplied to the wheel.

Because of slight irregularities in the wheel, the torque varied periodically with wheel rotation. Thus, the recorded torque measurement provided a record of the rotation rate. (Rotation rate also can be measured visually.) The torque and rotation rate measurements, when combined with the water pump power, provide a measurement of the power into the refrigerator, as required for an efficency calculation.

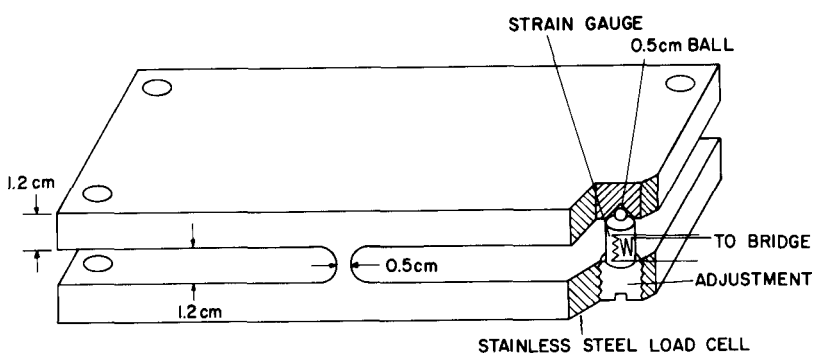

Figure 6-3. Torque table upon which the drive motor and gearbox are mounted. The torque on the gearbos drive shaft is translated into load cell force, which is measured by the bridge attached to the strain gauge. The two strain gauges on the load cell are located 180° around the circumference of the load cell. Only one gauge is shown here.

Section 7

TESTS OF REFRIGERATOR

INITIAL TESTS

The magnet was charged to 60 A (2.5 T) and the wheel was rotated at 0.1 Hz while the temperatures of the water flow around the wheel were monitored with thermocouples. The water flow rate was varied until the maximum temperature difference between the hot and cold sides of the wheel was achieved. The maximum ΔT was 7.5 to $8^{o}C$. The magnetic field was increased to 3 T with a slight increase in ΔT to $9^{o}C$. The water flow and wheel rotation rates were varied in many combinations, but ΔT did not increase above $9^{o}C$. Some observations from this experiment are:

(1) The ΔT between the hot and cold sides of the wheel remains the same for 0.1 and 0.2 Hz (with optimum flow).

(2) Flow oscillations appear with a frequency 18 times the rotation rate and with a magnitude of at least 15% of the average flow rate.

(3) The optimum average flow rate is nearly that calculated from Appendix A.

(4) The average flow rate adjustment is critical.

(5) ΔT increases with the magnetic field.

(6) The temperature at the top of the wheel, measured with thermocouple T-12, is extremely sensitive to flow fluctuations and flow balance. Temperature oscillations, described below, occur at this thermocouple site.

We decreased the stray magnetic field by a few percent by adding 1.2- by 7.6- by 11.4-cm soft iron sheets near the wheel. The ΔT increased $0.5^{o}C$, given optimum flow conditions at 0.1 Hz.

In addition to running the wheel as a refrigerator we also are able to run the wheel as a heat engine by running cold water through the hot-side heat exchanger while heating the cold-side exchanger. The torque in the heat-engine mode was at least 5.6 N-m (50 in.-lb) at 0.1 Hz, which gives a power of 4 W. Although this was not a large net-power output, the small ΔT

between the hot and cold baths makes the ideal Carnot efficiency extremely low, so the fact that it operates as a heat engine at all was significant.

ANALYSIS OF INITIAL REFRIGERATOR TESTS

It is important to thoroughly understand that results of these experiments which extended over about a one month period. The performance of the real system must be compared to the idealized system described in Sec. 2. Clearly the smaller than expected magnetic field plays a major role, as does the fact that the adiabatic sections of the wheel in Figure 2-5 have only a 1.2 T field difference across them. The theory of Section 2 shows that all the parameters of refrigerator performance are very sensitive to the field change through the quantity Δ which is proportional to the field change. But, is inadequate field change the main reason for the decreased capacity and temperature drop span? Lets examine the refrigerator in detail.

Internal Temperature Oscillations

One possible source of entropy creation is the temperature oscillations caused by the flow oscillations. We measured these temperature fluctuations at the top of the wheel in the high field and at the bottom of the wheel. Both temperature recordings had two frequencies, one of $1^{o}C$ magnitude peak-to-peak with a 1-cycle period, and one of $0.5^{o}C$ magnitude peak-to-peak with a 1/18-cycle period. The 1-cycle component is probably caused by impedence variation in the gadolinium around the wheel, whereas the 1/18-cycle component must be associated with the orifices of each compartment passing under the input/output seals to and from the pump. These temperature oscillations produce entropy in two ways: the gadolinium is always at a slightly different temperature from the water, and water with different temperatures is mixed in each housing compartment. The entropy created can be estimated using

$$dS = \frac{dQ\ T}{2T^2} \quad , \qquad (7\text{-}1)$$

where dS is the rate of irreversible entropy production and dQ is the heat flow between the two bodies initially ΔT apart with a mean temperature of T. This formula (derived in Appendix C of Ref. 18) is an excellent approximation for $\Delta T/T < 1$. When numbers appropriate for the wheel are used, the gadolinium-water heat transfer for two-thirds of the wheel gives

$dS = 0.005$ W/K. The water-water mixing gives $dS = 0.028$ W/K for 12 compartments. Neither of these mechanisms gives much irreversible entropy production because ΔT is so small.

Frictional Losses

A second obvious source of entropy production is the friction in the wheel. This friction is produced primarily by the seals rubbing against the wheel. The frictional torque averaged 17 N-m (150 in.-lb) at 0.2 Hz. The entropy production rate associated with this torque is (17 N-m) (2π) (0.2 Hz)/300 K = 0.071 W/K.

Parasitic Heat Leaks from Ambient Air

The pipes and hoses of the pumping system are exposed to air at ambient temperature. The heat leak in this system is another source of entropy creation. The heat leak can be calculated using $\dot{Q} = hA\Delta T$, where h is the conductance, calculated using the Dittus-Boelter equation for the water to the pipes and hoses. Similar experimental correlations for the air conductance to pipes or hoses can be found. The air conductance to the pipe is 1×10^{-4} W/cm^{2}K for a T of 1°C. The air-to-pipe impedance dominates the heat transfer from the air into the water, and the entropy production rate of this heat leak into our pumping system is 0.0004 W/K.

Water Flow Fluctuation

The flow measurements indicated a complex flow pattern with fluctuations of approximately $\pm$ 15%. The exact causes of these flow fluctuations are explained later. Appendixes A, D, and E of ref. 16 consider the effect of flow fluctuations, leakage, and inhomogeneity of gadolinium on the heat transfer in the top and bottom thirds of the wheel where the regenerative states of the cycle are executed. From Eq. (D-1) of ref. 18 the effect of slow, $\pm$ 10% fluctuations on the heat transfer number N_{tu} is predicted to vary inversely as the flow fluctuation percentage, if the initial heat transfer is excellent (N_{tu} large). We designed for a $N_{tu} \sim 60$ with a safety factor of 3, so the N_{tu} should have been the order of 180 initially, and reduced to the order of 19 by the flow fluctuations.

Appendix A, ref. 16, shows that 20% leakage around the segments would lower the N_{tu} from 60 to 22. At the moment, the refrigerator performs as if our effective N_{tu} were about 4, which would requier $\sim$ 60% leakage. All of our

earlier leakage measurements put the leak rate at ∿10%, which should have negligible effect on the N_{tu}.

Appendix E, ref. 16 considers flow inhomogeneity caused by variation in gadolinium porosity. Equation (E-12), ref. 16 shows that the 10% inhomogeneity in the gadolinium segments should have a small effect if the initial N_{tu} is large.

Pump Losses and Pressure Drop Through the Wheel

We also consider losses associated with the pump and the water circulation. The water-pump motor is rated at 250 W (1/3 hp), where the maximum loss from the pump and pressure drops around the wheel are 250 W. The maximum pressure-drop loss around the wheel VdP is 50 W. However, to produce this flow loss, the pump motor has to be at maximum power. The discrepancy between 50 and 250 W suggests that the pump is extremely inefficient. The performance of the pump is described later in more detail.

First- and Second-Law Analysis of Refrigeration

We will do an energy and entropy balance on the unit. Table I records the energies and entropies illustrated in Figure 7-1. Pumping and parasitic heat leaks enter the system as a refrigeration load at 293 K. Frictional heat and entropy are dissipated at a mean temperature of 296 K. Mixing entropies are also produced at a mean temperature of 296 K (N.B., energy is not introduced into the wheel in this entropy-producing mechanism). The effect of N_{tu} degradation is not fully understood but it should be very small, according to previous discussion. The work put into the magnetic system has no entropy content until the internal refrigeration process converts the work into entropy. The amount of expelled heat equals the energy going in, and it may be converted to an expelled entropy by dividing by 301 K.

The losses shown in Table I, excluding N_{tu}-degradation, give a total irreversible entropy-handling rate of 0.4 to 1.0 W/K. Our analysis of the N_{tu} degradation indicates that if the original N_{tu} were large (∿60), the effective N_{tu} in the presence of various imperfections should still be large, so very little entropy will be created.

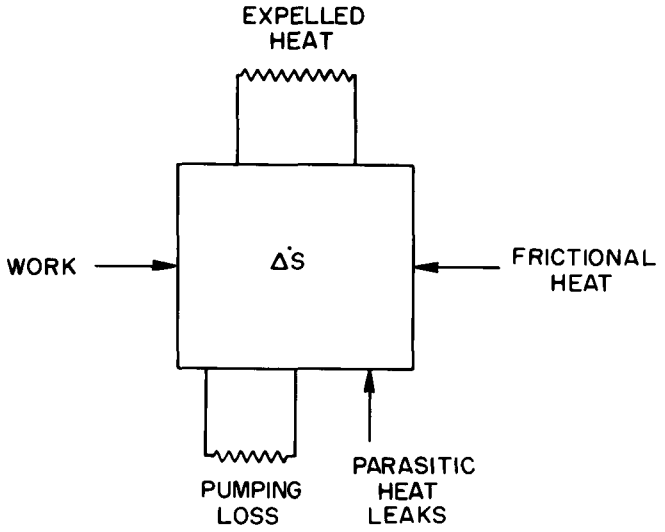

Figure 7-1. A black-box refrigerator used for energy and entropy balance calculations.

TABLE 7-1
ENERGY AND ENTROPY SOURCES IN REFRIGERATION

Source	Energy (W)	Temperature (K)	Entropy (W/K)
Pumping loss	50 to 250	293	0.171 to 0.853
Parasitic heat leaks	0.1	293	0.0004
Frictional heat	21	296	0.07
Water-water mixing	0	296	0.03
Gd-water mixing	0	296	0.005
N_{tu} degradation	0	296	?
Work	39	—	0
Sum of expelled heat or sum of entropy produced	110.1 to 310.1		0.276 to 0.958
Expected expelled entropy deduced from expelled heat		301	0.366 to 1.03
Unaccounted entropy			0.090 to 0.072

Ideal Refrigeration

From the entropy temperture curves for gadolinium near room temperature, the entropy change for a 3- to 0.5-T magnetization or demagnetization is 0.62 J/mole K. Hence the entropy-change rate for refrigeration at 293 K and 0.2 Hz is

$$\Delta\dot{S} = (0.62 \text{ J/mole K})(14.6 \text{ moles})(0.2 \text{ Hz}) = 1.81 \text{ W/K}. \qquad (7\text{-}2)$$

However, a careful estimate of the magnetic field profile indicates that ΔS shold be reduced to 0.35 J/mole K for the adiabatic sections of the wheel.

Therefore, the real entropy change rate for refrigeration at 293 K and 0.2 Hz is $\Delta\dot{S}$ = 1.01 W/K. This is very close to the second set of values in Table I.

ADDITIONAL REFRIGERATOR TESTS

Additional Magnet Test Results

In the first magnet tests our power supplies were limited to 150 A. Later, Intermagnetics General Corporation (IGC) power supplies capable of 300 A were used. With these power supplies we tested the inner superconducting magnet coil up to 300 A with no current in the outer coil and obtained a field of 3.55 T at the center of the recess in the Dewar (where the center of the gadolinium wheel passes at its apex). The field at the corners of the racetrack-shaped magnet is 1.4 times the field at the center of the magnet, which means that the inner coil wire is operating at 76% of its short-sample limit in this mode. A further test of the inner wire with three power supplies in parallel gave a field of 3.9 $\pm$ 0.1 T with 335 $\pm$ 5 A in the inner coil alone, indicating that the inner wire reached 85 $\pm$ 1% of its short-sample limit. On the other hand, tests of the outer windings by themselves provide a field of 3.1 T at the center, or about 3.1 x 1.4 = 4.3 T at the corners. This represents 77% of the short-sample limit.

With the inner coil at 300 A from the IGC supplies, the current was increased in both coils by another power supply across both coils. The maximum current befoe quenching was $\sim$ 10A in the outer coil and 310 A in the inner coil. This produced a field of 3.7 T at the center of the recess in the Dewar. A plot of inner-coil quench current vs outer-coil quench current showed approximately a straight line, indicating that no obvious optimum combination

of inner and outer current exists. The problem with the magnet performance is that when inner and outer winding coils are operated together, it is not possible to achieve a field larger than that of the inner coil operated by itself; this suggests a field-related instability of some kind. Possibly the magnet problem is that the yoke shown in Figure 3-2 contains only part of the coil; no yoke contains the forces along the length of the coil.

Magnetocaloric Effect in Gadolinium

Because refrigerator performance is a strong function of the gadolinium entropy-temperature relations (see Section 2), we measured the entropy-temperature curves for gadolinium in fields up to 3 T. The experiment consisted of embedding a copper-Constantan thermocouple in a small gadolinium sample, insulating the sample, and measuring the temperature change as the sample was quickly inserted into or removed from the field. The zero-field heat capacity of gadolinium was measured recently for several samples.[19] We integrated the data from sample Gd 2A of Ref. 19 to obtain a zero-field entropy curve. The results are plotted in Figure 7-2.

Agreement between the experimental results and the calculated curves , Fig. 2-2, is excellent and verifies that the magnetocaloric effect in gadolinium is very large for high field changes.

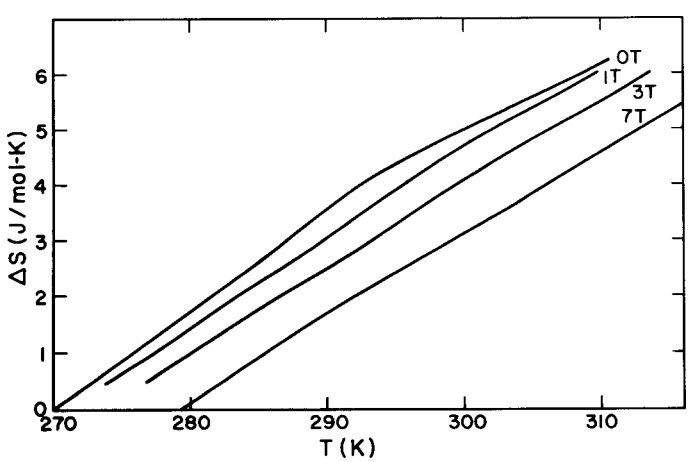

Figure 7-2. Measured entropy-temperature curves for gadolinium metal as a function of magnetic field. The 7-T curve was taken from calculated curves, which agreed with the experimental results of G. V. Brown.

We also measured the adiabatic temperature change on a sample of porous gadolinium after it had been through the entire fabrication process. The sample gave results identical to those for the virgin sample of gadolinium as received from Research Chemicals.

Another experiment was done to test for hysteretic heating. We rapidly cycled the gadolinium sample in and out of the field for as many as 10 cycles and found no evidence of any hysteretic loss. The magnetocaloric effect in gadolinium was as originally expected.

Gearchem Fluid-Pump Loss

Because of the pump location in our flow circuit (see Figure 6-2), any inefficiency in the pump can produce a heat load on the refrigerator. The pump was driven by a 1/3-hp (250-W) motor, which produced a maximum flow of 120 cm^3/s (1.20×10^{-4} m^3/s) at 60 psi (4.1×10^5 Pa), corresponding to a flow loss of 50 W. The 200-W difference between the power required for the motor and the flow loss could be a thermal load on the refrigerator. To check that possibility we attached copper-Constantan thermocouples to the copper pipes coming into and out of the pump. By measuring the flow rate and the temperatue difference we obtained the power dissipation of the pump as a function of pressure drop across the pump. These results are shown in Fig. 7-3. The heating is relatively independent of the volume flow rate V.

The pump was "flat out" for the maximum flow and therefore dissipating 250 W. The maximum experimental flow loss was 46 W, so the amount of power dissipated in the pump and water was 204 W. From the data in Figure 7-3, the maximum thermal load dumped into the water was $\sim$ 160 W, which means that $\sim$ 45 W were dissipated in the pump body and shaft.

To eliminate the pump load we soldered a coil of small copper tubing around the pipe between the outlet of the pump and the filter and attached a thermocouple before and after the tubing. By adjusting the flow of cooling water through the tubing we could cancel the load associated with the pump inefficency. However, when the refrigerator was operated at optimum conditions the removal of the pump load decreased the temperature gradient across the hot heat exchanger but did not noticeably increase the temperature span across the wheel. The situation is somewhat puzzling but suggests that internal losses dominate the performance of the wheel.

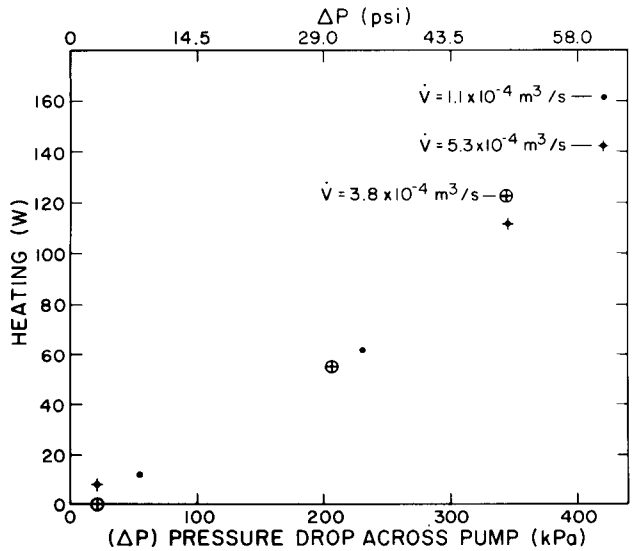

Figure 7-3. Heating load of the Gearchem pump as a function of the pressure drop across the pump for a range of volume flow rates.

Flow Pattern Measurement and Seal Modification

Four differential pressure transducers obtained from Celesco enabled us to make rapid response-time measurements of the flow and pressure. A section of the flow and pressure recording at very low rotation rate is shown in Figure 7-4. The nomenclature and positions of the transducers and valves are shown in Figure 6-2.

The flow pattern at F8 (Figure 7-4) fluctuated 18 times per cycle, which means that it was associated with the 18 compartments of the wheel passing over the entrance and exit ports to and from the pump. Because the pressure at P8 also decreased as the flow through F8 increased, the impedance from inlet to outlet sharply decreased at that point. The flow through F4 decreased simultaneously with the increase in F8, as was to be expected if the impedance decrease was caused by a leak from inlet to outlet.

The smaller, slow fluctuations of the baseline of the flow patterns are caused by impedance variations as the orifices in various compartments are partially blocked when passing under the axial seals in the housing. The rapid fluctuations that cause the wide trace most apparent in F10 are caused by the pump. The changes in the average baseline flow, most apparent in F4, are caused by the variation in the flow impedance of the compartments. Because

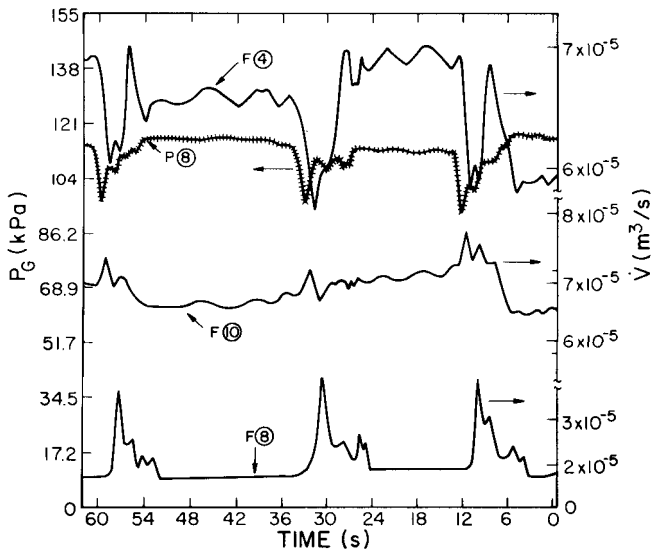

Figure 7-4. A recording illustrating the flow patterns and pressure pattern at very slow rotation rate.
the flow through F4 is in parallel with flow through the high-temperature adiabatic section of the wheel when high-impedance compartments are in the adiabatic section of the cycle, the flow through F4 will increase.

additional shimming of the neoprene seals did not reduce the flow fluctuations. We then sequentially put the flow input into each port of the housing and measured the output from all of the other ports. The output measurements agreed with our design expectations but proved the existence of a flow short circuit from port 7 to port 8 at one particular spot for each compartment. The width of the flow increase in the pattern of Figure 7-4 also corresponds to two orifice widths. The seals around these ports were widened to decrease the leakage. In the final version, the magnitude of the leakage in the flow fluctuation was almost as large as it was initially, but the duration was much shorter. In the present design the only obvious way to stop the flow fluctuation completely would be to exactly balance the leak with a complete flow blockage. The inlet-outlet seal was not fine-tuned to that extent because of the inherent flow fluctuations caused by the gadolinium porosity variation. Also, the calculations reported in Ref. 18 indicated that the 10% fluctuations caused by the seals were rapid enough to average out and had little effect on the heat transfer. However, the effect of the

fluctuations on the entrained fluid compensation is uncertain and the models used in Ref. 18 to predict the effects of fluctuations on heat transfer may be too idealized.

Entrained Fluid

Another possible explanation of the reduction in cooling power and limitation to a $9^{o}C$ span is that the entrained fluid in the gadolinium acts as an internal load because it is not being properly compensated by a controlled flow in the opposite direction. There is little doubt that in steady state the counterflow mechanism will work, but with flow fluctuations it may not. If the entrained fluid is not compensated for, the available cooling power will be dramatically reduced. The temperature change in the adiabatic section of the cycle with no compensation for the entrained fluid is decreased as the ratio of the thermal mass of the gadolinium to the thermal mass of gadolinium + thermal mass of water + thermal mass of stainless steel. If we assume that 20% of the wheel is in the adiabatic section and that the field gradient across this section is 1.4 T, then a ΔT of $1.2^{o}C$ is predicted with no compensation. The experiment that corresponds with this calculation involves closing port 8 and putting all the flow for optimum operation into port 10. The experimental average temperature difference between T10 and T9 is $0.5^{o}C$. Since this measures approximately half of the ΔT across the adiabatic section, $1.0^{o}C$ should be compared to the calculated number, $1.2^{o}C$. To check, we ran the wheel with alcohol as the heat exchange fluid. Because the density of the alcohol is 79% that of water and its specific heat is 58% that of water, the predicted temperature change in the adiabatic section with the same assumptions as before is $2.0^{o}C$. The measured average temperature difference between T10 and T9 for the alochol was $1.5^{o}C$, which, when doubled, gives $3.0^{o}C$ for the full adiabatic section. The discrepancy between 2 and $3^{o}C$ may be caused by different heat transfers in the regenerative section of the wheel when alcohol is used.

When the reverse experiment was done--part 10 closed and all of the fluid put back into port 8--the corresponding temperatures were T8 - T9 = $+1.75^{o}C$ for water and T8 - T9 = $2.75^{o}C$ for alcohol. The fact that T9 is colder than T8 is expected because the refrigeration load is being extracted from the fluid as it moves through the adiabatic section. Even though the temperature change is in the opposite direction, the magnitude of the temperature difference is

bigger than in the previous case. Therefore, the counterflow mechanism is partially successful in compensating for the entrained fluid.

The maximum amount of external cooling from the wheel with no compensation for the entrained fluid can be calculated from the first experiment. If all the fluid required for balanced thermal mass flow goes through the external heat exchanger and there is a 1.0°C difference across the adiabatic section in the presence of the entrained water, we obtain 474 W of refrigeration at 0.2 Hz.

Temperature Measurement in the Gadolinium

Because of the uncertainty of the temperature gradient between the water and the gadolinium in the wheel we decided to measure the gadolinium temperature directly. When a thermocouple was used, the changing flux induced a voltage in the thermocouple wire loop that was of the same order of magnitude (tens of microvolts) as the thermal voltage. Therefore, we mounted a small, disk-shaped thermistor (0.10 cm thick x 0.23-cm dim) in the center of the gadolinium in one compartment. Connections to the thermistor were brought from the wheel through a double commutator that was fabricated from printed circuit board and gold-plated, beryllium-copper contacts. A calibration of the thermistor gave good sensitivity to temperature changes, with 0.35-s response time in water and 4-s response time in air. The mgnetic-field dependence was negligible.

The first experiment was the measurement of the gadolinium temperature as a function of field and compartment position with no water in the wheel. The adiabatic temperature change was obtained dynamically while the wheel continuously rotated at very low frequencies (0.05 Hz) and statically with the wheel stopped. The measurements agreed and gave a ΔT of 4.75°C when the wheel was in a 3.5-T field. The shape of the dynamic temperature change was approximately sinusoidal and gave a measure of the magnetic field profile inside the gadolinium. The only thermal load on the gadolinium is that from the stainless steel and fiber glass, which reduces the adiabatic temperature change by 32%. Therefore, without any load, the gadolinium would have an adiabatic temperature change of 7.0°C in 3.5 T, compared with the 7.4°C change shown in the experimental entropy-temperature curves of Figure 7-2.

The magnetic field profile shown in Figure 3-7 was inferred from these measurements and indicates a major limitation of the present wheel design. The important field change is across the adiabatic section, from the 8- to 10-o'clock and 2-to-4-o'clock positions in Figure 3-7, and is only 37% of the maximum field produced by the magnet. The gadolinium homogenizes the field within itself, a fact that explains why the presence of the soft iron shielding around the bottom part of the wheel gave such small increase in the temperature across the wheel.

In the next experiment we added water and observed the temperature change in the gadolinium as the refrigerator operated. When ports 10 and 2 were closed and all the fluid required for approximately balanced flow was going into port 8, we obtained the temperature pattern shown in Figure 7-5A--a uniform temperature excursion with a maximum excursion of 6.8^{o}C at 0.044 Hz. The phase of the temperature profile is difficult to interpret because of the time constant of the thermistor, but the shape should be meaningful. When ports 2 and 11 were partially open and port 8 was open (as required for proper operation of the refrigerator), the temperature profile changed to that shown in Fig. 7-5B, where the profile indicates that the gadolinium is undergoing an Ericsson-type cycle instead of a Brayton-type cycle, i.e., it has two roughly isothermal steps instead of adiabatic steps where the temperature rapidly changes. The only explanation is that the gadolinium has a thermal load during magnetization and demagnetization. That explanation supports our earlier observation that the entrained fluid in the wheel is not being completely compensated for by the fluctuating counterflowing fluid.

Pressure Drop Across the Gadolinium

At the start of our experiments on the wheel we measured the pressure drop across the wheel (see Figure 5-4). It agreed (within a few per cent) with the expected calculated pressure drop. After each day of experiments with the wheel we flushed the 1% NaH_2PO_4 solution out of the wheel with alcohol and dried the wheel with dry nitrogen gas. Each time the wheel was taken apart we inspected the gadolinium and found no apparent degradation. However, after 3 months of operation the pressure drop across the wheel had increased by at least a factor of 2.

We lowered the impedance somewhat by back-flushing with high-pressure nitrogen, but did not reach the original value. Ultrasonic cleaning in

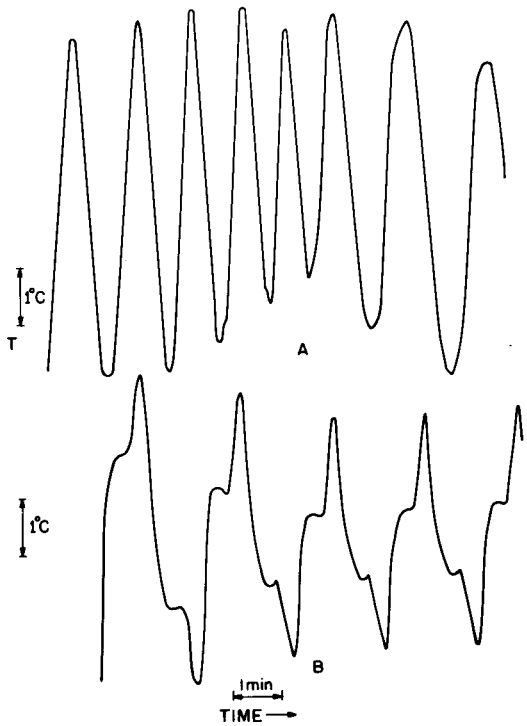

Figure 7-5. (A) Temperature profile of the gadolinium with balanced flow and with V2 and V11 closed, V8 open. (B) Temperature profile of the gadolinium with balanced flow and V2, V11 partially open, V8 open.

alcohol produced no change in the impedance. The flow-impedance increase is not a serious problem because it only gives a larger flow loss in the wheel; however, its cause is not completely understood and probably should be studied more carefully.

Heat Transfer Results for the Wheel

Another possible explanation of the limited temperature difference across the wheel is that the heat transfer is much worse than expected. To check this possibility we operated the wheel in a zero magnetic field with a temperature

gradient produced by using hot and cold water. From a measurement of the temperatures around the wheel and by using the relationship

$$\Delta T_{av} = 2[T_H - T_C)/(1 + N_{tu})] \qquad (7\text{-}3)$$

where ΔT_{av} is the average temperature difference between the gadolinium and the water, $T_H - T_C$ is the temperature difference across the wheel, and N_{tu} is the number of heat transfer units,(15) we were able to infer an N_{tu} of 5, a value well below our design value of 60.

These measurements were taken with the higher gadolinium flow impedance, which may have influenced the result. A more plausible explanation is that the combination of the flow fluctuations and thermal mass imbalance caused by the variation of the field in the heat exchange sections of the wheel probably caused the lower N_{tu}. The exact nature of the heat-exchange degradation is difficult to model. The separate causes, which were treated in the Appendices of Ref. 18, indicate that if the original N_{tu} is large, the degradation from flow fluctuations, etc., shoud be small. A good experiment would be to measure separately the heat transfer of one of the gadolinium segments. If hA (where h is conductance, A is contact area) is large, the transients of the situation must be seriously limiting the N_{tu}.

FINAL ANALYSIS

In light of the additional experiments, further analysis was possible.

Comparison of the Actual Wheel with Theory to Estimate N_{tu}

We can use the calculations of Ref. 7 to compare the expected temperature span with out measured 9^oC span. With zero load, the temperature of the cold fluid T_f^C divided by the temperature of the hot fluid T_f^H is 289/298 = 0.970. Under zero load, the temperature of the water change in the external cold heat exchanger, Δ_f^C, is zero. Figure 2-10 shows that under these conditions we expect $T_f^H/(\Delta_W N_{tu} = 16)$ which gives $N_{tu} = 5.8$. (We took the adiabatic temperature change of the gadolinium Δ_W as 3.2^oC.) This value of N_{tu} is consistent with the N_{tu} deduced from Eq. (7-3). However, the refrigerator capacity of 500 W at a 7 K span is larger than expected on the basis of $\Delta_W = 3.2$ and $N_{tu} = 5.8$.

External Load Curve for Gadolinium Wheel

The most important parameter of the refrigerator is the amount of cooling power that it can maintain over a given temperature span. We collected these data in the form of a load curve at 0.2 Hz for a ΔB of $\sim$1.2 T across the adiabatic section of the wheel. The data are shown in Figure 7-6. The load curve is impressive for the size of the magnetic field change across the adiabatic section of the wheel and should scale along both axes almost linearly with an increase in ΔB.

Efficiency

Another important characteristic of the refrigerator is the efficiency. For this refrigerator we can take the ratio of real to ideal coefficient of performance (COP) as the efficiency. The ideal COP is given by the ratio of the cooling power to work or

$$\text{COP (ideal)} = T_C/T_H - T_C), \qquad (7\text{-}4)$$

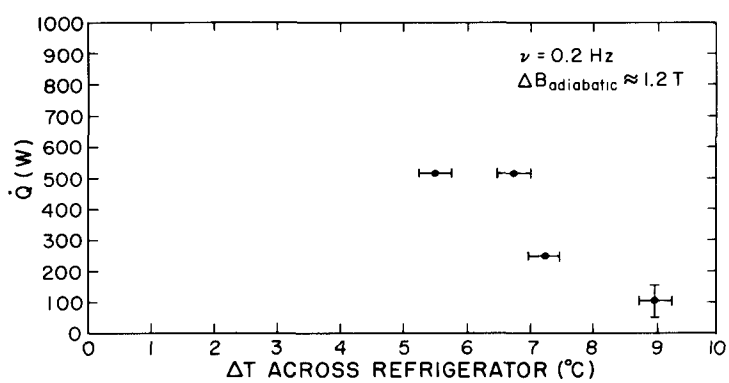

Figure 7-6. Thermal load added by a heater in the cold, external heat exchanger as a function of $T_H - T_C$ across the refrigerator. The flow was approximately balanced, the frequency = 0.2 Hz, and $\Delta B_{(adiabatic)}$ = 1.2 T.

which gives 293/7 = 41.9 for the ideal COP with a $7^{o}C$ span across the wheel. The real COP can be estimated from the torque measurements. If we use only the magnetic contribution when $T_H - T_C = 7^{o}C$, the torque is $\sim$ 28.3 Nm, which corresponds to 36 W at 0.2 Hz. If the cooling power at $7^{o}C$ is taken from the load curve as $\sim$400 W, then COP (real) = 11. The resulting efficiency of the wheel refrigerator is 26% for this operating point. The pumping power requirements and the magnet power requirements are not included, but considering everything that we know about the wheel, it is a reasonable result.

SUMMARY OF TEST RESULTS

The gadolinium wheel has operated successfully as a refrigerator and as a heat engine. The refrigeration load curve as a function of the temperature span across the wheel and an efficiency were determined. Experiments were performed to enable us to understand the operation of the wheel.

The following key problems limit the refrigeration capacity of the wheel.

A much smaller field change across the adiabatic sections of the wheel than was planned. The magnet did not reach its expected 6-T value and the gadolinium tended to reduce the gradient.

An internal refrigeration load from the entrained water. There was a partial failure of the counterflow mechanism to compensate for the entrained fluid.

Reduced heat transfer. We designed for an N_{tu} of $\sim$60 and obtained experimental values of 5. The exact reason is not completely understood, but is related to the sectioning of the gadolinium into 18 compartments and to flow fluctuations.

These three problems are soluble and at present do not pose any unexpected intrinsic limits on the wheel. We have found that the wheel works well in many aspects, such as the axial and circumferential seals, the pumping system, and the general instrumentation system.

Section 8

CONCLUSIONS

We can evaluate the performance of our gadolinium magnetic-wheel refrigerator compared with the performance originally expected and with that of comparable commercially available refrigerators. This comparison centers on three important relationships, those of refrigeration power ($\dot{Q}$), of efficiency (η), and of temperature span (ΔT) as functions of the effective magnetic field change (ΔB) across the adiabatic region of the wheel.

The original goals of $\dot{Q}$ = 1000 W, η = 70% of Carnot, ΔT = 40 K below ambient were not met but that the actual figures were approximately $\dot{Q}$ = 400 W, η = 26% of Carnot, ΔT = 7 K and that with no external load ΔT = 9 K. On the face of it, this comparison may seem discouraging; but a more thorough inspection of the situation reveals, we believe, that the experiments with the wheel were highly successful. The original goals were determined on the basis of ΔB = 6 T and heat exchanger quality (N_{tu}) = 60, whereas in fact the experiments were done with ΔB = 1.2 T and N_{tu} = 5. In the following we will, first, demonstrate that the observed performance under the latter conditions is entirely compatible with the expected performance under expected conditions, and, second, discuss the reasons for the diminished values achieved for ΔB and N_{tu}.

REFRIGERATION POWER vs MAGNETIC FIELD

The cooling power of the magnetic-wheel refrigerator is given from equation 2-15

$$\dot{Q}^C = \dot{m} C \nu \Delta_w, \tag{8-1}$$

where $\dot{m}$ and C are the mass of water flowing each cycle and specific heat of the water, ν is the rotation frequency, and Δ_w is the adiabatic temperature change during demagnetization of the gadolinium. The mass and specific heat are fixed by mass balance required for good heat exchange between the water and the gadolinium. The cooling power increases linearly

with frequency and with Δ_w. The experimental entropy-temperature curves for gadolinium show that Δ_w increases almost linearly with ΔB. We have plotted in Figure 8-1 the expected cooling power of our magnetic wheel at 0.2 Hz as a function of ΔB, using an average Δ_w obtained from the experimental entropy-temperature curves. THe experimental data point lies above the predicted curve because Δ_w is slightly larger near the CUrie point, where the load data were taken. On the curve of Figure 8-1, the X at ΔB = 6T shows that $\dot{Q}$ for the existing wheel would be 1450 W, comfortably above the expected 1000 W, but extrapolation of the data would give $\dot{Q}$ = 2100 W.

EFFICIENCY VS MAGNETIC FIELD

The efficiency of the magnetic refrigerator is a ratio of the real coefficient of performance (COP) to the ideal COP. THe ideal COP is the ratio of the cooling power to the work required, which can be reduced to

$$\text{COP (ideal)} = T_C/(T_H - T_C) \tag{8-2}$$

the real COP can be approximated by

$$\text{COP (real)} = \frac{\dot{Q}}{(\dot{Q}/T_C + \dot{S}_{irr})\, T_H - \dot{Q}} , \tag{8-3}$$

where $\dot{Q}$ is the cooling power and $\dot{S}_{irr}$ is the rate of entropy creation by heat transfer, friction, flow losses, etc., in the wheel. These two equations can be combined to give the efficiency η

$$\eta = \frac{1 - T_C/T_H}{(1 + \dot{S}_{irr}\, T_C/\dot{Q}) - T_C/T_H} . \tag{8-4}$$

For a fixed $\dot{S}_{irr}$, this equation shows that the efficiency increases as $\dot{Q}$ increases, and $\dot{Q}$ increases approximately linearly in ΔB, so the efficiency will increase as ΔB increases. The dependence on ΔB is shown in Figure 8-2, where $\dot{S}_{irr}$ has been adjusted to fit the experimentally observed efficiency of 26% at 0.2 Hz, ΔT = 7 K, and $\dot{Q}$ = 400 W. Using this value of $\dot{S}_{irr}$ and the extrapolation of the data in Figure 8-1 to 6T, we find η = 0.65, near to the goal of 0.70. For a fixed temperature span and frequency, $\dot{S}_{irr}$ is almost constant so Figure 8-2 gives a reasonable scaling curve of η vs B.

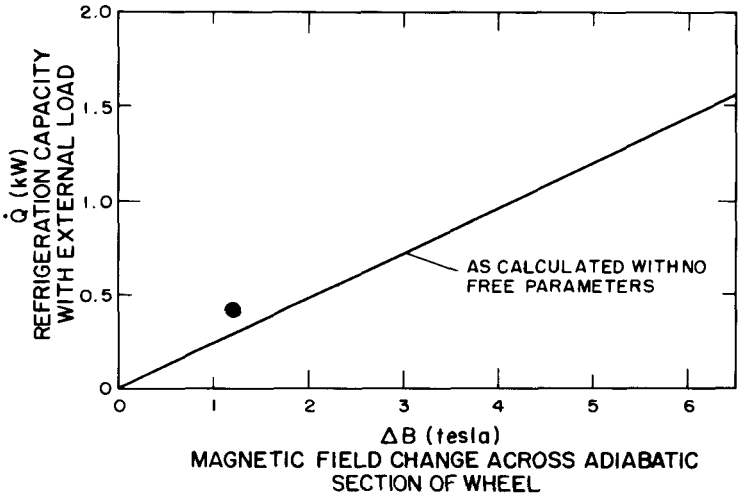

Figure 8-1. Calculated refrigeration capacity as a function of filled change across wheel. Experimental point is shown.

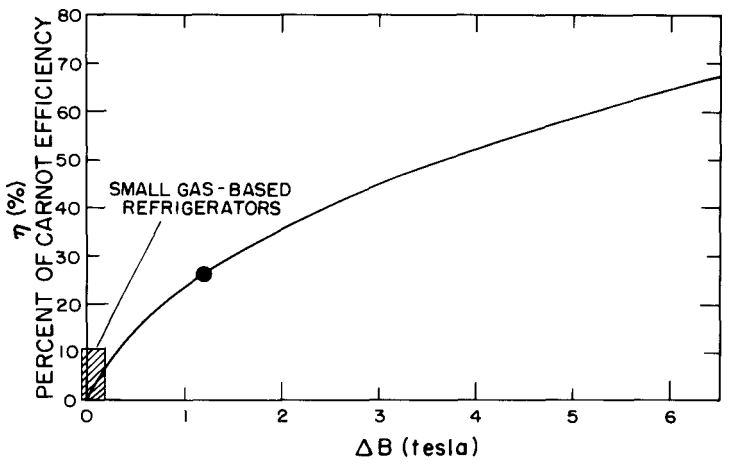

Figure 8-2. Calculated refrigerator efficiency as a function of field change across the wheel. Experimental point is shown.

The direct comparison of this refrigerator efficiency with other refrigerators and air conditioners is difficult because of the prototype-nature of the magnetic refrigerator. The shaded region on the efficiency axis shows the range of most existing small refrigerators. Gas-based refrigerators of 1 kW cooling power generally have efficiencies of less than 10% Carnot. For larger machines η increases, and only when the capacity increases to hundreds of kW does the efficiency approach 35%.

TEMPERATURE SPAN ΔT VS MAGNETIC FIELD

Experimental results from NASA and LASL show that the adiabatic temperature range of the gadolinium working material is very nearly proportional to ΔB. Reference 8 shows how ΔT is a strong function of the heat exchanger quality and also of the load. For small loads and $N_{tu} = 5$, the relation between ΔT and ΔB is given in Figure 8-3. To achieve the expected 40 K temperature span for a small load, it is seen that $\Delta B = 6T$ would do nicely; for larger load, N_{tu} would have to be increased to maintain the same ΔT at 6T.

DISCUSSION OF EXPERIMENTAL MAGNETIC FIELD

The magnet for the wheel refrigerator was designed to provide a 6T field at the top of the wheel. It was expected that this field would drop off to near zero at the bottom of the wheel. In fact, the highest field for reliable operation proved to be only about 4 T because of stresses in the coil and because the coil wire could be run at only about 75% of short-sample current.

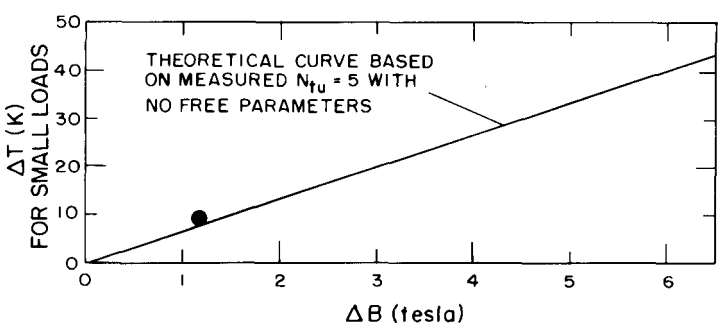

Figure 8-3. Calculated refrigerator span as a function of field change across wheel. Experimental point is shown.

Also the field at the bottom of the wheel only dropped to 21% of that at the top because the gadolinium homogenizes the field, and, most importantly, the maximum change in field in the adiabatic region during experiments with a load was only 1.2 T. The coil for this wheel is a rather complicated "race track" and cannot easily be shielded to improve this last figure.

It is clear, now, that the coil design used is hardly optimum. For example, it would be far better to use a solenoid and run the gadolinium on a flexible continuous belt through the bore of the coil. In such a design, ΔB could be raised to the 6 T level.

DISCUSSION OF EXPERIMENTAL HEAT EXCHANGER

The heat transfer in fine particles such as those used in the wheel was measured(12) and found to be sufficient to support expectations of a high N_{tu} for the heat exchanger. The fact that these expectations were not met is probably due to flow fluctuations of the water exchange medium (despite extensive efforts to minimize these), the extremely complex flow path of the water, and hold-up of fluid in the gadolinium pores. Future designs are planned to be far less complex and should achieve higher N_{tu}. Nevertheless, it should be recognized that an $N_{tu} = 5$ represents a very good exchanger.

Section 9

REFERENCES

1. F. Giauque, J. Am. Chem. Soc., Vol. 49, 1927, p. 1870 .

2. P. Debye, Ann. Physik, Vol. 81, 1926, p 1154.

3. W. F. Giauque and D. P. MacDougall, Phys. Rev., Vol. 43, 1933, p. 768.

4. This approach is covered in almost any text on Magnetism, see for instance A. H. Morrish, The Physical Principles of Magnetism, New York: Wiley, 1965, Chapter 6.

5. M. Griffel, R. E. Skochdopole, and F. H. Spedding, Phys. Rev. Vol. 93, 1954, p. 657. In all the work here, no effort has been made to arrive at very careful fits to the specific heat data, nevertheless, the required entropy results are more than accurate enough for our engineering application, see Fig. 2-2 for example.

6. T. F. Connolly and Emily U. Copenhaven, Biography of Magnetic Materials and Tabulation of Magnetic Transition Temperatures, (Solid State Literature Guides, Volume 5) New York: IFI/Plenum, 1973.

7. W. A. Steyert "Stirling Cycle Rotating Magnetic Refrigerators and Heat Engines for Use Near Room Temprature," W. A. Steyert, J. App. Phys. Vol. 43, 1978, p. 1216.

8. M. S. Islam and R. G. Scurlock, "Qualitative Details of the Complex Flow in Cryogenic Vapour Columns," Cryogenics, Vol. 17, 1977, p. 655.

9. See for example D. T. Paris and F. K. Hurd, Basic Electromagnetic Theory, New York: McGraw-Hill, 1969.

10. W. A. Steyert and N. J. Stone, "Low Flow Velocity, Fine-Screen Heat Exchangers and Vapor-Cooled Cryogenic Current Leads," Los Alamos Scientific Laboratory report, September 1978, LA-7395.

11. W. A. Steyert, "Heat Transfer and Flow Friction in Fine Porous Media," Los Alamos Scientific Laboratory report, September 1977, LA-6915-MS.

12. J. A. Barclay, W. A. Steyert, and D. R. Zrudsky, "Magnetic Refrigerator Development, June 1--August 31, 1978," Los Alamos Scientific Laboratory report, February 1979, LA-7605-PR.

13. R. C. Weast, Ed., Handbook of Chemistry and Physics, 57th ed. Cleveland, Ohio: CRC Press, 1976.

14. J. A. Gibson and G. S. Harvey, "Properties of Rare Earth Metals and Compounds," Air Force Materials Laboratory report, 1966, AFML-TR-65-430.

15. W. M. Kays and A. L. London, Compact Heat Exchangers, New York: McGraw Hill, 1964.

16. J. A. Barclay and W. A. Steyert, "Magnetic Refrigerator Development," December 1, 1978--February 28, 1979," Los Alamos Scientific Laboratory report, August 1979, LA-7781-PR .

APPENDIX A

WATER REQUIRED FOR BALANCED FLOW

To make the water and gadolinium flow rates in the actual wheel consistent with the requirements discussed in Section 2, we need three conceptually distinct flows.

ENTRAINED FLUID

Figure A-1 shows that as the wheel rotates, a quantity of entrained fluid moves with the gadolinium. During each rotation of a wheel of volume V, containing a volume fraction f of gadolinium, a volume of fluid V(1-f) moves counterclockwise across the imaginary plane, as in Figure A-1. However, if the pump pushes that same quantity of fluid clockwise around the wheel, it will be as if the fluid is stationary in the laboratory reference frame and the effect of entrainment in this simplified picture is then eliminated. Therefore, we require a flow rate to cancel the entrained fluid V_E given by

$$\dot{V}_E = V(1 - f)\ \nu. \qquad \text{(A-1)}$$

STRUCTURAL SPECIFIC HEAT

If the structural mass m of the wheel (with specific heat C_m) is in thermal contact with the water, heat will be transferred as a load on the refrigerator. The effect of this rotating mass is nullified by circulating a water flow V_s, given by

$$\dot{V}_s = \frac{\dot{m}\ C_m}{C_W \rho_W} \quad . \qquad \text{(A-2)}$$

where C_W and ρ_W are the specific heat and density of water.

HEAT TRANSFER FLUID

Figure A-1 shows the fluid required to transfer heat to and from the gadolinium (of specific heat C_g). Precisely balanced flow of the heat transfer fluid V_H is required in the upper and lower exchanger sections of the wheel, shown by the dashed arrows in Figure A-1. This flow rate is given by

$$\dot{V}_H = \frac{Vf \quad \nu C_g \ \rho_g}{C_W \rho_W} \quad . \tag{A-3}$$

TOTAL FLUID FLOWS

For flow through the adiabatic sections of the wheel (the section between the fluid ports on the right and left of Figure A-1) the proper flow is the sum of $\dot{V}_E$ and $\dot{V}_S$. For flow through the heat exchanger sections (indicated by broken arrows at the top and bottom of the wheel of Figure A-1b) the proper flow is the sum of $\dot{V}_E$, $\dot{V}_S$, and $\dot{V}_H$.

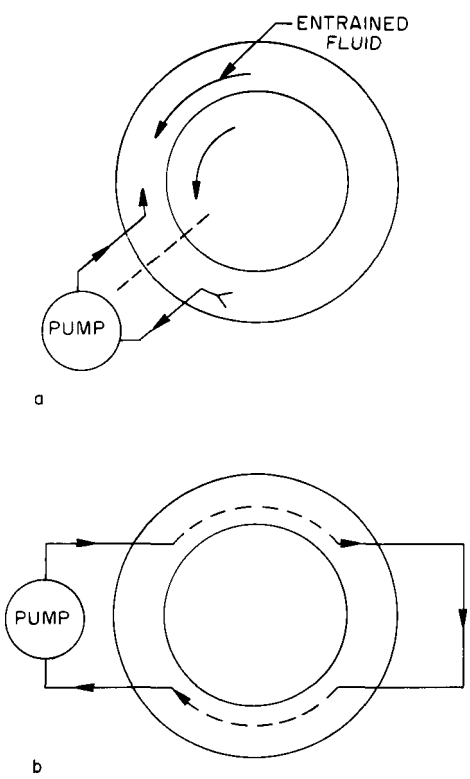

Figure A-1. Fluid flow in wheel. Figure (a) shows entrained fluid circulating with the wheel, which the pump counteracts. Figure (b) shows the fluid required for balanced flow in the heat exchanger.

APPENDIX B

PUBLICATIONS AND TALKS

EPRI PROGRESS REPORTS

1. W. A. Steyert, "Magnetic Refrigerator Development, September 1--November 30, 1977," Los Alamos Scientific Laboratory report LA-7165-PR (March 1978).

2. J. A. Barclay and W. A. Steyert, "Magnetic Refrigerator Development, December 1, 1977--February 28, 1978," Los Alamos Scientific Laboratory report LA-7257-PR (June 1978).

3. J. A. Barclay and W. A. Steyert, "Magnetic Refrigerator Development, March 1--May 31, 1978," Los Alamos Scientific Laboratory report LA-7390-PR (September 1978).

4. J. A. Barclay, W. A. Steyert, and D. R. Zrudsky, "Magnetic Refrigerator Development, June 1--August 31, 1978," Los Alamos Scientific Laboratory report LA-7605-PR (February 1979)

5. J. A. Barclay, W. A. Steyert, and D. R. Zrudsky, "Magnetic Refrigerator Development, September 1--November 30, 1978," Los Alamos Scientific Laboratory report LA-7654-PR (March 1979).

6. J. A. Barclay and W. A. Steyert, "Magnetic Refrigerator Development, December 1, 1978--February 28, 1979," Los Alamos Scientific Laboratory report LA-7781-PR (August 1979).

7. J. A. Barclay and W. A. Steyert, "Magnetic Refrigerator Development, March 1--May 31, 1979," Los Alamos Scientific Laboratory report LA-7913-PR (October 1979).

8. J. A. Barclay, J. C. Bronson, and W. A. Steyert, "Magnetic Refrigerator Development June 1--August 31, 1979," Los Alamos Scientific Laboratory report LA-8066-PR (December 1979).

OTHER PUBLICATIONS AND TALKS RESULTING FROM THIS WORK

9. W. A. Steyert, "Small Magnetic Refrigerators to Pump Heat from Helium Temperatures to above 10 K," presented at the Cryocooler Conf., Boulder, CO, October 3-4, 1977, published as NBS Special Publication 508.

10. G. R. Stewart, J. A. Barclay, and W. A. Steyert, "The Specific Heat of C- plus Gd_2O_3, Solid State Communication 29, 17 (1979).

11. W. A. Steyert, "Magnetic Refrigerators for Use at Room Temperature and Below, Invited talk presented at the 15th International Low Temperature Conference, August 23-29, 1978, Grenoble, France, Proceedings of LT15, Journ. de Physique 39, C6-1598 (1978).

12. W. A. Steyert, "Magnetic Refrigerators and Heat Engines," Invited talk to the Spring Meeting of the German Physical Society, Munster, West Germany, March 14, 1979.

13. W. A. Steyert "Refrigerators and Heat Engines Using Solid Working Materials," Colloquium, Oregon State University, Corvallis, Oregon, November 5, 1979.

14. W. A. Steyert, "Refrigerators and Heat Engines Using Solid Working Materials," Solid State Seminar, University of Oregon, Eugene, Oregon, November 7, 1979.

PART B

RECIPROCATING REFRIGERATORS

Section 1

INTRODUCTION

The idea that components constructed of superconducting materials can provide significant operational and economic benefits in electric power systems is becoming increasingly more credible. In particular, in this country, EPRI and the U.S. Department of Energy (DOE) have appreciated the large potential advantages which could be realized through use of high capacity ac and dc superconducting power transmission lines (SPTL) and are funding developments in these areas. Calculations a well as experimental results have already assured the feasibility of SPTL systems and that no insuperable technical barriers should arise to prevent the introduction of superconducting cables into the electric power grid, by perhaps as early as the late 1980's. Thus the emphasis in the development of SPTL systems has turned to optimization of the realiability, safety, efficiency, and economic aspects of the various components comprising such systems. The refrigeration sub-system, required to maintain the low temperature environment for SPTL's, provides an example where improvements in existing technology could significantly expedite the commercialization of superconducting cables.

For application in SPTL systems refrigerators must serve at least three separate functions, each of which makes different demands on the refrigerator. The first function is that of cool-down of the unloaded line; and this is followed by steady state refrigeration under operating conditions. The third requirement is for cooling of the cryogenic potheads to remove heat leak at I^2R losses generated in the normal metal leads (e.g., copper) by the high currents typical of SPTL operation. Specification for one or more types of refrigerators for these purposes will depend on a large number of possible SPTL characteristics, such as: operating temperature, current, and voltage; thermal shielding design of the cable; pressure and pressure drop in the cryogenic coolant; whether the cable is ac or dc (the latter will not suffer ac power losses associated with either dielectric dissipation in the insulation or hysteretic effects in the superconductor); separation between refrigeration stations; etc. However, in spite of the large number of system variables, it is possible to select rather reasonable

Section 2

THEORY OF ACTIVE MAGNETIC REGENERATION

The basic theory of the active magnetic regenerator is that of an ordinary regenerator, except that the temperature of the material can be changed by the application or removal of a magnetic field and that a thermal wavefront propagates back and forth in the regenerator. Each different material executes a small Brayton cycle near its Curie temperature, but when all the materials are combined, they yield a Brayton cycle over an extended temperature range. The basic cycle is described as follows: Consider a porous-bed regenerator composed of a series of different ferromagnetic materials whose Curie temperatures gradually change from the hot bath temperature T_H to the cold-bath temperature T_C. Also consider that the cycle begins with the porous bed at temperature T_H at one end and T_C at the other end thereby establishing a temperature gradient along the regenerator. Consider that the temperature gradient is uniform but displaced to the left of center in the regenerator. Upon application of a magnetic field, the temperature all along the bed will adiabatically increase by ΔT, which might be about 16-20K for a 10-T field. After the field is applied, then helium or hydrogen gas, at temperature $T_C+\Delta T$ is pushed through the bed from the cold end, which is now at $T_C + \Delta T$. As the gas at $T_C+\Delta T$ enters the bed, the gas will warm as the bed cools and a thermal wavefront will propagate through the bed. The gas leaves the regenerator at $T_H + \Delta T$ until the wavefront arrival at the right of the regenerator causes the temperature of the exiting to just start decreasing. When this happens, the gas flow into the cold end is stopped, and the regenerator is adiabatically demagnetized. The temperatures all along the bed drop by ΔT. The gas coming out of the regenerator at $T_H+\Delta T$ during the magnetized state is put through a heat exchanger, cooled to T_H, and now is put back into the regenerator. Another thermal wavefront travels in the opposite direction to the first thermal wavefront as gas at T_H is pushed into the regnerator. The gas exits at T_C, and is put through a load heat exchanger to be heated to $T_C+\Delta T$. When the cold gas temperature at the end of the regenerator just decreases from $T_C+\Delta T$, the gas flow is stopped and the cycle now repeats as the regenerator is again magnetized. A quantitative description of simple wavefront propagation is given in Appendix A.

Section 3

RESULTS ON ACTIVE MAGNETIC REGENERAION

POROUS-BED HEAT TRANSFER EXPERIMENTS

The successful operation of an active magnetic regenerator depends on good heat transfer between the gas and the magnetic solid. Porous bed correlations in the literature[1,2] suggested that excellent heat transfer could be obtained with tolerable pressure drops.[3] Since we have previous experience[4] with porous beds that suggested the effective heat transfer was much worst than expected, we decided to make several test beds to determine whether excellent heat transfer could be obtained. This section of the progress report describes these experiments.

Theory of Heat Transfer in Porous Bed

The theory of thermal wave propagation through a porous bed was presented approximately forty years ago.[5] The basic, one-dimensional equations for heat transfer in a porous bed are

$$\alpha \rho_f c_f \frac{\partial T}{\partial t} = - \dot{m}_f c_f \frac{\partial T}{\partial x} + ha (\Theta - T) \tag{3-1}$$

$$(1 - \alpha) p_s c_s \frac{\partial \Theta}{t} = ha(T - \Theta) + (1 - \alpha) g_s \frac{\partial^2 \Theta}{\partial x^2} \tag{3-2}$$

where α is the porosity, ρ_f and ρ_s are the densities of the fluid and solid, respectively, c_f and c_s are the heat capacities of the fluid and solid, respectively, $\dot{m}_f$ is fluid mass flow rate, T and Θ are the temperatures of the fluid and solid, respectively, a is the contact area per unit volume of the bed, and λ_s is the effective axial thermal conductivity of the bed. If the heat capacity of the gas is neglected and we assume that the second derivatives of the temperatures are equal, i.e.,

$$\frac{\partial^2 T}{\partial^2 x} = \frac{\partial^2 \Theta}{\partial^2 x} \quad , \tag{3-3}$$

then eqs. (3-1) and (3-2) can be written as a single equation.[6]

$$(1-\alpha)_s \rho_s c \frac{\partial\Theta}{\partial t} = \left(\lambda_o + \frac{\dot{m}_f^2 c_f^2}{ha} \frac{\partial^2\Theta}{\partial x^2}\right) - \dot{m}_f c_f \cdot \frac{\partial\Theta}{\partial x}\Bigg) \qquad (3\text{-}4)$$

where λ_o is the static bed thermal conductivity. Note that the assumption of infinite conductance is <u>not</u> required. Equations (3-4) or (3-1) and (3-2) have been numerically solved by finite difference techniques to predict the propagation of a thermal wave as a function of time. Near room temperature both solutions give almost identical results. For a given bed of well-defined particles, the effect of λ_o is negligible except at very low mass flow rates, e.g., 0.1 g/s. Therefore, at $\dot{m}_f$ = 2 g/s, the only adjustable parameter of the calculation is h.

<u>Experimental Bed</u>:

We prepared porous beds 15.2 cm long, 3.7 cm diameter that were filled with 0.15 cm Pb balls, 0.32 cm stainless steel balls, Fe chips approximately 0.018 cm x 0.025 cm x 1.27 cm, and Gd chips approximately 0.020 cm x 0.039 cm x 0.38 cm. The porosities of the beds were 0.42 for Pb, 0.40 for S.S., 0.80 for Fe, and 0.80 for Gd. Another Pb-ball bed was prepared with α = 0.40 after more careful screening of the Pb balls so the particles were more uniform. Copper-constantan thermocouples were located at 2.5 cm, 7.5 cm, 12.5 cm with inlet and outlet thermocouples about 1 cm in front of and behind the bed in the connecting hoses. The inlet hoses were connected to a valving arrangement that allowed very rapid switching from a cold stream to a hot stream of gas. The exit hose was connected to a flowmeter in some of the experiments. Temperatures were recorded on two 4-pen chart recorders.

The basic experiment consisted of preparing a bed at an equilibrium temperature, usually about 20^{0}C, then rapidly switching to hot gas at approximately 40^{0}C. THe inlet thermocouple generally measured a square thermal wave and succeeding thermocouples measured a slightly more dispersed wave. Most experiments did not have a precise meaurement of the mass flow rate but this is easily obtained from the experimental curves because the midpoint of the thermal wave must propagate according to the first law of thermodynamics, i.e.,

$$\dot{m}_f c_f \, \Delta T = m_s s_x \, \Delta\Theta/\Delta t \qquad (3\text{-}5)$$

where m_s is the mass of the solid from the inlet to the position of the thermocouple and Δt is the time the midpoint of the wave takes to reach that position. Because $\Delta T = \Delta\Theta$, then

$$\dot{m}_f = m_s c_s / c_f \Delta t. \tag{3-6}$$

Having obtained $\dot{m}_f$, the experimental curves were fitted with numerical solutions to Eq. (3-1) and (3-2) or (3-4) with variable h until a good fit was obtained. The values of h were then checked against conductance correlations in the literature[1,2] and the agreement was quite good. An experimental result for Pb balls is shown in Figure 3-1 and the corresponding theoretical curves are shown in Figure 3-2. The heat transfer characteristics of the bed can be expressed at $N_{tu} = h\,A/\dot{m}_f c_f$ with $A = aV$ where V is the volume of the bed. There are several subtle effects that show up in the experimental curves. For example, the temperatures do not all converge at large times as one would ideally expect. This is due to the heat loss to the outside world. The roll off of the curves as T_H is approached is due to the thermal mass of the container and a conribution from the changing properties of the gas with temperature. The key conclusion of these experiments is that it is possible to design and build porous beds with excellent heat transfer such that N_{tu}'s in the range 10-100 are easily obtainable.

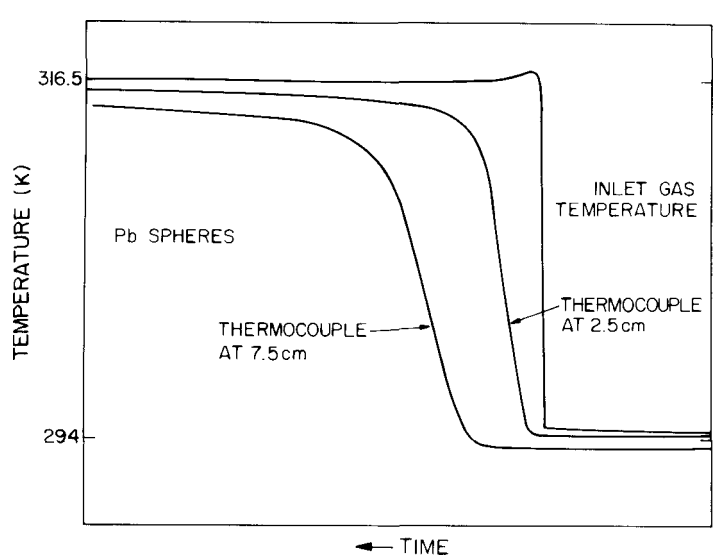

Figure 3-1. Experimental result for heat transfer of air in a Pb-ball porous bed.

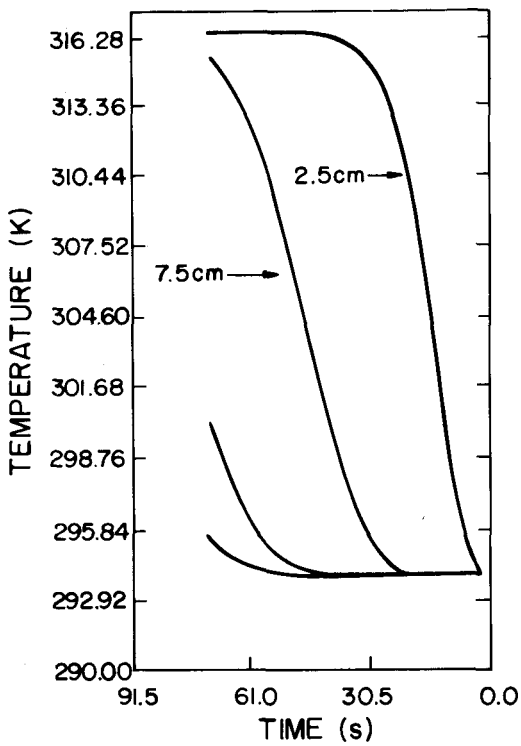

Figure 3-2. Theoretical result for heat transfer of air in a Pb-ball porous bed giving a N_{tu} = 25 ± 15.

GADOLINIUM-AIR EXPERIMENTS

Dewar

As reported earlier,[7] the annular Dewar required for the room-temperature, Gd-air, reciprocating magnetic refrigerator tests was successfully designed and built. The earlier analysis showed that the commercial magnet leads to the 9-T magnet were the dominant heat leak into the Dewar. We replaced the braided copper-superconductor leads with vapor-cooled leads of our own design and remeasured the boil-off rate of the Dewar. The boil-off rate dropped to about 0.8-ℓ/h after the initial transfer transients.

Gd-Air Design No. 1

The initial design of reciprocating gadolinium efrigerator using air a the heat exchange fluid was reported in reference 7 and is schematically shown in Figure 3-3. A mistake in the initial viscous-flow pressure drop lead us to believe that a cylindrical, porous bed of Gd would make a good design for a

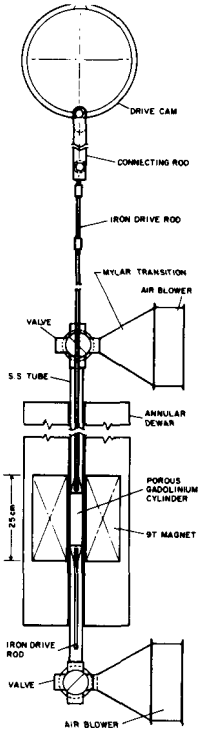

Figure 3-3. Experimental setup for gadolinium reciprocating heat pulse air refrigerator.

low-power (100 W) refrigerator. However, after the construction was already well under way, the mistake was uncovered and showed that the cylindrical design was a poor design because of large viscous losses. By operating at low frequencies, η = 0.02 Hz, the experiments could still be performed but the net power was expected to be only $\sim$ 10 W. The basic concept of an active magnetic regenerator could still be tested and the reciprocating design could be checked.

Gd-bed Construction

The gadolinium chips had average dimensions of 0.020 cm x 0.039 cm x 0.38 cm. The stainless steel container was 3.63 cm i.d. with 0.89 cm walls and 15.2 cm long. The gadolinium was pressed into the cylinder in six sigments, each $\sim$ 2.54 cm long. The ends of the cylinder were closed with 40 mesh Cu screen ($\sim$ 100 x less impedance than Gd) and a 20 mesh Cu screen was put between each of the segments to help ensure uniform flow in the bed. A total of 261 g of Gd was used in the bed which results in a porosity of 80%.

The approximate pressure drop through the porous Gd bed was measured and roughly agreed with the pressure drop predicted in Ergun's equation[3], i.e.,

$$dP = \left[\frac{150\ (1-\alpha)}{D_p G_o/\mu} + 1.75\right] \frac{(1-\alpha)}{\alpha^3} \frac{L}{D_p} \frac{G_o^2}{\rho_f} \tag{3-7}$$

where D_p is the effective particle diameter, G_o is the mass flux, μ is the fluid viscosity, and L is the bed length. The heat transfer was measured using the same experimental apparatus as described peviously. The measured N_{tu} was 88 $\pm$ 10. This value of N_{tu} is spanned by calculated values from correlations in the literature.[1-2] The more reliable of these correlations predicts a lower N_{tu} but uses an effective particle diameter given by

$$D_p = 2\left(\frac{3\ xyz}{4\pi}\right)^{1/3} \tag{3-8}$$

where x, y, and z are the chip dimensions. Equation (3-8) obviously equally weights the long dimension and therfore will over estimate the practical particle diameter because flow will not be uniform around all dimensions of the chip. Because the N_{tu} increases with decreasing particle diameter, the observed N_{tu} is greater than the calculated value.

The cylinder of porous gadolinium was put in the apparatus described in reference 7 and shown in Figure 3-3. The first experiment that we performed was the measurement of the magnetic forces. We had calculated that a 0.64 cm Fe rod above and below the Gd cylinder would be approximately magnetically equivalent to the Gd at the mean operating temperature. However, in these calculations, the magnetization of the Gd was only approximately determined and therefore the force balance was only approximate. The acutal resultant force was measured using a strain-gauge transducer and a bridge circuit incorporating a lock-in amplifier. The experimental results taken with the Gd at T = 268 K and B_{max} = 2.0 T are shown in Figure 3-4. The sense of the force is that positive values are tensile and negative values are compressional at the strain gauge on the drive shaft. The conclusion of our first experiment was that the Fe rods above and below the Gd cylinder did not compensate the forces very well. We tried to adjust the forces by adding more Fe to the end of the bottom Fe rod as shown in Figure 3-4, experimental curve #2. We also added more solid Gd to the bottom of the Fe rod to improve the

force compensation. We eventually were able to operate at 6 T but bent the drive shaft as the compressional forces got bigger with increasing field. It became clear from the force experiments that the force calculations needed to be done much more exactly.

The basic equation for magnetic force is

$$\underset{\sim}{F} = (\underset{\sim}{M} \cdot \nabla)\, \underset{\sim}{B} \tag{3-9}$$

where F is the force vector, M is the magnetization, and B is the field. Equation (3-9) reduces to the following expressions for cylindrical symmetry:

$$F_x = i\,(m_x \frac{\partial B_x}{\partial x} + m_z \frac{\partial B_z}{\partial x}) \tag{3-10}$$

$$F_z = k\,(m_x \frac{\partial B_x}{\partial z} + m_z \frac{\partial B_z}{\partial z} \tag{3-11}$$

where i, k are unit vectors in the x and z direction, respectively, and m_x and m_z are the components of m = MV where V is the volume of the magnetic material. The value of m is a function of B and T and is rapidly changing for Gd but essentially constant for Fe near room temperatue. This fact makes it impossible to exactly compensate the Gd forces with Fe for all B at any temperature near room temperature. The forces expected from the different components of the system are shown in Figure 3-5. If the appropriate forces for the apparatus are added then the calculated curves shown in Figure 3-4 are obtained. The agreement between the theory and experiment is excellent except at the high end of the stroke, i.e, when the Gd is far out of the magnet. The difference between calculated and measured forces is probably due to the demagnetization of the Fe as it moves out of the field, i.e, as $B \leq 0.2$ T, the magnetization of Fe rods falls from its saturation value due to domain reorientation and reformation. The key conclusion from the force experiments and calculations is that for reciprocating refrigerators, the magnetic work required for the refrigeration cycle is produced by a force which is the difference between two much larger forces. A compensation mechanism using solid Gd and Fe rods above and below the working cylinder is possible but requires careful design to avoid large parasitic losses.

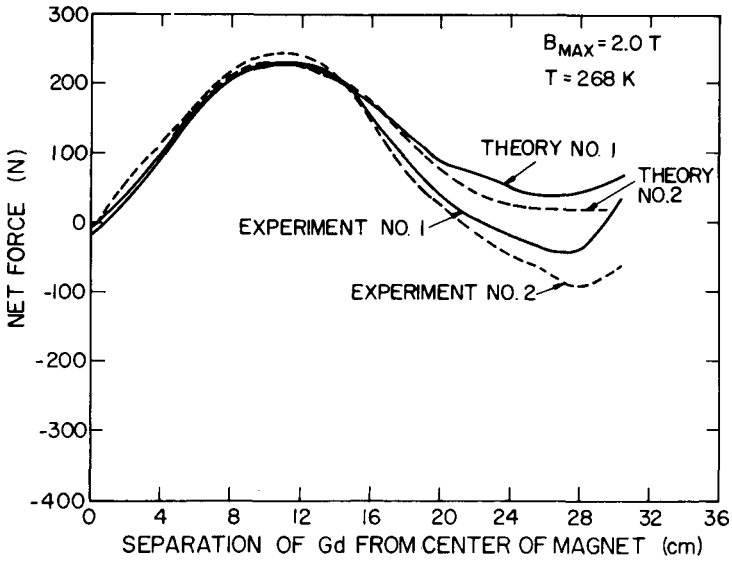

Figure 3-4. Experimental and theoretical force measurements for Gd-Air design No. 1. Curves labeled No. 1 are for a 30 cm Fe rod above and below the 15 cm Gd pill. Curves labeled No. 2 are for a 30 cm Fe rod above and a 39 cm Fe rod below the Gd pill. See Figure 3-5 for individual forces on the components.

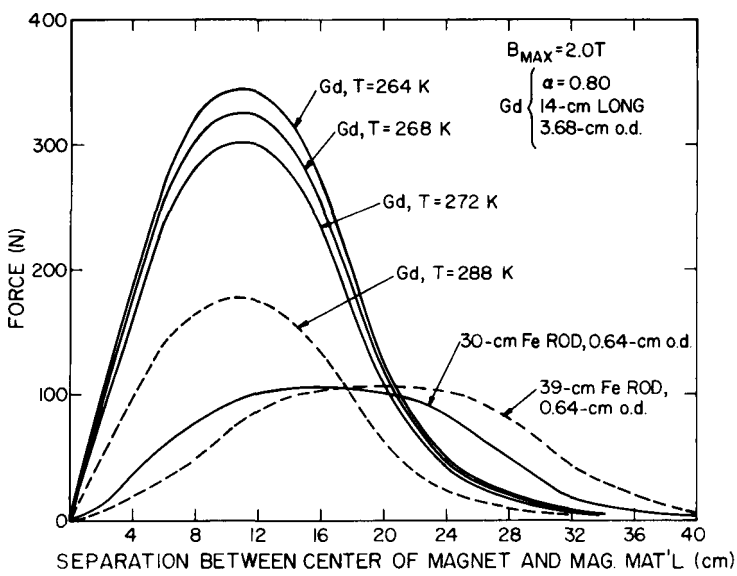

Figure 3-5. Calculated forces for various components of Gd-air design No. 1.

The next experiment we did was to measure the performance of the gadolinium cylinder as a refrigerator and test whether the active magnetic regenerator cycle would work. The results of one run at 4.0 T are shown in Figure 3-6. There are five temperature excursions plotted in Figure 3-6, showing the increase and decrease in temperature as the Gd is adiabatically magnetized and demagnetized. The end vectors show that the air going into the bottom of this porous bed is hotter than the air coming out of the bottom and the air coming out of the top of the porous bed is hotter than the air going into the top in another part of the cycle. The results of Figure 3-6 show that the basic active magnetic regenerator concept works on the limited scale of this experimental run. The temperature span is small and the temperature excursions are also relatively small because ΔB was 4 T and not 9 T. The thermal mass of the container also limits the temperature excursions to about half of the free Gd case. Another complication in this particular experimental run was that the air flow rates from the top and bottom were

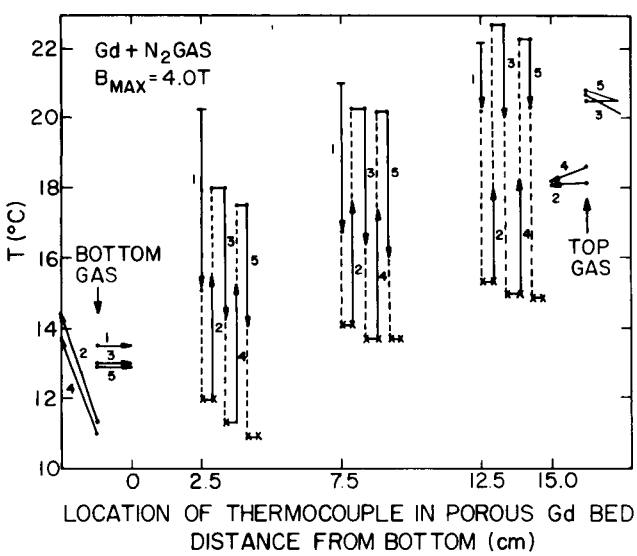

Figure 3-6. Temperature excursions of gadolinium and gas for Gd-air design No. 1. There are five excursions in temperature as the Gd is put into and out of the magnetic field. The dashed portions are during magnetization or demagnetization and the solid portions are during the gas flows from either end.

different, which limits the refrigeration capacity of the refrigerator. We tried larger temperature spans in this design but without balanced mass flows and large parasitic losses of the design no sensible results were obtained. The experiment did help immensely in the design of Gd-air No. 2.

Gd-Air Design No. 2

Following the first set of experiments we redesigned the apparatus with the following considerations:

- Eliminate any thermal addenda possible
- Have equal mass flow rates in each direction, i.e., no leaks
- Insulate the tube inside the annular tube of the Dewar to eliminate parasitic cooling from the vapor and radiation.
- Balance forces very carefully
- Improve instrumentation
- Reduce viscous flow pressure drop

All of these considerations have been taken into account in Gd-air design No. 2. The tube inside the annular Dewar has been insulated and careful seals using O-rings have been made. THe gadolinium cylinder has been redesigned to reduce parasitic losses and thermal mass by using nylon instead of stainless steel and designing a thermal isolating suspension system. The viscous loss has been reduced by replacing the cylindrical shape with a rectangular shape with the flow path through the short dimension of the rectangle. The forces have been balanced at 8 T for room temperature operation, as shown in Figure 3-7, where we can see that the net force of $\sim$ 445 N (100 lbs_f) is required to do the magnetic work for the thermodynamic cycle. The parts for this design have all been built and are ready for testing. We have also decided that He gas is much better than air, so the next experiments will use He gas.

GADOLINIUM WATER EXPERIMENTS

Experimental Details

The experimental setup of Figure 3-3 was used. However, in place of air, water is moved through the gadolinium. The magnetic regenerator is 12 cm long, 3.7 cm in diameter and contains 638 g of spherical gadolinium particles. This gives a filling portion of 66.5%. The spherical particles were screened to 325 mesh (U.S. Standard); particles smaller than 325 mesh were rejected.

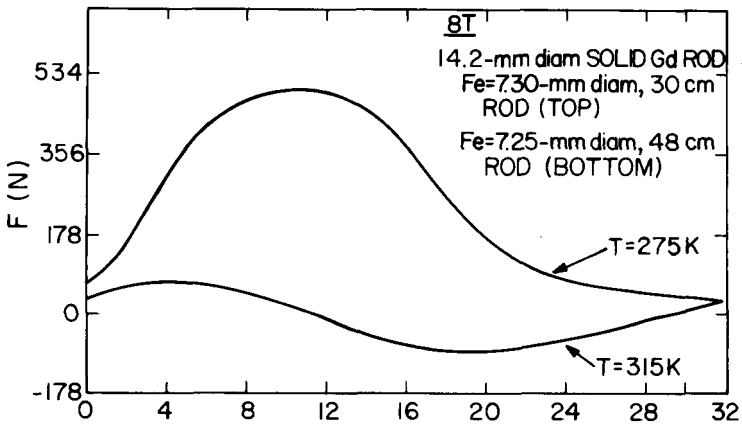

Figure 3-7. Net force on gadolinium-air refrigerator.

Because of the large forces involved in moving the gadolinium into and out of the magnetic field, it was decided to operate the refrigerator in a mode where the magnet is turned on and off to execute the cycle. Thus, the drive mechanism of Figure 3-3 was not needed.

There were seven copper-constantan thermocouples used to monitor the temperature during the refrigeration cycles. Four were located on the four 3-mm-diameter fluid inlet and outlet tubes, about 2 mm above the end cap. Three were located on the outside of the can, one was 2 mm below the top end cap, one was 2 mm below the bottom end cap, and one was located in the center of the can. The magnitude of the field changes for magnetization and demagnetization in these experiments was 4 T.

Results

Each cycle 50 cm^3 of water was moved through the gadolinium bed in about 45 s; 3 or 6 min were required to charge and discharge the magnet. The pressure drop through the porous bed was measured as about 0.03 MPa (5 psi). This is consistent with the pressure drop expected for a porous bed calculated from Eq. 3-3.

Figure 3-8 shows the temperature history of the seven thermocouples toward the end of an experimental run. It is necessary to cycle about 8 times until start-up transients have died out.

The refrigeration capacity and span can be deduced from these temperature recordings and are summarized in Figure 3-9. The results represent the consistent value from a number of cycles after initial transients have died out. The cooling capacity C is given for 50 cm^3 throughput:

$$C = V\,C_p\,\Delta T = 50 \times 4.18 \times (T^B_{in} - T^B_{out}) \qquad (3\text{-}12)$$

where $T^B_{in} - T^B_{out}$ represents the mean temperature change of the water as it leaves the bottom of the refrigerator. The temperature span S is given by

$$S = (T^T_{in} + T^T_{out})/2 - (T^B_{in} + T^B_{out})/2 \qquad (3\text{-}13)$$

where the superscript T indicates values of the top of the refrigerator. The temperature quantities for Eq. (3-12) and Eq. (3-13) are indicated in Figure 3-9.

Expected Performance

Because of the long pause to bring the magnet up to its maximum field for these runs (4.5 T) and to bring it down to its lowest field ($\sim$ 0.5 T) a large quantity of conduction loss results. First, there is a longitudinal conduction from the hot, upper, section of the cylinder to the cold, lower, section of the cylinder. The heat flow rate is calculated to be

$$\dot{Q}_\ell = 0.025\ \Delta T \quad . \qquad (3\text{-}14)$$

$\dot{Q}_\ell$ is the heat flowing along the length of the gadolinium-packed refrigerator cylinder caused by a uniform temperature gradient ΔT that is the temperature difference between the top and the bottom of the cylinder.

The most important heat flow is the flow of heat $\dot{Q}_W$ from cylinder to the surrounding Dewar walls. By heating a copper rod, the same size as the refrigerator cylinder, and inserting it into the Dewar in place of the cylinder this heat flow was measured. We found

$$\dot{Q}_W = 0.3\ \Delta T \quad . \qquad (3\text{-}15)$$

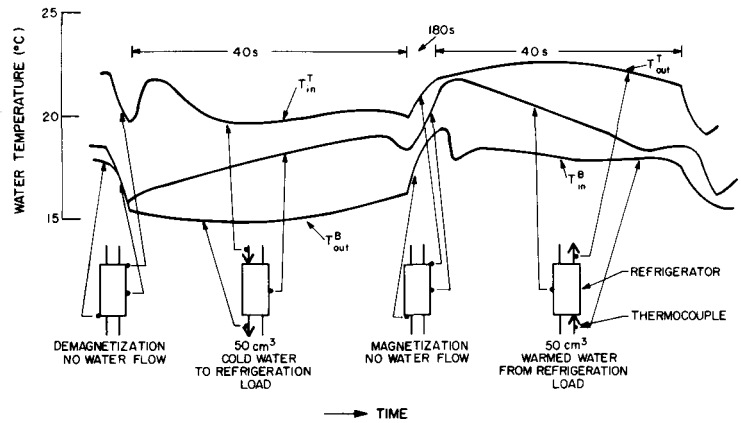

Figure 3-8. Experimental Design No. 2. Temperatures of water entering and leaving the refrigerator during a complete cycle. Temperature at the middle of the refrigerator is also shown.

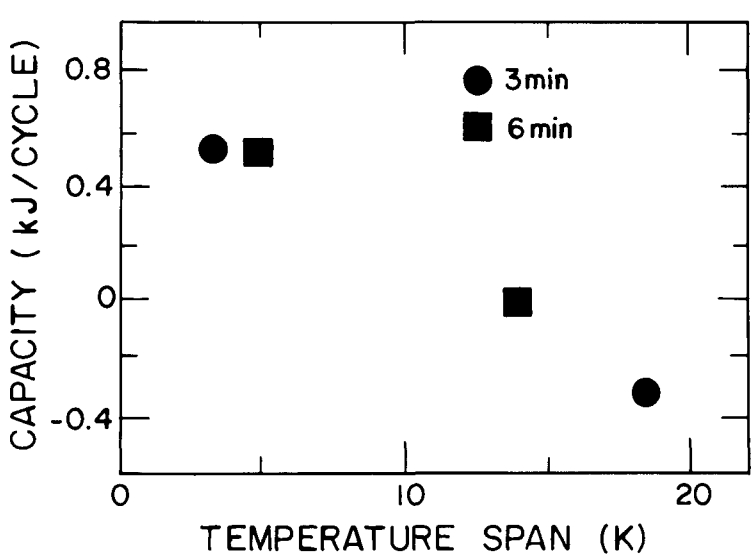

Figure 3-9. Experimental refrigeration capacity versus temperature span.

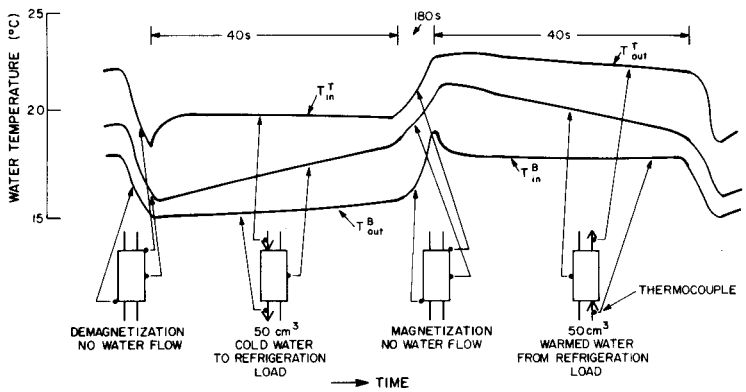

Figure 3-10. Calculated temperature of water entering and leaving the refrigerator during a complete cycle. Calculated temperature at the middle of the refrigerator is also shown.

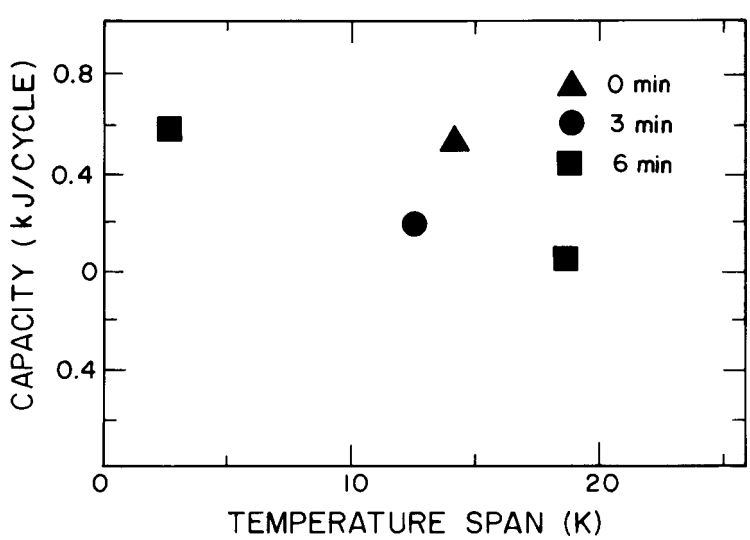

Figure 3-11. Calculated refrigerator capacity versus temperature span.

This energy flow heats and cools the walls of known specific heat, C = 85 J/K, over the 12 cm length of the refrigerator.

All these factors can be put into a computer program which calculates the curves as shown in Figure 3-8 and can be reduced to the data of Figure 3-9. These results are shown in Figure 3-10 under the same conditions as tested experimentally in Figure 3-8. The curves of Figure 3-10 from the computer can be analyzed as wa the experimental data to yield the results of Figure 3-11.

A comparison of Figures 3-9 and 3-11 shows that for small spans, the refrigerator performs as expected, a little under 0.5 kJ/cycle capacity. At the largest temperature spans ($\sim$ 19 K) the capacity expected is near 0 kJ/cycle while the measured capacity is nearer to -0.3 kJ/cycle.

Section 4

CONCUSIONS

The reciprocating refrigerator experiments have shown that the active magnetic regeneration concept works, at least over restricted temperature spans. The magnetic force compensation mechanism and the parasitic loss from thermal addenda are shown to be the key problems at this state of development. The wheel design compensates forces much more conveniently than the reciprocating design. Since the entrained fluid is used in a reciprocating design, this problem is eliminated. The axial bed conduction is a potential problem but further work is needed to clearly decide. Liquids are clearly better heat transfer fluids than gases for cylindrical reciprocating designs because of the viscous-flow losses caused by large volume flows in gases which in turn are due to the low heat capacity of the gases.

Section 5

REFERENCES

1. J. E. Coopage and A. L. London, "Heat Transfer and Flow Friction Characteristics of Porous Media," Chem. Eng. Prog., Vol. 52, 1956, p. 52.
2. E. R. G. Eckert and R. M. Drake, Jr., Heat and Mass Transfer, McGraw-Hill, New York, 1959.
3. R. Bird, W. Stewart, and E. Lightfoot, Transport Phenomena, John Wiley and Sons, New York, 1960, Chap. 6.
4. J. A. Barclay and W. A. Steyert, "Magnetic Refrigerator Development," March 1 - May 31, 1979," Los Alamos Scientific Laboratory report LA-7913-PR, October 1979.
5. T. E. W. Schumann, "Heat Transfer; A Liquid Flowing Through a Porous Prism," J. Franklin Inst., Vol. 208, 1919, p. 405.
6. D. Vortmeyer and R. J. SChaefer, "Equivalence of One- and Two-Phase models for Heat Transfer Processes in Packed beds: One Dimensional theory," Chem. Eng. Sci, 29, 485 (1974).
7. J. A. Barclay and W. A. Steyert, "Magnetic Refrigerator Development," June 1 - August 31, 1979, Los Alamos Scientific Laboratory report, LA-8066-PR, December 1979.

APPENDIX A

SIMPLIFIED MODEL OF ACTIVE MAGNETIC REFRIGERATOR

In order to allow simple mathematical modeling we have represented the gadolinium entropy curves of Figure 2-3 of Part A as

$$S/R = aT + \text{constant} \quad (S \text{ in J/g-ion-K}) \tag{A-1}$$

These are shown in Figure A-1. From the experimental data of Figure 2-3 of Part A we obtain $a = 0.016K^{-1}$ and in a field of 6 T $\Delta = 8$ K.

Consider a reciprocating magnetic refrigerator laid on its side as shown in Figure A-2. We inject a stream of fluid in the left hand side ($x = 0$); it flows at the rate $\dot{m}$ moles per second ($\dot{m}$ is negative if fluid flows from right to left) and its entropy per mole is given* by

$$S/R = cT + \text{constant} \tag{A-2}$$

We have many small channels through the working material to provide good contact between the fluid and the working material (in this case metallic Gd). At any point in this idealized device the fluid and the working material are held at the same temperature by the good thermal contact. The device is taken as isothermal in planes perpendicular to this axis; and it is built so that heat conduction along the axis is small.

If there are M moles of working material per unit length the entropy change in the section between x and dx is given by:

$$\frac{\partial T}{\partial t} = - \dot{m}cR \frac{\partial T}{\partial x} \tag{A-3}$$

---

*Actual fluids may differ somewhat from this; a large temperature span is considered, but again simplicity demands this form approximation.

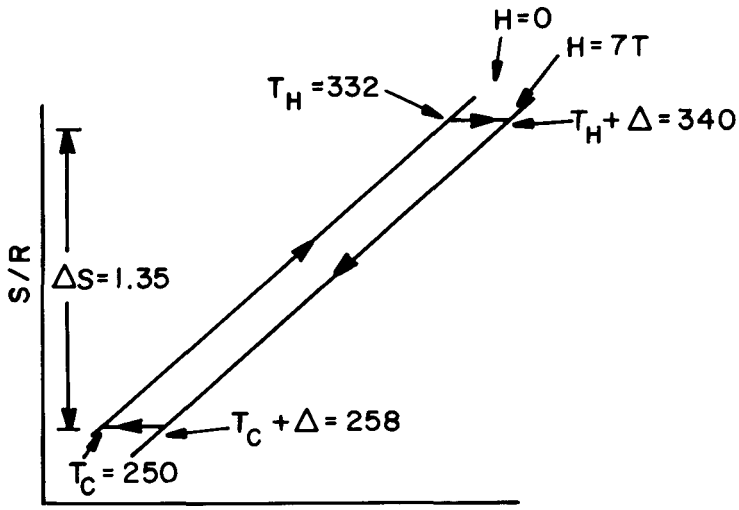

Figure A-1. Simplified S-T curves for Gd metal.

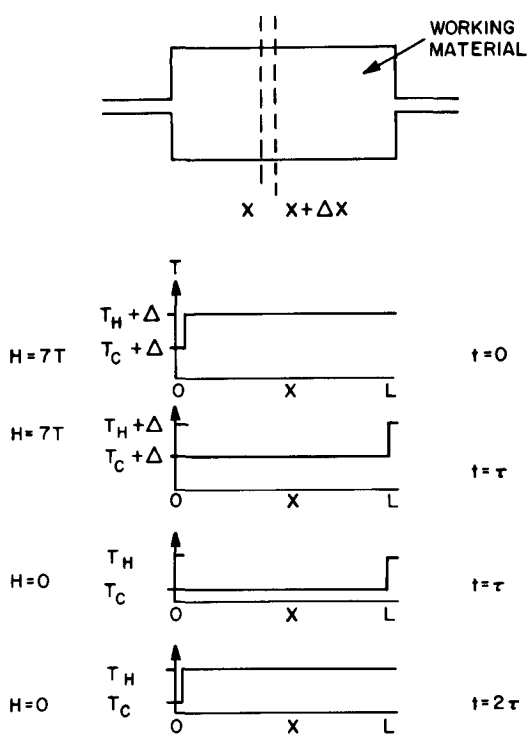

Figure A-2. Thermal wave propagation through an active magnetic regenerator type of refrigerator.

or, if H is held constant

$$\frac{\partial T}{\partial t} = -\frac{\dot{m}c}{Ma}\frac{\partial T}{\partial x} \tag{A-4}$$

$$T = f(x - \frac{\dot{m}c}{Ma}t) + \text{constant} \tag{A-5}$$

f ( ) is any function of $x-\dot{m}ct/Ma$, as determined by the boundary conditions. Equation A-5 is the equation for a wave moning through the device with velocity $v = \dot{m}c/Ma$.

We will now describe the performance of a refrigerator using these principles as shown in Figure A-2. At the start t=0, take the device to be in an applied field H=7T, and except for a small bit at x=0 at temperature $T_H+\Delta$. Fluid at temperature $T_C+\Delta$ flows into the cold end (x=0) of the refrigerator, and by Eq. (A-5) the cold wave move through the device arriving at the end at time $t = \tau$ given by

$$\tau = L/v = L/(\dot{m}c/Ma) = MaL/\dot{m}c \tag{A-6}$$

whereupon the fluid flow is stopped. The entire device (except for the hot end) is at $T_C+\Delta$, having been cooled in an applied field ($T_H+\Delta$ to $T_C+\Delta$ in Figure A-2b). Hot fluid, at $T_H+\Delta$ has flowed out of the refrigerator at x=L.

Now the field is removed, the device is adiabatically demagnetized from $T_C+\Delta$ to T_C. Now the fluid, having been cooled to T_H (delivering heat and entropy to the high temperature bath), returns down through the device. With a negative $\dot{m}$, Eq. A-4 describes a hot wave moving <u>down</u> through the refrigerator (fluid at T_C leaving device at x=0) for a period τ. Fluid flow is stopped, device is now at T_H (except for negligible section at x=0), and a field of H=7T is reapplied, returning us to the situation at t=0, and a cycle is complete. The fluid, being heated to $T_C+\Delta$ by the low temperature bath, is ready to be fed back through the refrigerator.

Let us see now, how much heat has been pumped and work done in this cycle. First, the entropy S_H in J/K per cycle expelled at the hot end is from Eqs. A-2 and A-6.

$$S_H/R = \dot{m}c(T_H+\Delta-T_H)\ \tau = \dot{m}c\Delta\tau \tag{A-7}$$

$$= \dot{m}c\Delta MaL/\dot{m}c = \Delta MaL$$

Similarly, the entropy entering cold end of refrigerator -

$$S_C/R = \dot{m}c(T_C+\Delta-T_C) = \Delta MaL \tag{A-8}$$

The fact that $S_H = S_C$ is required because we have not allowed for irreversibilities associated heat flowing downhill. The that Q_H, and Q_C deposited in the hot bath or removed from the cold bath is given by

$$Q_H = \dot{m}\tau \int_{T_H}^{T_H+\Delta} T\ dS = \dot{m}\tau R \int_{T_H}^{T_H+\Delta} c\ TdT \tag{A-9}$$

$$= \dot{m}c\,\frac{MaL}{\dot{m}c}\ \frac{(T_H+\Delta)^2 - T_H^{\ 2}}{2}\ R = MaL\ R\ \frac{(2T_H\Delta + \Delta^2)}{2} \quad . \tag{A-10}$$

similarly

$$Q_C = MaL\ R\ \frac{(2T_C\Delta + \Delta^2)}{2} \tag{A-10'}$$

By the first law of thermodynamics, the work (W) must be the difference in these energies given by

$$W = Q_H - Q_C = MaL\ \Delta\ (T_H - T_C)\ R \quad . \tag{A-11}$$

Also, from Figure A-1, the work done is the area of the parallelogram times the moles of working substance. Therefore, $W = \Delta SR\Delta \times ML$, remembering that $\Delta S/(T_H-T_C) = a$ (Eq. A-1 and Figure A-1), we have

$$W = a(T_H - T_C)\ \Delta\ MLR \tag{A-12}$$

consistent with Eq. A-11.